# IRON-ZINC INTERMETALLICS EFFECT
# ON THE FORMING BEHAVIOR OF
# GALVANNEALED IF-SHEET STEEL

by

Luis Gonzalo Garza-Martínez

J 6124
c. 2

J 6124
c. 2

A thesis submitted to the Faculty and Board of Trustees of Colorado School of Mines in partial fulfillment of the requirements for the degree of Doctor of Philosophy (Metallurgical and Materials Engineering).
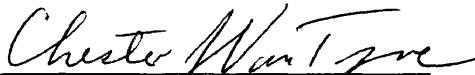
Golden, Colorado

Date April 16th, 2006

Signed: _____
Luis Gonzalo Garza-Martínez

Approved: _____
Dr. Chester J. Van Tyne
Thesis Advisor

Golden, Colorado

Date: 4/11/06

_____
Dr. John J. Moore
Trustees' Professor and Head of the
Metallurgical and Materials Engineering Department

iii

# ABSTRACT

Galvannealed (GA) interstitial free (IF) steel sheets are produced by annealing a hot-dipped galvanized IF-steel sheet. The GA coating is composed of four different Fe-Zn intermetallics. The $\delta$-phase and $\zeta$-phase are the main intermetallics present on the surface of the coatings, and their distribution affects the forming characteristics of the coated sheets, such as coefficient of friction (COF) and powdering. It is believed that the amount of $\zeta$-phase present on the surface of the GA coating controls the COF and the powdering in a forming process.

Nine GA coated IF-steels with a variety of $\delta/\zeta$ distributions on the surface were studied. Four of the those coatings shared the same experimental substrate coil, and were not temper rolled; the rest of the coatings had more common characteristics of a commercially available product. The COFs of the GA coated IF-steels lubricated with a common mill oil were measured with the flat die tribometer (FDT); and the bending under tension tribometer (BUTT), using a 50.8 mm and a 12.7 mm diameter roller die. The powdering of the GA coated IF-steels was measured with the double-Olsen powdering test. A scratch test was also used as alternative friction test. The limiting drawing ratio (LDR) of the GA coated IF-steels was measured with the Swift cup test, as a measure of the formability and as an indirect friction testing. The surfaces of the untested and tested samples were characterized and contact areas were calculated from 3D surface profiles.

It was found in every friction test that the COF increases as the Fe content of the coating decreases, and the COF also increases as the amount of $\zeta$-phase on the surface of the coating increases. The GA coated sheets that were temper rolled, had a preexisting contact area surface region, and had higher COF compared to the non temper rolled sheets. The real contact area of the tested samples increased as the applied normal stress increased for each individual coating, and this increase was larger for coatings with $\zeta$-phase on the surface. The COF increased with contact area of tested sample, and the behavior was found to be independent of both the friction testing performed and the phase distribution on the surface of

the coating. The powdering tests showed that the metal loss of the GA coatings is not directly influenced by the amount of $\zeta$-phase on the surface of the coating, but influenced by the amount of Fe content in the coating. However, in a forming process the $\zeta$-phase on the surface of the coating deforms increasing the real contact area, protecting the coating by decreasing the resulting normal and shear stress components. The LDR results presented lower values for the coatings with higher COF, however the range of values for all the coatings was small. The $\zeta$-phase on the surface of the GA coating is the most significant factor affecting the frictional response. The $\zeta$-phase deforms in contact increasing the real contact area, resulting in an increase of the COF.

The friction response of the GA coated steel sheets was found to match a mixed film lubrication (MFL) regime. The behavior of the COF versus the real contact area matched the model. The model applied to the experimental data allowed the determination of the boundary lubrication COF, $\mu_b = 0.397$.

# TABLE OF CONTENTS

# LIST OF FIGURES

# LIST OF TABLES

# ACKNOWLEDGEMENTS

To my beloved parents Jesus and M. Olivia,
and my love Kelcey.

# CHAPTER 1

# INTRODUCTION

Galvannealed (GA)-coated sheet steels are widely used in exposed and non-exposed automobile panels as well as in appliances, primarily for their corrosion resistance. GA-coated sheet steels are fabricated by annealing a hot-dipped galvanized sheet steel. The annealing process promotes diffusion of iron and zinc, creating a series of Fe-Zn intermetallics. GA coatings offer several advantages when compared to the galvanized coating such as improved weldability and paintability and, in some reported cases, improved corrosion resistance. GA-coated sheet steels exhibit different forming behavior such as friction and powdering as compared to galvanized or non-coated steels. These behaviors are dependent on the distribution of the intermetallics in the coating, which is itself a product of the different annealing conditions.

This chapter presents a basic introduction to and a brief history of the zinc coating processes. It also covers the different intermetallics and characteristics of the Fe-Zn system. Finally, it introduces the two major forming issues of concern in this dissertation, powdering and friction.

## 1.1 Zinc Coating Technology on Steels

Steel sheets are coated with zinc to prevent corrosion. Zinc provides galvanic protection and also serves as a barrier. Nonprotective zinc hydroxide forms protective zinc carbonate by reaction with $CO_2$ and moisture in air; steel exposed at scratches or cut edges is galvanically protected if sufficient zinc is present [1]. Iron and zinc form a galvanic couple where iron, the more noble metal, is protected by the more active metal, zinc, which becomes a sacrificial anode.

In 1836, Sorel, a French scientist, patented the process of zinc plating by dipping iron into molten zinc (now known as galvanizing). Sorel was well aware of the sacrificial role of

1

the zinc coating in the iron, the knowledge of this role is the reason for the term 'galvanizing' [2]. A few years earlier in 1828, R. Walter of Rotherham introduced the idea of stiffening sheet iron by corrugating, so by 1836 the technology was established for what is now know as 'corrugated iron', a galvanized corrugated iron sheet [2].

Bracelets made of zinc found in the ruins of Cameros (prior 500 B.C.) give us some reason to believe that zinc was know by the Ancients. Zinc metal was well known in the Far East prior to such knowledge in Europe, and great quantities of zinc were imported to Europe from China and India as early as the 16th century [3]. The German scientist, Andreas Marggraf, was the first to successfully separate pure zinc metal from a mineral called calamine in 1746, marking the rediscovery of the metal. It was William Champion of Bristol, England, who was credited for developing the first intentional production of metallic zinc in the West in 1743. In Champion's visits to China prior to 1740, he learned and developed his method [2,4].

There are two primary methods of applying the zinc coating to a steel sheet. In the first method, hot-dip-galvanizing (HDG), the steel sheet goes through a molten bath of a zinc alloy, and the resulting material is called galvanized (GI). In the second method, electro-galvanizing (EG), the steel strip enters a zinc ion aqueous solution bath, the coating is deposited by electrodeposition, and the resulting steel sheet is called electro-galvanized (EGI). After the application of the Zn coating, the coated steel sheet can be heat treated. The annealing allows diffusion to occur between the iron and zinc, promoting the formation of Fe-Zn intermetallic compounds. The annealing process changes the phases and phase distribution within the coating. The resultant material is known as galvannealed (GA) sheet steel. HDG is the common coating application for GA sheets, although EGI sheet can be annealed as well, producing an electro-galvannealed sheet (EGA). Nevertheless, electro-deposition allows for the application of the desired Fe-Zn intermetallic, and the annealing process can be avoided [5].

Zinc and zinc alloy electrodeposition of steel strip takes place in either sulfate- or chloride-based electrolytes, up to speeds of 213 m/min. The zinc, alloying nickel, or iron metal ions are contained in an electrolyte solution acidified with sulfuric or hydrochloric

2

acid. Sometimes alkali or ammonium salts are used to increase the conductivity of the solution. The sulfate process is the type most widely used in zinc and zinc alloy steel plating because of its simple chemistry and because the solution is compatible with the insoluble anodes. Another advantage of the sulfate electrolyte is that it can deposit finer grain coatings without requiring organic additives and it can operate over a wide range of current densities, temperature, and acidity. Zinc plating plants are very complex; the steel strip passes first through a series of cleaning stages prior to entering the plating cells. The plating cells can be radial, vertical, or horizontal. After plating, the strip is cleaned, temper rolled, and additional coatings (organic coatings or paint) are applied before coiling [6]. Figure 1.1 shows an example of an EGA coating line.
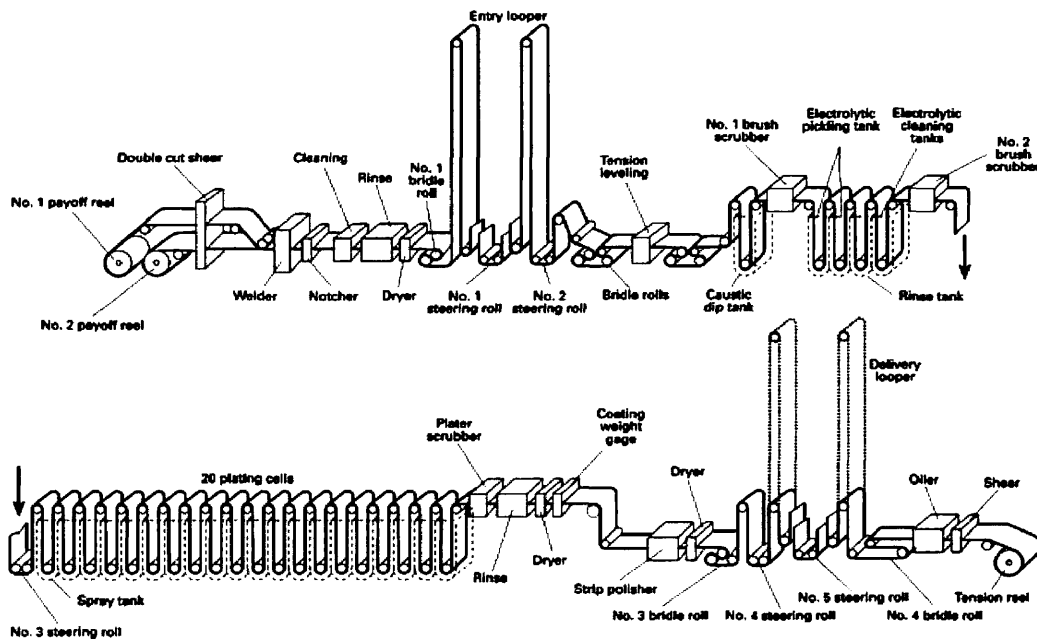


**Figure 1.1**     Schematic diagram of a typical electrogalvanizing line with vertical plating cells (L.W. Austin and J.L. Lindsay, "Continuous Steel Strip Electroplating," slide course, American Electroplaters and Surface Finishers Society, 1989) [6].

In the hot dip sheet-coating process, the steel strip is cleaned of debris and residual oils in cleansing baths and by mechanical methods. The steel strip is then heated in a mixed nitrogen and hydrogen atmosphere that removes iron oxides from the surface, above the

3

recrystallization temperatures about 700 °C, as part of the heat treatment of the strip, or at lower temperatures if a heat treatment is not needed. If heat treated, the strip is cooled to about the melt pot temperature prior to entering. The steel strips enter the pot containing the molten zinc where the actual coating takes place. The strip exits the pot with a thin layer of liquid zinc adhering to the surface. Gas blades control the thickness of the final coating and provide a rapid quench. There are a variety of post-coating processes that can be applied before coiling to improve mechanical properties, surface quality, and corrosion resistance, for example: annealing, skin passing, oiling, phosphating, and flash electroplating [6,7]. The annealing process that produces a GA steel sheet is of interest in the present study and will be more fully described. Figure 1.2 presents a schematic of a hot-dipped galvanizing line.
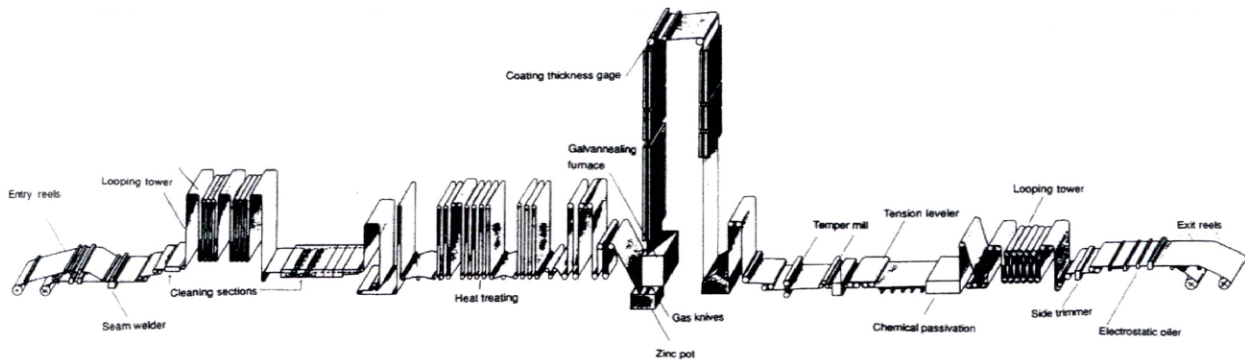


**Figure 1.2**    **Schematic diagram of a continuous galvanizing line. An example of a "hot" line with in-line annealing capability [6].**

Besides pure zinc coatings for steel sheets, there are other different zinc alloys. Fe-Zn coatings are produced by annealing the hot-dipped coated sheet producing GA-coated steel sheets. The annealing step, promotes diffusion of iron and growth of the respective intermetallics. Another kind of zinc coating alloy is Al-Zn coatings. Hot-dipped Zn containing 5 wt% Al and about 0.1 wt% of mischmetal rare earths such as cerium and lanthanum (Zn-5Al-0.1mischmetal), commonly known as Galvafan®, produces a eutectic microstructure that has better formability characteristics as compared to GA steel sheets, and it provides excellent corrosions resistance and paintability as well [6,8,9,10,11,12]. Galvalume® is another Zn alloy coating containing 55 wt% of Al and about 1.5 wt% of Si

4

(Zn-55Al-1.5Si). The high amount of Al offers an excellent long term atmospheric corrosions resistance, while the reduced Zn still offers a good galvanic protection for scratches and cut edges. Galvalume® steel sheets are primarily used in pre-engineered metal buildings, especially for roofing material [6,11,12,13,14].

Zinc-coated steel sheets have a wide range of uses. In Japan, the automotive industry consumes 39 % of the domestic production of zinc-coated steel, followed by construction 19 %, packing 14 %, appliances 9 %, with the remaining 19 % having diverse uses [15]. Nowadays more than half the weight of the steel used in an automobile is coated steel, and although EG, GI, as well as GA coatings are used, GA is becoming one of the favorites because of the advantages it offers to post-processing [16]. The appliance industry has used larger amounts of zinc-coated steel sheets in the last several years. This industry has tried other types of coatings or pre-painted steel sheets, but the corrosion resistance and cost of zinc-coated steel sheets makes it an optimum choice.

Galvannealed steel sheet offers certain advantages to mass productions requirements of the auto-making industry. Panels are joined using spot welding, a welding process that pulses an electric current from the electrodes while they are clamping the sheets in place, fusing the sheets by resistance heating. Figure 1.3 shows a diagram that exemplifies the spot welding process. The copper alloy electrodes operate at a temperature above the melting point of the zinc. Pick up of zinc to the electrodes and diffusion of the zinc into the electrodes changes the electrode operational characteristics, increasing the current needed for the spot welds and reducing its operational life. The Fe-Zn intermetallics of the GA coating, having a higher melting point of that of pure Zn, are not picked up by the electrodes as much as zinc from a galvanized coating, improving to acceptable levels the life of the electrodes [17]. Another advantage of the GA coating is the improved paintability. Pure zinc coatings as in galvanized sheet, with a very smooth finishing surface, are often treated with phosphorous, roughening the surface to improve the adhesion of paint. The rough surface finish of the GA coating provides good paint adhesion properties and does not require any further treatment [18].

5
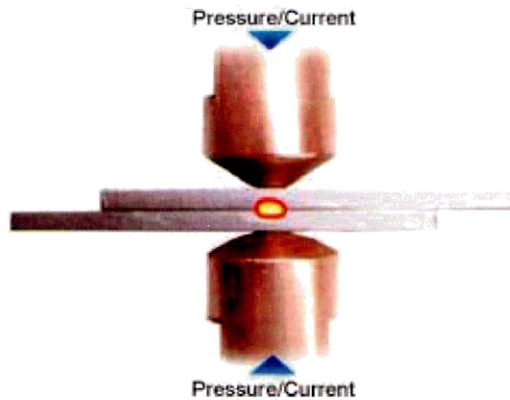
**Figure 1.3** **Diagram of a spot weld. (www.fpe.co.uk/graphics/resist_diag.jpg)**

While possessing several manufacturing benefits, GA sheets also present several forming challenges. Depending on the intermetallic phases present in the coating, the friction coefficient can vary, and coating defects such as flaking and powdering are reported to occur for GA sheet steels. Automotive customers are demanding coated sheets with specific GA microstructures in order to enhance forming characteristics. The scope of this document is to describe and understand the behavior of the coating in a forming operation.

## 1.2 IF Steels

Interstitial free-(IF) steels are produced by a careful process of carbon reduction and stabilization with either niobium or/and titanium. Low carbon steels (< 50 ppm) developed in the 1970s were used for their exceptional drawing characteristics, the anisotropy and elongation of the clean ferrite matrix making it possible to withstand heavy deformations, as in a deep drawing forming process. Reheating of the molten steel in a vacuum chamber with argon stirring reduces the carbon content in the melt, and aluminum addition maintains the low oxygen level. At the end of the vacuum degassing process, additions of Nb[1 see foot note] or

---

[1] In order to maintain certain agreement with international conventions, niobium (Nb) will be used instead of columbium (Cb) for element 41 of the periodic table. In 1801 Charles Hatchett, a skilled chemical analyst, described a new mineral called columbite, named after the location it was found in North America. Hatchett showed that the mineral contained a new element and he called it columbium and the mineral columbite, after its place of origin. In 1802 Ekeberg discovered a new metal in a rare earth mineral

Nb-Ti react with carbon and nitrogen, leaving a ferrite matrix fee of interstitials (< 30 ppm of carbon), hence the name IF-steels. Products of the stabilization, NbC, TiC, and TiN, precipitate at the grain boundaries controlling grain growth and resulting in improved mechanical properties [19,20].

IF-steels were not developed specifically for galvanized sheets but resulted in the best option for both, the drawing characteristics needed for the applications and for the adhesion of the coating to the substrate. Although applications for galvanized IF-steels are diverse, they are of particular importance for the automotive industry. Exceptional drawing characteristics combined with corrosion resistance make galvanized IF-steels the best option for exposed and unexposed automobile panels. Around 75 % of the body, chassis, and power train of a typical American automobile manufactured in 1986 were composed of zinc-coated steel [21]

## 1.3 Galvannealed Coatings

The GA coatings are a product of an annealing process that forms intermetallics in the coating. The section describes the annealing process and the intermetallic evolution of the coating.

---

called yttrotantalite, and called it tantalum because like Tantalus in the Greek myths who could not drink, this new element would not react with acids. Both columbite and tantalite were analysed by William Wollaston in 1809 (after Hatchett had effectively given up science and taken over his father's coach-building business following the latter's death). Wollaston was confused by the similarity in the physical and chemical properties of the two elements and he thought they were the same i.e. he stated that Hatchett's columbium and Ekeberg's tantalum were in fact the same element and consequently the two elements were confused until 1844.

In 1844, not long before Hatchett died, Heinrich Rose 'rediscovered' columbium, but he now called it niobium after the Greek nymph Niobe, who was the daughter of Tantalus - thus recognizing the close relationship between the elements tantalum and niobium (columbium). Hatchett had already shown that the oxide of niobium, $Nb_2O_5$, and the corresponding oxide of tantalum, $Ta_2O_5$, had different properties. Wollaston's reputation had ensured that his erroneous views prevailed over Hatchett's, especially as Hatchett had given up science by then [Peter E. Childs, University of Limerick, Ireland, http://www.ul.ie/~childsp/CinA/Issue65/TOC43_Columbian.htm]

For these reasons it is the author's opinion that the name columbium should be used instead, in recognition of the first scientist that discovered the element. The name columbium is sometimes still in used in North America.

## 1.3.1 Coating processes

GA-coated steel sheet is a hot-dipped steel sheet that was heat-treated immediately following the zinc coating. The heat treatment allows for diffusion to occur between the iron and zinc, forming the different Fe-Zn intermetallics. The Zn-Fe alloy coating has different characteristics, higher melting point, and a rougher surface, improving the weldability and paintability of the coating. Figure 1.4 shows a light optical micrograph and a scanning electron microscope – secondary electron image (SEM-SE) of a GA coating where the different Fe-Zn intermetallics are indicated.

The Fe-Zn system has been extensively studied. The first Fe-Zn phase diagram is often attributed to J. Shramm in 1938 [5], but since that time there have been many modifications especially in the Zn-rich zone [22]. The latest version of the binary phase diagram, and the one that will be used in this dissertation, is the one proposed by Burton and Perrot in 1992 [23]. Figure 1.5 and Table 1.1 present the phase diagram and the comprehensive list of phases. This binary phase diagram does not show all of the possible intermetallic phases as described in other proposed phase diagrams [22]; however, it is a practical phase diagram presenting only the phases that can be identified at room temperature. Further description of the different phases will be given below.
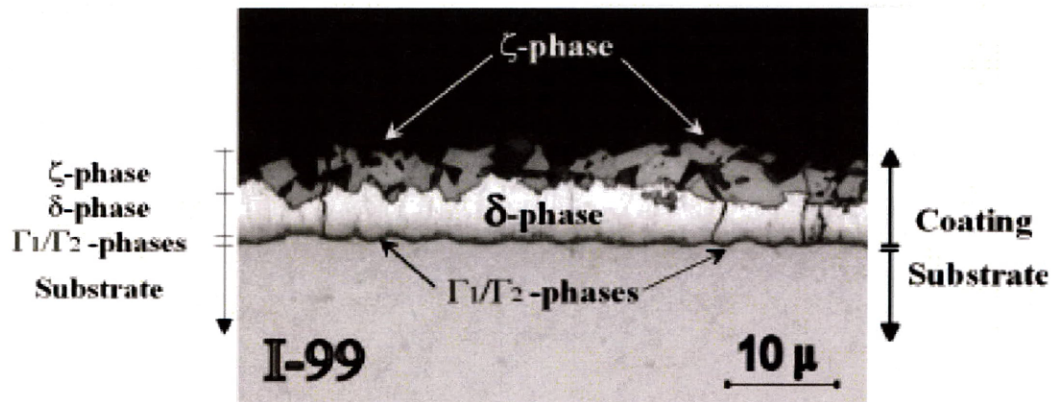
(a)
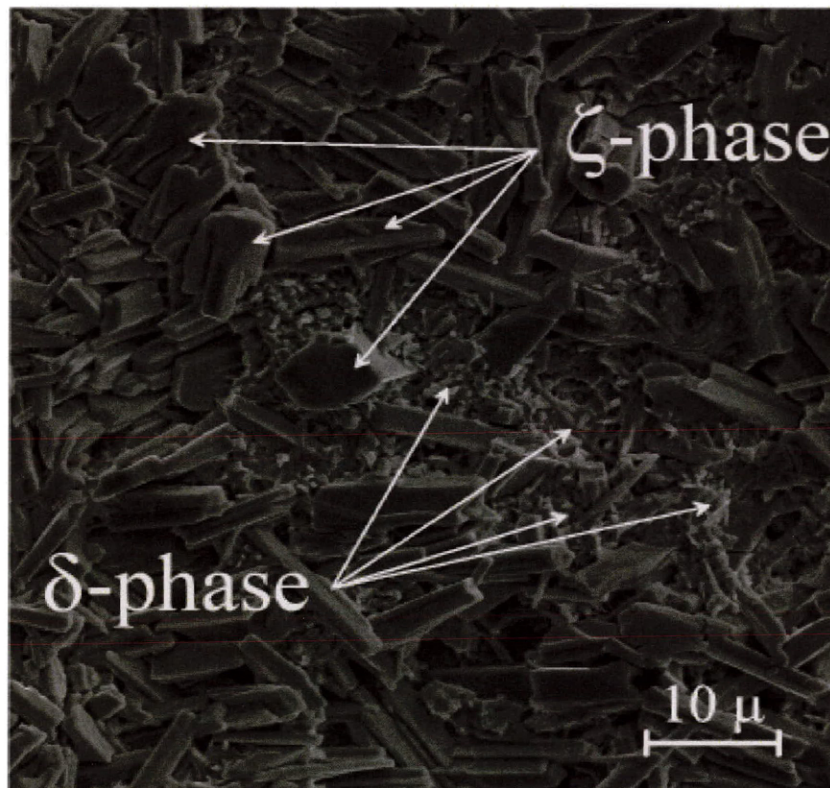


(b)

Figure 1.4    Examples of GA microstructure.  (a) light optical micrograph of a GA coating with the Fe-Zn intermetallic phases indicated; (b) SEM-SE image of the surface of a GA coating with the Fe-Zn intermetallic phases indicated.
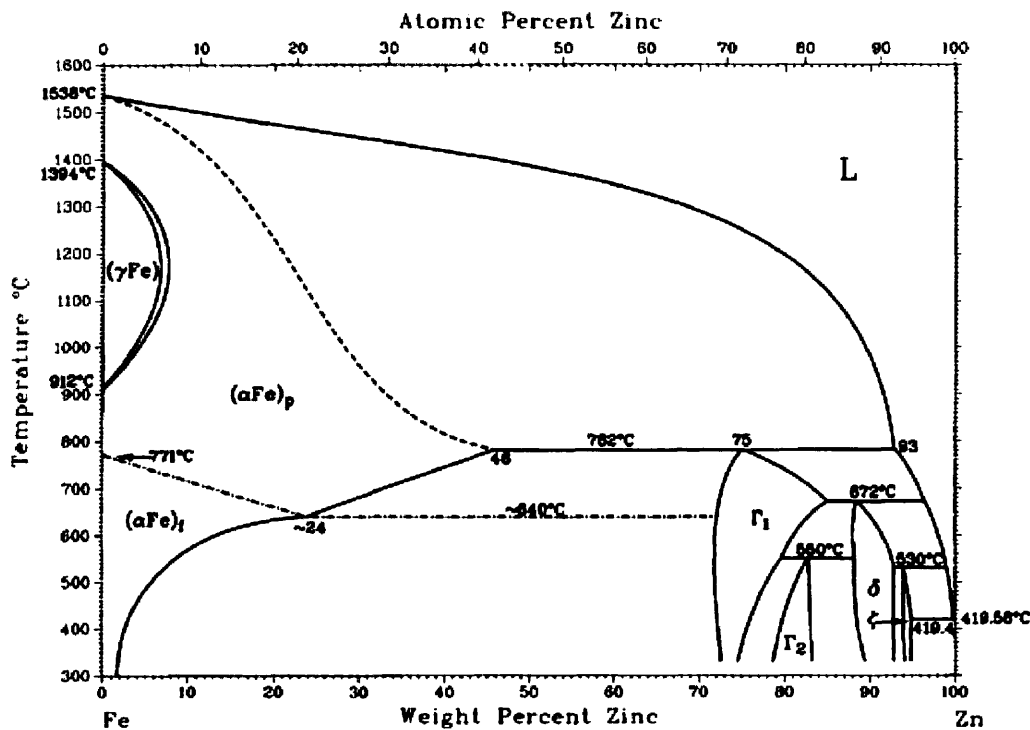
**Figure 1.5**      **Fe-Zn binary phase diagram [23].**

**Table 1.1**      **List of Fe-Zn phases[23].**

| Phase | Composition, wt% Zn | Pearson symbol | Space group |
|---|---|---|---|
| (γ-Fe) | 0 to 6.59 | cF4 | $Fm\bar{3}m$ |
| (α-)Fe, (δ-Fe) | 0 to 46 | cI2 | $Im\bar{3}m$ |
| Γ1 | ~72 to ~85 | cI52 | $I\bar{4}3m$ |
| Γ2 | 0.91 to 83 | cF408 | $F\bar{4}3m$ |
| δ | 88.5 to 93.0 | hP555 | $P6_3mc$ |
| ζ | 94 to 94.8 | mC28 | $C2/m$ |
| (Zn) | ~100 | hP2 | $P6_3.mmc$ |

The ζ-phase is the richest Zn intermetallic, $FeZn_{13}$; its crystal structure is monoclinic. The δ-phase is the second Zn-rich phase, $FeZn_{10}$; it has a complex hexagonal crystal structure. The Γ2-phase, $Fe_5Zn_{21}$, has a complex face-centered cubic structure. And finally, the Γ1-phase, $Fe_3Zn_{10}$, has a body-centered cubic structure. The Pearson symbols and space

groups of the phases are listed in Table 1.1. In a more recent study, Tang *et al.* had identified an extra intermetallic phase that is not presented in the binary phase diagram, the T-phase (*cF408*) which forms with longer annealing times [24].

In other proposed phase diagrams, $\delta$-phase is usually identified as $\delta_1$-phase; the $\delta$-phase is stable at temperatures between 620 to 672 °C and with a more limited solubility compared to $\delta_1$-phase. It has been postulated that the $\delta_1$-phase consists of two distinct phases, the compact $\delta_{1k}$, and the palisade $\delta_{1p}$-phase, both separated by a two phase region; the distinction between these two phases is more morphological, since they have the same crystallographic structure [22]. Although these two $\delta$-phases are well distinguished either in SEM-SE images or light optical micrographs with color capabilities, they always share the same characteristic morphology and will be treated as one phase, called
$\delta$-phase in this document.

## 1.3.2 Galvanizing and intermetallic phase evolution in galvannealing

In the galvanizing process, small quantities of aluminum are added to the zinc bath (between 0.10 to 0.20 wt %). Because of the high affinity of Al for Fe, these small Al additions create an inhibition layer between the substrate and the molten Zn that prevents rapid intermetallic formation and growth of the $\Gamma$-phase, as well as outburst formation. In a continuous GA process, after the sheet has been submerged in the molten Zn bath, air nozzles quench the coating and act as knives controlling the thickness of the coating. The sheet then goes through the annealing process, and the coating that in this stage consist of $\eta$-phase melts and the formation of the different intermetallics begin.

At the beginning of the annealing process, the inhibition layer starts to break down as Al diffuses into the Fe substrate. The $\Gamma$-phase forms immediately at the interface with the substrate. There are discrepancies in the literature about the formation mechanisms of the intermetallics. Some authors describe it as a solid diffusion mechanism, while others discard the solid diffusion transformation and propose a dissolution of phases into supersaturated liquid which precipitate into another phase. In either case, the first intermetallics to form are $\Gamma$-phases at the interface with the substrate and $\delta$-phase that nucleates from the liquid zinc.

In the solid state diffusion description, the coating solidifies into a mixture of predominantly η, ζ-phase, with some minimal δ-phase. The ζ-phase grows rapidly consuming the η-phase until it reaches the surface; meanwhile, the δ-phase grows in a columnar manner consuming the ζ-phase [25]. In this description it is not clear if the diffusion of Fe or the diffusion of Zn is controlling transformation species. It has been reported that the diffusivity of Zn in Fe is more rapid than the diffusivity of Fe in Zn, which would cause the Fe rich intermetallics to form first, supporting the evidence that the Γ-phases are the first intermetallics to form [22]. In the other formation description, the zinc solidifies into a mixture of Γ-phases at the interface with the substrate and ζ-phase surrounded by liquid Zn; the ζ-phase dissolves back into the liquid; the δ-phase precipitates from the Fe-rich liquid. This mechanism explains why there is no correlation with the δ-phase and the previous blocky ζ-phase, as well as explaining the rapid growth of the δ-phase from the liquid, rather than from solid-state diffusion [26,27]. It is the author's opinion that both descriptions are correct, and the annealing temperature controls which mechanism operates.

Substrate alloying elements are reported to have an effect on the kinetics of the coating annealing. C and P retard the incubation time of the intermetallics, while Ti and Nb accelerate the incubation time of the intermetallics. When Si is present in the substrate, Si-oxides alter the wetting of the Zn, creating uneven coating solidification [28].

By controlling temperature and time in the annealing process, different combinations of intermetallic phases can be produced. Coatings can be produced with 100 % of ζ-phase at the surface, 100 % of δ-phase, or a mixture of both. The thickness of the Γ-phase can also be controlled by the amount of Al in the Zn bath as well as by the annealing conditions. Different intermetallic distributions have different manufacturing responses. The presence of the ζ-phase at the surface of the coating increases the coefficient of friction (COF), introducing complications into forming operations. Meanwhile, a coating with only δ-phase at the surface tends to present more powdering defects (powdering is the defect of coating breakage and de-attachment from the substrate). When the Γ-phase is significant, because of its brittle nature, powdering is increased considerably. These defects and their implications

12

will be more extensively described in this chapter. The effect of the phase distribution on these behaviors is the main concern of this dissertation.

## 1.4 Formability and Friction

Flat products like GA sheets are often formed into shapes such as a panels or structural members. Fuel efficiency requirements demand parts with reduced thickness. Forming processes have also become more demanding. The GA coatings have introduced one more difficulty into the stamping process by increasing the COF as compared to uncoated steel sheets and to GI-coated steel sheets. Forming capabilities such as the limiting drawing ratio and such are controlled not only by the substrate but are also dependent on the frictional response of the sheet. Powdering defects play an important role as well, affecting the life span of the forming dies.

## 1.4.1 Forming defects: powdering and flaking.

Powdering defects can be defined as: particle formation by intracoating failure to produce particles with dimensions less than the coating thickness [29]. Another related defect, flaking, is defined as: the formation of flat particles by decohesion of the coating/substrate interface to produce particles with sizes similar to the coating thickness [29]. In this document the term "powdering" will be used indistinctively of the size of the particle, meaning it could be a powdering or flaking defect according to the given definitions.

Powdering defects have two implications. The loss of the coating reduces the galvanic protection of the steel sheet; more importantly, when powdering occurs continuously in a forming process, it often induces another defect call galling. Galling occurs when particles from the formed sheet bond to the tool surface. The adhered particles plough through the coating or bond to the coating resulting in additional coating damage [29]. The de-attached coating or powder adheres to the tool die, affecting the smoothness of the die surface, locally increasing the COF and producing galling defects

One of the most popular powdering tests in industry is the double-Olsen powdering test. In the double-Olsen test, a sheet sample is clamped to a table with a circular die, and the

13

sample is deformed with a spherical punch; the sample is turned around and deformed in the opposite direction. This reverse deformation produces bending in the sheet in two directions, causing some of the coating to flake off. The samples are weighed before the test, after testing a special tape is used to pull loose coating off the sheet. The samples are cleaned and weighed again. The difference in weight is the coating loss. There is a visual interpretation of the damage of the coating, but that technique is more subjective, developed for rapid testing in production environments. Figure 1.6 shows a diagram that graphically explains the double-Olsen test.
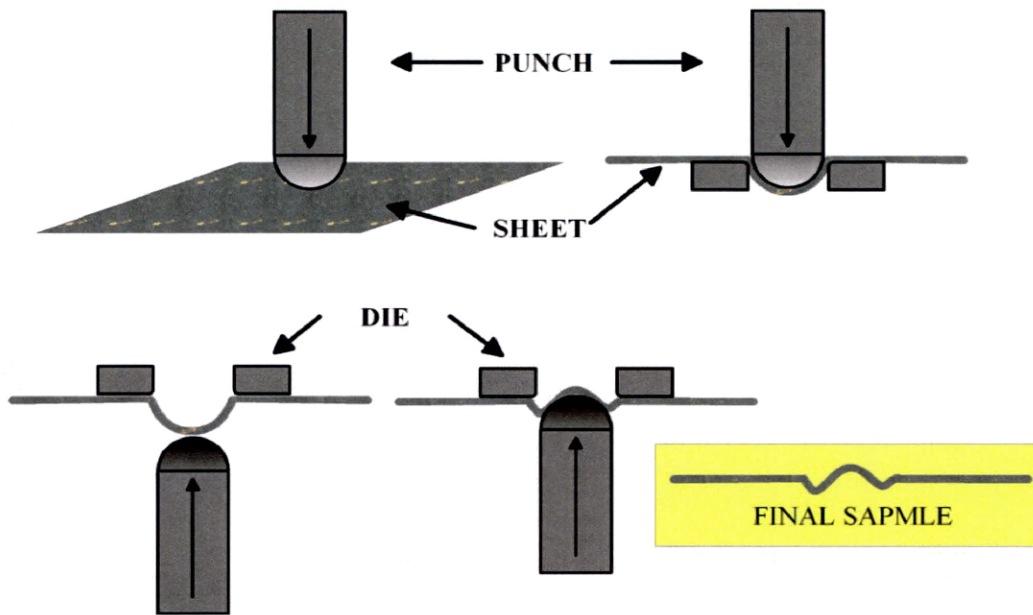


**Figure 1.6**       **Diagram of the double-Olsen powdering test.**

Powdering has been widely investigated. Rangarajan *et al.* described the failure mechanism of the coating using different forming tests as the draw-bead simulator and the cup drawing test [30,31]. They found that powdering occurs when the coating is subjected to compressive stresses. Tensile stresses produce cracking of the coating but do not produce powdering. No evidence was found of friction induced powdering. The brittle δ-phase, being the hardest and constituting most of the coating, is strongly related to powdering behavior [32]. Zhong *et al.* using the double-Olsen test, found that the severity of the

powdering increases with $\delta$-phase grain size. They also found that as the Fe content in the $\delta$-phase increases the powdering also increases [33].

Powdering has also been attributed to the thickness of the $\Gamma$-phase. Cheng *et al.* measured the effects of substrate microstructure of GA-coated extra-low carbon steels by means of a conventional 60° bend test; their conclusions were that if the $\Gamma$-phase is present in the coating, the propensity for powdering increases with the thickness of the $\Gamma$-phase layer [34]. Other authors like Shi *et al.* maintain that the cracking of the coating propagates through the $\Gamma/\delta$ interface. They claim that this interface is the most brittle component of the coating [35].

Crater formation is another coating defect. Shrinkage during solidification and uneven phase growth are the common causes of this defect. Craters are reported to contribute to reducing the occurrence of powdering. Most of the studies attribute this phenomenon to the ability of the craters to accommodate strain when the coating is subject to compressive stresses [36,37]. One thing all studies agree on is that the presence of $\zeta$-phase decreases powdering behavior [30,31,32,33,34,35,36,37,38]. In many articles it is stated that the $\zeta$-phase helps in decreasing the powdering defects, either by alleviating the strain, or as a sign of lower Fe content in the coating. It is not entirely clear as to the fundamental role that the $\zeta$-phase plays in keeping the galvanneal coating defect free.

## 1.4.2 Friction and tribology

Friction is the force in opposition to the sliding movement of two objects in contact with each other. Friction is an everyday occurrence, and without friction forces life could not be possible. As an example, when walking, a person uses friction forces to impel himself forward; as he transfers weight from one leg to the other, he kicks his feet backward causing him to move forward. When the friction coefficient gets modified, as when a person walks on ice, the forward movement is not as simple. In other instances, the friction forces are intentionally reduced. In an engine, the use of lubricants increases efficiency by reducing the friction of moving parts, such as gears. In a Formula 1 racing car, the aerodynamic design of

the car's body produces downward forces, increasing the frictional forces to a maximum, helping to maintain control of the car at such high speeds of up to 360 km/h.

Friction force is defined in the ASTM Standard G-40-93 in "Standard Terminology Relating to Erosion and Wear" as: "the resisting force tangential to the interface between two bodies when, under the actions of an external force, one body moves or tends to move relative to the other", and COF is defined as: "the ratio of the force resisting tangential motion between two bodies to the normal force pressing those bodies together".

The symbol $\mu$ is used to express COF.

[ Eq. ] 1-1
$$\mu = \frac{F}{N}$$

where $F$ is the frictional force and $N$ is the normal force.

This proportionality of forces for the COF was first described by Guilaume Amontons, a French physicist in 1699, although it was Leonardo Da Vinci who was the first to investigate frictional behavior of materials, Figure 1.7 shows some of da Vinci's sketches for friction studies. The other important statement by Amontons is that the force of friction is independent of the apparent area of contact.

The COF can also be expressed as:

[ Eq. ] 1-2
$$\mu = \frac{\tau_i}{\sigma}$$

where $\tau_i$ is the interface shear stress, and $\sigma$ is the normal stress acting on both bodies.

The ratio in [ Eq. ] 1-2 is known as part of the Coulomb's law of friction. Charles Augustin de Coulomb (1736-1806) was a French military engineer and a physicist, also famous for his work in electromagnetism. His work in friction is better recognized for describing the independence of the COF and the sliding velocities as well as the difference between static and dynamic friction.

If normal stress and/or COF are sufficiently high, up to a point it is more energetically favorable for the weakest material in contact to deform by shear. Another expression for the interfacial shear stress has been developed:

16

**[ Eq. ] 1-3** $\qquad \tau_i = mk$

where $k$ is the shear strength of the material and $m$ is the frictional shear factor. The values of m can be from, $m=0$ for a frictionless interface, up to $m=1$ where there is a sticking friction behavior.

Tribology is the science that studies friction, lubrication, and wear. The word derives from the Greek τριβσ (tribos) which also means rubbing. The term tribology is relatively new, it was establish after being suggested by H. P. Jost of a group of British lubrication engineers in 1966.

All these friction relationships presented above were developed from macroscopic observations. One result of the Coulomb's friction law is that the COF is independent of the contact area. In reality, tribology systems are more complex. When taking a closer look at tribological systems, surfaces are imperfect having topographic irregularities. In the case of two sliding hard metals, the surfaces in contact can be smooth or can contain certain degree of roughness in the form of asperities. The contact of two metals is the interaction of the asperities which, depending on their size and distribution, present different real contact areas, plastic deformations, and in some cases adhesion between the metals.
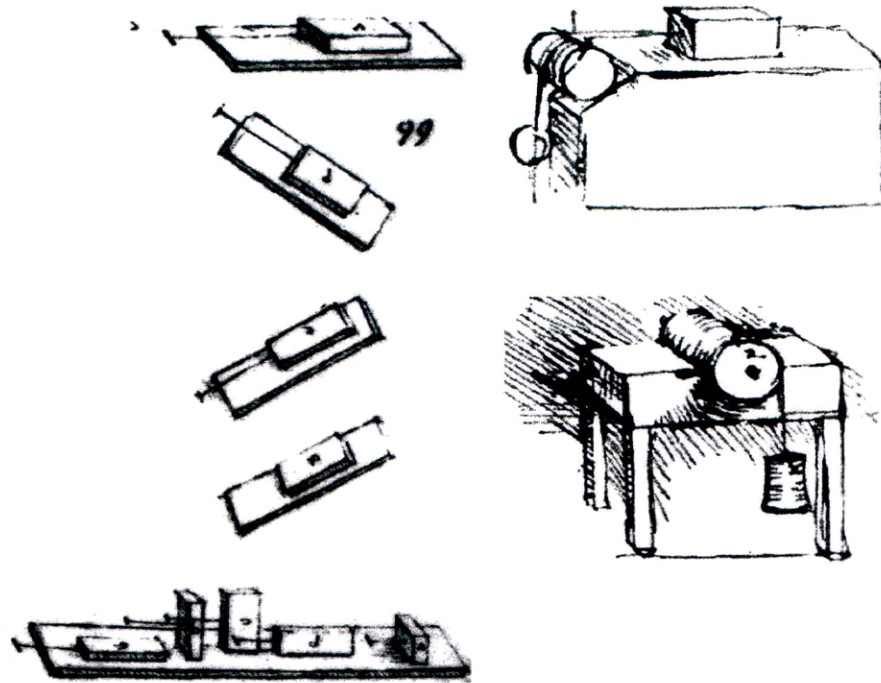
**Figure 1.7**   **Leonardo da Vinci's studies of friction. Sketches from the *Codex Atlanticus* and the *Codex Arundel* showing experiments to determine: (a) the force of friction between horizontal and inclined planes; (b) the influence of apparent contact area upon the force of friction; (c) the force of friction on a horizontal plane by means of a pulley; (d) the friction torque on a roller and half bearing. (Figure taken from History of Tribology by D. Dowson, London, 1979) [39].**

The friction between two metals, besides producing some localized plastic deformation, also cause the temperature of the surfaces to rise. This temperature rise modifies the mechanical properties of the metals in contact.

It has been of great interest to measure the COF. In the Webster's Revised Unabridged Dictionary (1998) "tribometer" is defined as *an instrument to ascertain the degree of friction in rubbing surfaces*, the word "tribometre" was used in the 18th century by Goldsmiths to mean "measure of friction". The most common tribometer apparatus is one in which a block of a material is placed on a flat surface and the force to initiate movement is measured; the ratio of the weight of the block and the force needed to initiate movement give

a measure of the COF between the block material and the surface. A variation of this apparatus is one in which the sliding surface and one extremity can be lifted forming an angle with the vertical; a block of material is place on the rotating surface and the angle at which the movement initiates is measure. It can be easily proven that the angle of the rotating surface at which the movement initiated gives a direct measure of the COF, and it is expressed as:

[ Eq. ] 1-4    $\mu = \tan \theta$

where $\theta$ is the angle of inclination at which sliding commences. Figure 1.8 shows diagrams of these two basic tribometers.
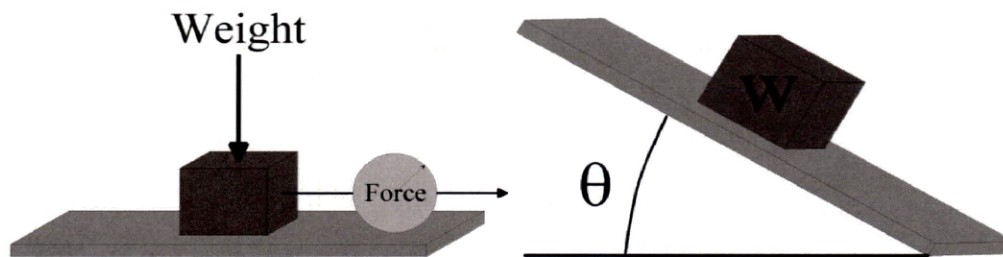


**Figure 1.8        Diagrams of common tribometers.**

In metal forming where the normal stresses are such that would cause deformation, the friction testing involves higher normal loads compared to the simple tests described above. One of the most common sheet forming friction tests is the flat-die tribometer (FDT). In the FDT, a sheet is pulled while a set of flat dies are clamped to the sheet. The ratio of the clamping force and the pulling force gives a measure of the COF. The FDT can be modified so that the sheet rests on a frictionless moving table and the normal load is applied to only one side of the sheet. This test is known as the sliding test. Another test commonly used by the industry is the bending under tension tribometer (BUTT). In this test the sheet is bent over a circumferential radius at a defined angle and pulled while the sheet is being held by a back force. From the measured pulling force and the back force the COF can be calculated. This test is sometimes preferred to measure COF of sheets because it produces stress states closer to the ones a sheet would be experiencing in a forming process. Figure 1.9 presents

diagrams of both the FDT and the BUTT friction test set ups. These two friction testing procedures will be described in more detail in Chapter 3.



(a)



(b)
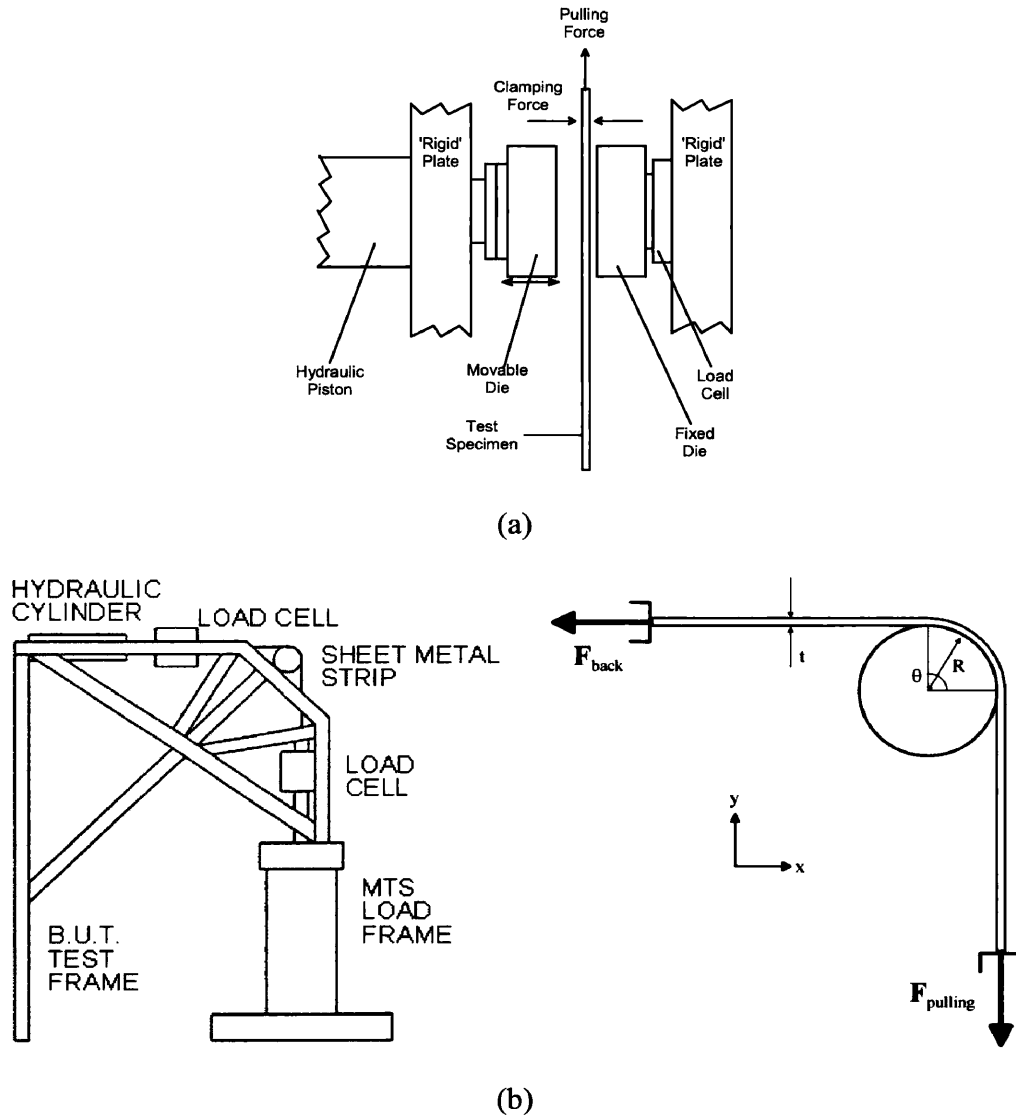
**Figure 1.9**     **Diagram of the flat die tribometer (a); and bending under tension tribometer (b).**

# CHAPTER 2
# PHILOSOPHY

Galvannealed coatings were developed to solve limited electrode life problem for spot welding of zinc-coated sheet steels. Galvannealing produces a coating with better paintability without the need for a phosphorizing process. These new coated steel sheets with improved manufacturing capabilities posed new forming challenges. The new brittle coating is prone to powdering, and coefficient of friction is increased. Significant amount of research has been done to try to characterize the effects of the processing parameters and the resulting intermetallic phase distributions to the powdering and frictional response of the galvannealed coatings. Significantly more research has been done in order to understand the kinetics of the formation of the intermetallics, the influences of elements on the formation and growth of the intermetallics, substrate influence on intermetallic formation, etc. With the available knowledge, the steel sheet users can make decisions on the type of coating that is best for their own specific forming requirements. In addition, coating line operators can define a processing schedule that will deliver a coating that complies with the demands of the user.

Although the amount of research dedicated to galvannealed sheet steels is large, there is a lack of understanding on the mechanisms of the fundamental formability behavior, especially the frictional response. The failure mechanisms for powdering have been extensively studied, and they are well characterized, but the extent of their characterization addresses only to the effect of the intermetallic distribution and composition to the powdering, but there are no post processing descriptions that could reduce the failure. The increase of coefficient of friction with the presence of the $\zeta$-phase is also known, but the fundamental explanation of this behavior is absent or qualitatively attributed to assumed mechanical properties of the intermetallic phase.

This dissertation has the objective of describing the basic mechanisms for the frictional response and powdering behavior change with the intermetallic phase distributions

on the surface of the coated sheet steel. Understanding the mechanism will allow for a better selection of processing parameters for a specific forming requirement, either to lower powdering or the coefficient of friction.

The philosophy under which the work for this dissertation was performed is based on the premise that:

*Friction and formability (formability as measured by powdering and flaking) are controlled by the distribution of the intermetallic phases in the galvannealed coating. Understanding the way the distribution of intermetallic phases affects the frictional response and the powdering, will allow to model and predict the forming behavior of the galvannealed coated steel sheet.*

The hypotheses under which this dissertation has been written is the following:

*The amount of $\zeta$-phase dictates the formability of the galvannealed coated steel sheets. The deformable $\zeta$-phase accommodates the normal stress by increasing the contact area. The increase of contact area results in an increase of the coefficient of friction. Similarly, the increase in contact area represents a decrease of the real normal and shear stresses, preventing the damage of the lower layer of the coating, the $\delta$-phase.*

22

# CHAPTER 3
# EXPERIMENTAL METHODOLOGY

This chapter introduces and describes the experimental techniques used in the characterization of galvannealed (GA) coatings. It is divided into three sections; the first section introduces the materials of study in this dissertation. The second section presents the characterization techniques used to identify the intermetallic phases in the coating. The third section presents the mechanical testing performed on the coatings to characterize the friction, powdering, and mechanical behaviors of the coatings. The results of the experimental methodology will be presented in the next chapter, Experimental Results, in which an extensive characterization of the coatings is included.

## 3.1 Experimental Materials

The criteria for the materials selection for this study were availability and Advanced Steel Processing and Product Research Center (ASPPRC) sponsor preference. Traditionally, extra low carbon steels, which had evolved into present interstitial-free (IF) steels, have been the most popular substrate for coated sheet steels. For this reason, most of the galvannealed sheet steels research has been performed on IF steels. IF steels represent a considerable portion of the gross weight in automobile materials, and the study of IF steel of significant importance to the automotive industry. Three sponsor companies of the ASPPRC provided the GA sheets for this study. All the steels shared some commonality, in that they are Ti-stabilized or Ti-Nb-stabilized IF steel.

International Steel Group, Inc., (ISG, now MITTAL Steel) provided a series of 48 GA sheets, measuring 915 x 1496 mm (36 x 59 in), from an experimental coil. By varying the furnace conditions on the annealing process, four very distinctive intermetallic coating distributions were produced. The characteristics of these sheets, different coating

characteristics within the same substrate coil, make an excellent material for this study, and they represent the principal material for this study.

United States Steel (USS) provided another series of 80 sheets measuring 915 x 1448 mm (36 x 57 in) from two experimental coils produced a few years ago, with three different intermetallic coating distributions. The last set of sheets provided by AK Steel Corporation, consisted of 50 smaller sheets measuring 457 x 610 mm (18 x 24 in) of two commercially produced coated sheets. The AK Steel sheets are used to compare results to a commercially available product and will not be substantially presented in the main discussion.

## 3.1.1 Substrates

The ISG sheets are Ti-stabilized IF steel, with a thickness of 0.61 mm (0.0240 in.). The USS sheets are Ti-Nb -stabilized IF steel, with a thickness of 0.75 mm (0.0295 in.). The AK-S sheets are stabilized IF steel, and there is no information of the exact chemistry of the substrate. The chemistry of the ISG and USS substrates is presented in Table 3.1 and Table 3.2. Although having different sheets from different providers, the substrates share the same fundamental characteristic, and the only difference that could exist among them is a processing difference. The light optical micrographs (LOM) of the substrates presented a common structure of the IF steels, clean ferrite grains with the Ti and Nb carbide precipitates. The LOM of the substrates are presented in Figure 3.1.

Mechanical properties were measured for the ISG and USS sheets. ASTM standard size E-8 tensile samples [40] were machined, parallel, perpendicular, and at 45° to the rolling direction. Careful machining was performed to produce parallel edges for R-value measurements. The samples were tested at a rate of 12.7 mm/min (0.5 in/min). Yield strength, ultimate tensile strength, uniform elongation, total elongation, n-value (determined for the strain range of 0.05 to 0.10) and K-values were calculated for the test results. A fracture mechanics strain gage was used to measure the width of the sample while the tensile test was performed, and R-values were calculated at a true strain of 0.15. The summary of

mechanical properties of the sheets is presented in Table 3.3 and Table 3.4. The samples are labeled after their coating characteristics which will be described further in the dissertation.

**Table 3.1**          **Chemistry of the substrate steels, ISG sheets.**

| Element weight percent | | | | | | | |
|---|---|---|---|---|---|---|---|
| C | Mn | P | S | Si | Cu | Ni | Cr |
| 0.002 | 0.05 | 0.009 | 0.007 | 0.008 | 0.008 | 0.01 | 0.02 |
| Mo | V | Ti | Al | B | Nb | N | |
| 0.005 | 0.001 | 0.055 | 0.03 | 2E-04 | 0.002 | 0.005 | |

**Table 3.2**          **Chemistry of the substrate steels, USS sheets.**

| Element weight percent | | | | | | | |
|---|---|---|---|---|---|---|---|
| C | Mn | P | S | Si | Cu | Ni | Cr |
| 0.003 | 0.18 | 0.009 | 0.006 | 0.006 | 0.014 | 0.011 | 0.02 |
| Al | Ti | Nb | B | N | | | |
| 0.047 | 0.035 | 0.032 | <.0002 | 0.003 | | | |
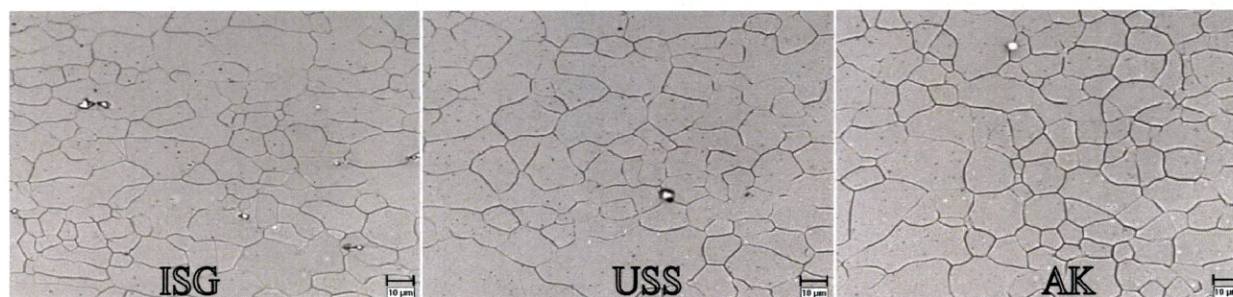


**Figure 3.1**          **Light optical micrographs of the ISG, USS, and AK substrates.**

**Table 3.3        Summary of mechanical properties of the ISG sheets.**

| | Tensile Strength [MPa] | Yield Strength [MPa] | $e_u$ | $e_{total}$ | n-value | K-value | R |
|---|---|---|---|---|---|---|---|
| **Sample: I-00** | | | | | | | |
| parallel to RD | 302 | 124 | 27 | 47 | 0.29 | 88.8 | 1.94 |
| diagonal to RD | 306 | 133 | 26 | 45 | 0.30 | 91.4 | 1.91 |
| perpendicular to RD | 301 | 130 | 22 | 42 | 0.28 | 86.9 | 2.83 |
| average R value | | | | | | | 2.15 |
| **Sample: I-04** | | | | | | | |
| parallel to RD | 295 | 119 | 28 | 50 | 0.31 | 88.8 | 1.79 |
| diagonal to RD | 298 | 127 | 27 | 47 | 0.30 | 89.9 | 2.13 |
| perpendicular to RD | 290 | 124 | 23 | 42 | 0.28 | 87.1 | 2.81 |
| average R value | | | | | | | 2.24 |
| **Sample: I-92** | | | | | | | |
| parallel to RD | 289 | 113 | 28 | 51 | 0.31 | 88.0 | 2.02 |
| diagonal to RD | 293 | 124 | 26 | 51 | 0.30 | 88.4 | 2.83 |
| perpendicular to RD | 286 | 119 | 26 | 47 | 0.29 | 88.3 | 2.83 |
| average R value | | | | | | | 2.63 |
| **Sample: I-99** | | | | | | | |
| parallel to RD | 289 | 115 | 26 | 54 | 0.31 | 88.1 | 2.59 |
| diagonal to RD | 290 | 120 | 26 | 52 | 0.31 | 87.6 | 2.42 |
| perpendicular to RD | 288 | 121 | 26 | 51 | 0.31 | 88.4 | 3.22 |
| average R value | | | | | | | 2.66 |

**Table 3.4**          **Summary of mechanical properties of the USS sheets.**

| | Tensile Strength [MPa] | Yield Strength [MPa] | $e_u$ | $e_{total}$ | n-value | K-value | R |
|---|---|---|---|---|---|---|---|
| Sample: U-02T | | | | | | | |
| parallel to RD | 311 | 154 | 25 | 40 | 0.26 | 86.2 | 1.95 |
| diagonal to RD | 309 | 165 | 25 | 44 | 0.27 | 86.8 | 2.12 |
| perpendicular to RD | 310 | 164 | 24 | 42 | 0.27 | 86.8 | 2.19 |
| average R value | | | | | | | 2.10 |
| Sample: U-93T | | | | | | | |
| parallel to RD | 307 | 144 | 26 | 44 | 0.28 | 87.9 | 1.69 |
| diagonal to RD | 307 | 152 | 25 | 44 | 0.27 | 86.8 | 2.06 |
| perpendicular to RD | 307 | 150 | 24 | 45 | 0.28 | 88.3 | 2.66 |
| average R value | | | | | | | 2.12 |
| Sample: U-99T | | | | | | | |
| parallel to RD | 313 | 157 | 25 | 44 | 0.27 | 87.7 | 1.72 |
| diagonal to RD | 311 | 164 | 25 | 43 | 0.27 | 86.6 | 1.78 |
| perpendicular to RD | 312 | 166 | 24 | 42 | 0.27 | 87.8 | 2.58 |
| average R value | | | | | | | 1.97 |
| Sample: U-GI (galvanized) | | | | | | | |
| parallel to RD | 316 | 146 | 26 | 46 | 0.30 | 93.1 | 2.38 |
| diagonal to RD | 313 | 154 | 25 | 45 | 0.28 | 90.5 | 2.12 |
| perpendicular to RD | 312 | 156 | 25 | 46 | 0.29 | 91.3 | 2.80 |
| average R value | | | | | | | 2.36 |

## 3.1.2 Coatings

The coatings of the ISG sheets consist of four different surface intermetallic distributions, from pure δ-phase at the surface, two mixtures of δ+ζ, and one coating with pure ζ-phase at the surface. Table 3.5 presents a summary of the coating compositions of the ISG sheets. The ISG sheets did not have a temper roll post treatment as would be found in a commercial sheet. This special characteristic will, 1) appear in the roughness measurements, 2) modify the friction characteristics, and 3) serve to create a better understanding of the frictional response.

The coatings of the USS sheets consist of three different surface intermetallic distributions, one with a minimal fraction of ζ-phase at the surface, one with a mixture of δ+ζ at the surface, and a third coating with pure ζ-phase at the surface. These coatings had been temper rolled, in contrast with the ISG. The summary of coating characteristics is presented in Table 3.5.

The coatings of the AK sheets consist of two different surface intermetallic distributions, one is a mixture of δ+ζ phase where the δ-phase predominates, and the second is another mixture of ζ+δ phase where the ζ-phase predominates at the surface coating. These sheets are commercial product and were temper rolled. The coating compositions expressed as Fe weight percent in the coating, and the coating mass are presented in Table 3.5. In the LOM of the cross sections as well as in the scanning electron microscope secondary electron (SEM-SE) images, it can be observed the distributions of the intermetallic δ and ζ-phases on the surface. In the LOM, in the coatings containing ζ-phase, appears as the gray phase on the surface, while in the SEM-SE images the ζ-phase appears as the bigger grains with a rectangular shape. The LOM of the cross sections of the coatings are presented in Figure 3.2, Figure 3.3 and Figure 3.4. SEM-SE images of the surface of the coatings are presented in Figure 3.5, Figure 3.6 and Figure 3.7

28

Table 3.5    GA coating characteristics for the ISG, USS and AK sheets.

| Sheet | Coating mass g/m2 | % Fe | Surface Phases |
|-------|-------------------|------|----------------|
| I-00  | 50.4 | 13.25 | All $\delta$ |
| I-04  | 48.7 | 12.50 | $\delta + \zeta$ |
| I-92  | 51.5 | 10.45 | $\zeta + \delta$ |
| I-99  | 52.1 | 9.50  | All $\zeta$ |
| U-02T | 53.3 | 11.75 | $\delta + \zeta$ |
| U-93T | 53.5 | 10.00 | $\zeta + \delta$ |
| U-99T | 53.0 | 7.80  | All $\zeta$ |
| U-GI  | 50.7 | 0.55  | All $\eta$ |
| A-15T | 62.8 | 8.73  | $\delta + \zeta$ |
| A-85T | 66.6 | 7.50  | $\zeta + \delta$ |
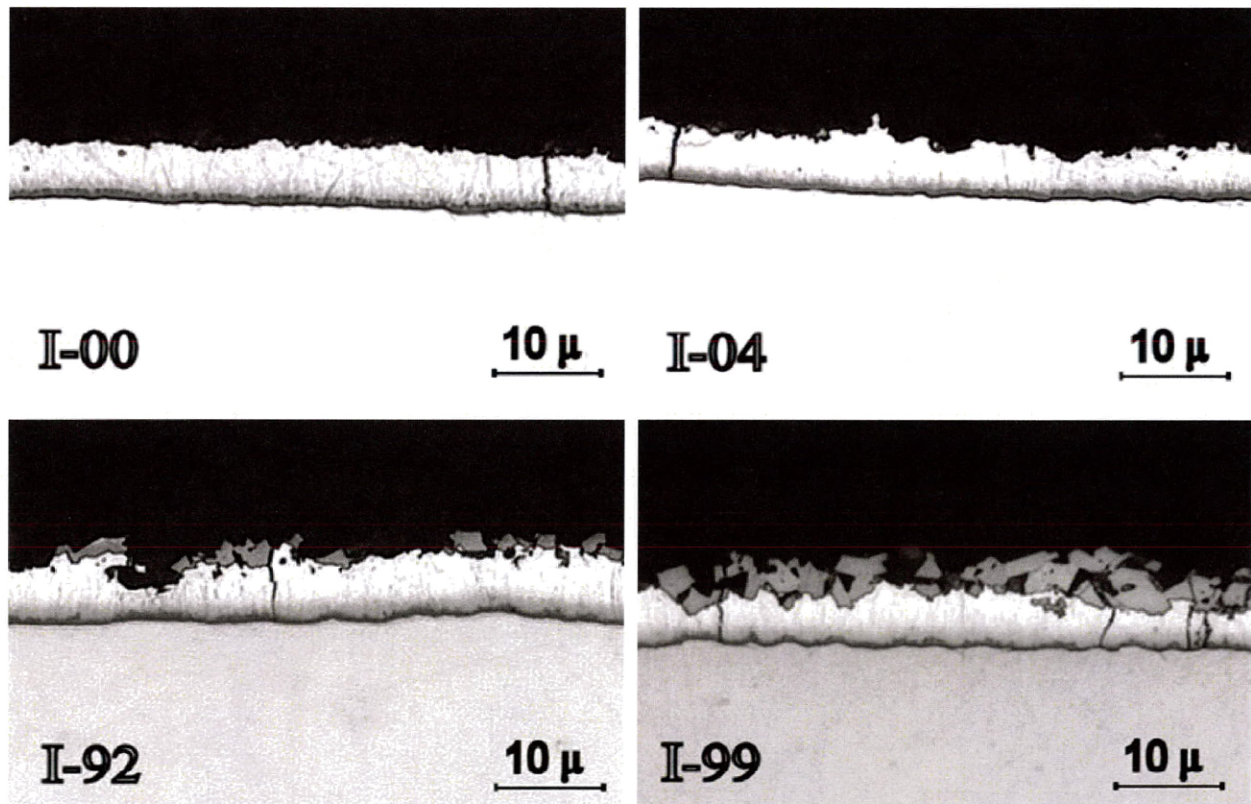


Figure 3.2    Light optical micrographs of the ISG sheets.  Note the amount of $\zeta$-phase at the surface of the coating, increases from sheet I-00 to I-99.

U-02T     10 μ     U-93T     10 μ



U-99T     10 μ
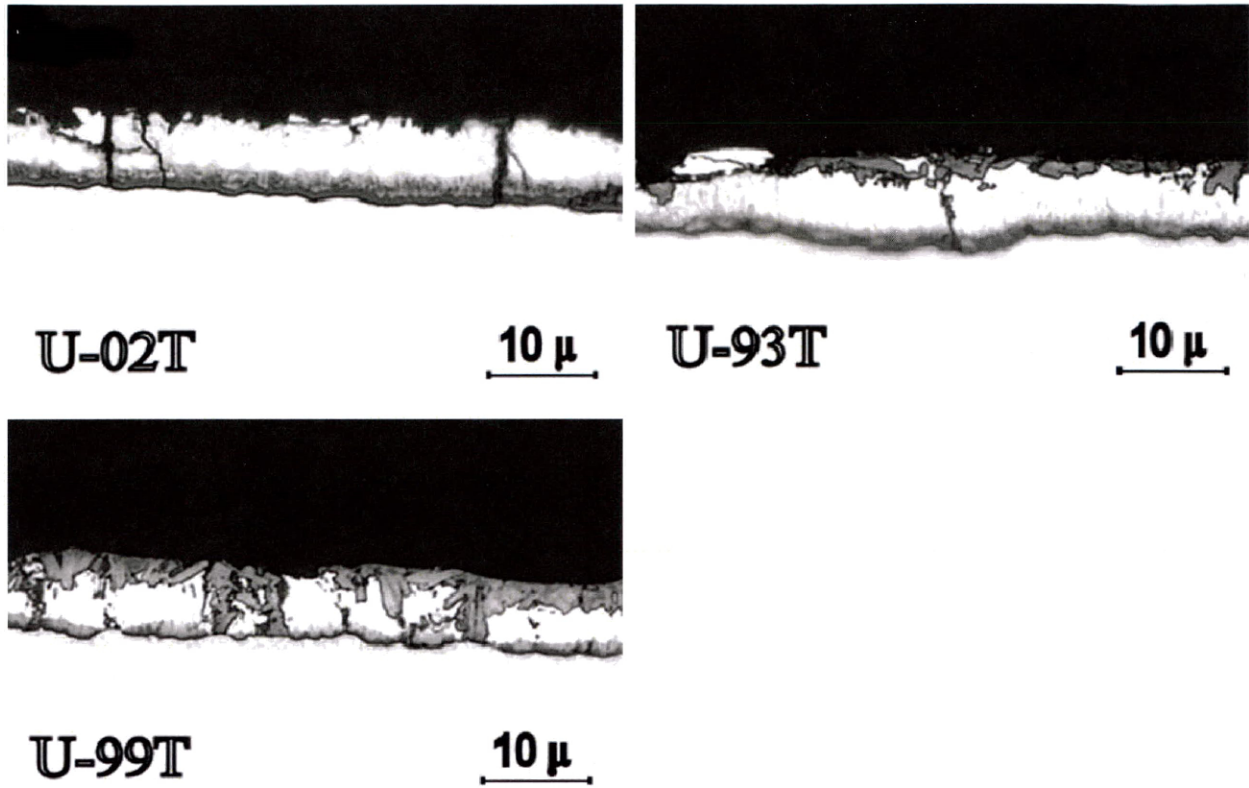
Figure 3.3     Light optical micrographs of the USS sheets. Note the amount of ζ-phase at the surface of the coating increases from sheet U-02T to U-99T. Also note the flat morphology of the ζ-phase at the surface caused by the temper roll.



A-15T     10 μ     A-85T     10 μ
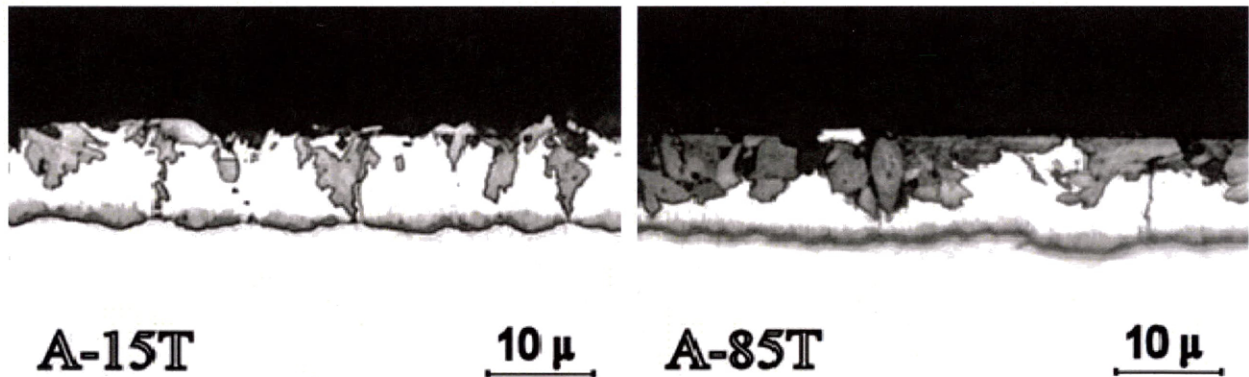
Figure 3.4     Light optical micrographs of the AK sheets. Note the amount of ζ-phase at the surface of the coating increases from A-15T to A-85T.
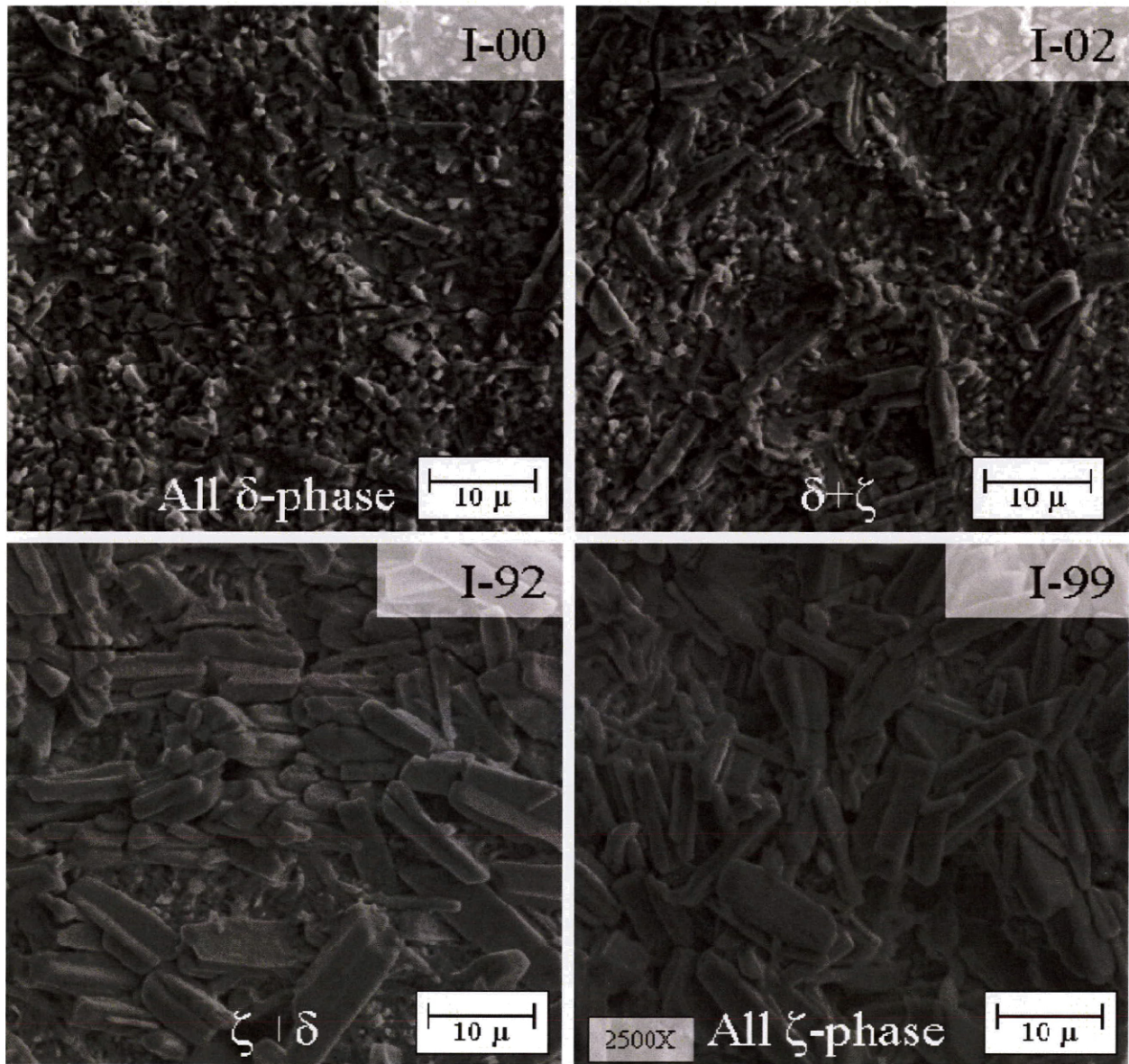
**Figure 3.5** **Scanning electron microscope SE – images of the surface of the ISG sheets.**
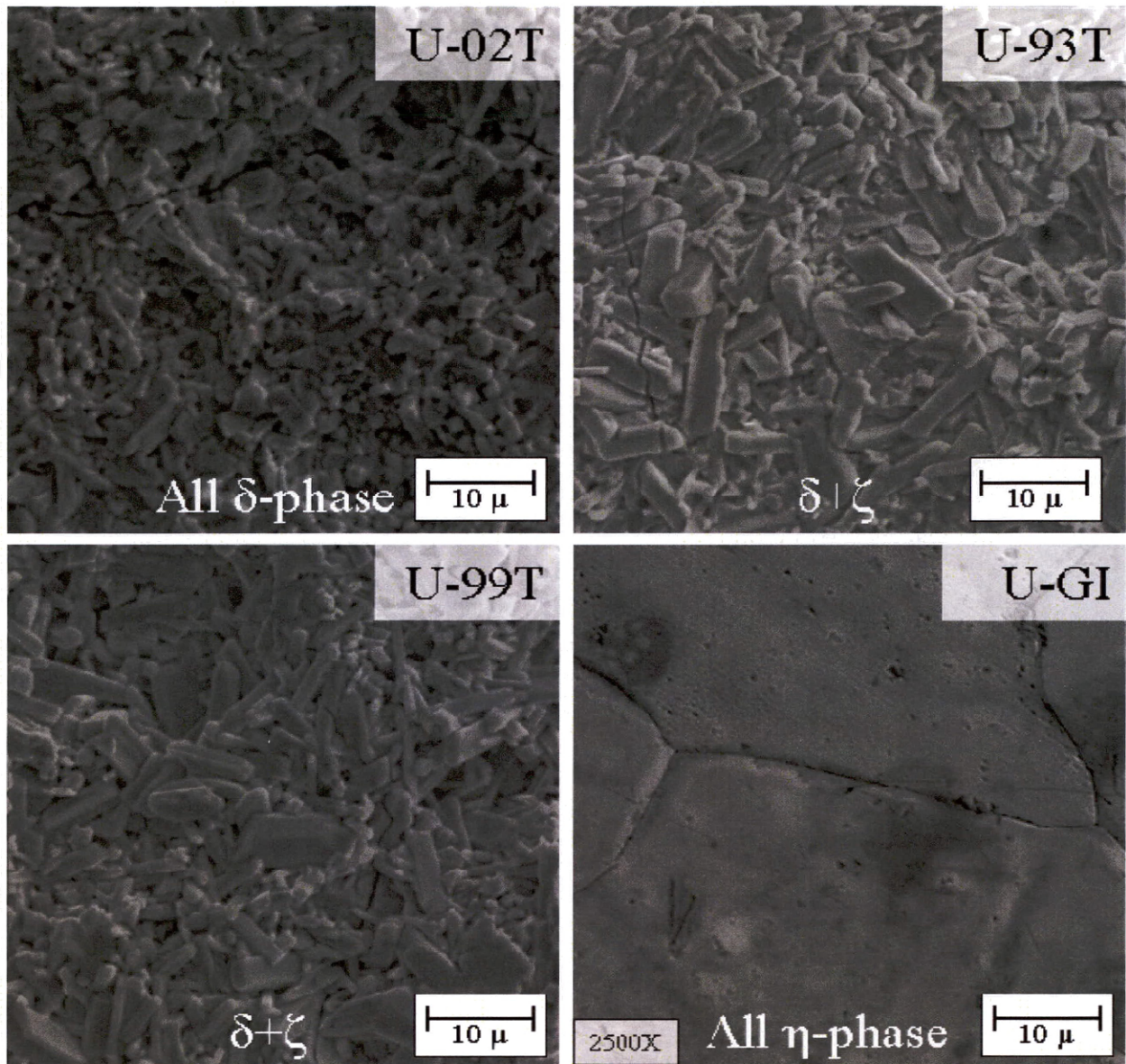
**Figure 3.6** Scanning electron microscope SE – images of the surface of the USS sheets.
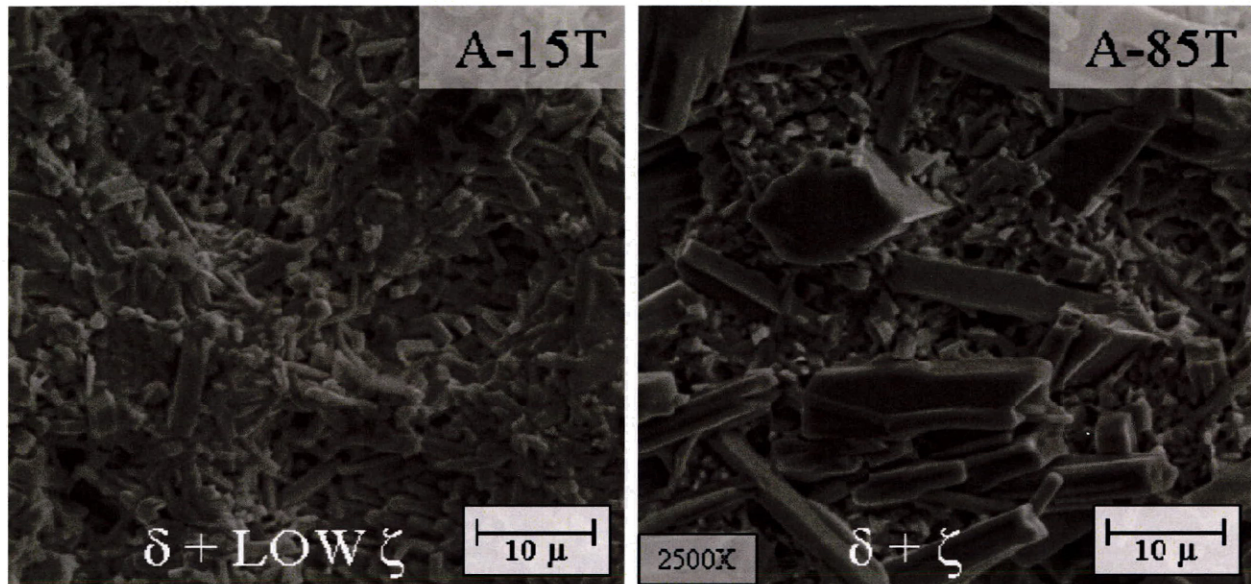
**Figure 3.7**     **Scanning electron microscope SE – images of the surface of the AK sheets.**

## 3.2  Experimental Methods, Coating Characterization Techniques

This section describes the techniques utilized to characterize the GA coatings. The methodologies used to make direct observations such as light-optical microscopy (LOM) and SEM-SE imaging are presented; methodologies used to obtain indirect observations, such as chemical analysis of the coatings are also presented. The techniques were performed on all or some of the coatings in this study, and the results of these characterizations will be presented in the next chapter, Experimental Results.

## 3.2.1  Qualitative observations, light optical micrographs, and electron microscopy

The metallographic preparation of GA coatings, a relatively brittle coating on a relatively soft substrate, is not a simple task. The coatings, with a thickness of about 10 μm, are relatively thin compared to the substrate and are easily rounded (a normal effect caused by the difference in hardness of the steel sample and the mounting media) or scratched out

when a single sheet is processed in a metallographic sample mount. To avoid these difficulties, arrays of samples are mounted together with dummy sheets on its sides for structural support when the grinding and polishing is taking place. Figure 3.8 shows an example of the metallographic mount. The sandwich-like array of samples helps to insure the integrity of the coatings and prevents rounding of the edges.
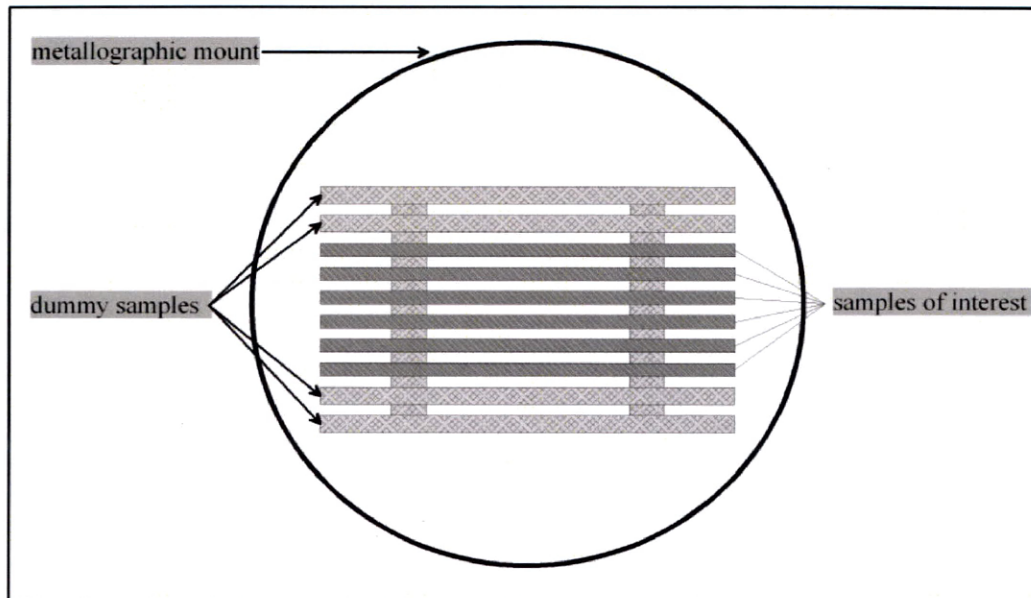


Figure 3.8       Sandwich-like mount for metallographic preparation of cross section of GA sheet steels.

Polishing and grinding of the samples are the most delicate step of the metallographic preparation. The thin, hard, and brittle coating on a bulky, relatively soft substrate creates a series of problems. Rounding is addressed by the mounting of the samples; if a normal procedure is followed the coating will break and be pulled out during the grinding step, and then the metal from the substrate will be smeared into the void left by the pulled coating. Very low pressures and a very slow stable process are needed in order to obtain an acceptably ground and polished sample. This procedure is described by Kilpatrick [41].

There are two etching techniques described by Kilpatrick and Jordan *et al.* [41,42]. The etching of the coatings is complex because it will protect the substrate against any

corrosion attack. In a cross section mount, the coating represents a small fraction of the area, and any etching agent will have to act uniformly yet not too strongly. Also, it is not possible to etch the coating and the substrate at the same time. All GA LOM cross sections in this dissertation were etched with Kilpatrick's solution.

Electron microscopy, using secondary-electron (SE) images and back scattered (BS) images, is another technique that allows for even higher magnifications. For cross-sections, the sample preparations are the same. The sample needs to be coated with gold for better conductivity in the microscope. To obtain a high quality BS-images, the imaging contrast needs to be adjusted carefully. The atomic difference between iron and zinc and the solubilities at which these elements are present in the different intermetallics makes it difficult for them to be differentiated. The topography of the surface of the coating can be easily observed with SE-images; the depth of field is significantly better, when compared to the LOM, as well as the resolution at which small details are resolved.

These two techniques, LOM and SEM, can be applied not only to characterize a coating, but also to make observations of tested sample. Cracking behavior and deformations can be identified easily. Test sample characterization is presented in the next chapter, Experimental Results.

Because the coating is a galvanic protection against corrosion, it needs to be stripped before attempting any etching and to conduct metallographic observations of the substrates. The coating can be stripped using a bath of hydrochloric acid (HCl) with some Fe inhibitor to prevent the substrate from being consumed by the HCl acid. Special care must be taken when working with HCl.

## 3.2.2 Quantitative observations, glow discharge optical emission spectrometer, x-ray diffraction, ICP-MS, and Coulometric stripping

The glow discharge optical emission spectrometer (GD-OES) is an instrument for chemical analysis which is also capable of performing element depth content profiles. In a low vacuum chamber filled with Ar, a potential is applied to the sample, creating an Ar plasma that is targeted to the sample. The bombarding ions act as an atomic mill, dislodging

layers of atoms, or creating an atomic sputtering. The free atoms are excited with the high energy electrons in the plasma, and when the excitation decays, the emitted characteristic radiations are analyzed by the spectrometer. Careful calibration of the equipment makes it possible to quantify the amount of the found elements, and knowing the elements makes it possible to calculate the milling rate, creating a depth element profile. The technique is adequate in theory, but in practice the measurements near the surface (around 0.25 μm) are not very accurate. The analysis technique used in this study is the element profiling through thickness. The name give to such technique is glow-discharge quantitative depth profiling (GD-QDP), and the technique will be referred to by this name in the results chapter and discussions.

One parameter that makes it difficult to obtain a good x-ray diffraction (XRD) pattern is the coating thickness. Selection of angles where the peaks of interest are present, away from the prominent Fe peaks is always needed, and because of the different solubilities of the intermetallics phases present, the peaks often present some broadening. Special techniques have been used successfully such as shallow angle diffraction, in which the lower incident angle of the x-ray gun avoids excessive penetration to the substrate. X-ray diffraction quantitative analysis of the coatings requires extensive experience. In cases where there is a very small volume fraction of a specific phase, the characteristic peak of such phase would pass unnoticed by the inexperience scientist.

Inductively coupled plasma-mass spectrometry (ICP-MS) is the quantitative technique most widely used in industry to characterize GA coatings. This results in information that is accurate but limited to the total amounts of concentration elements. The way this technique works is by stripping the coating off a sample with a standard dimensions in an HCl acid bath with some Fe inhibitor. The sample is weighed before and after the stripping giving a measure of the coating weight per area a direct relationship with its thickness. The coating containing solution is then analyzed, and the concentration of Fe in the coating is measured. This Fe concentration is universally used to describe the GA coating, although it does not give a description of the intermetallic phases present in the

coating, and different processing paths can result in different intermetallic phase distributions.

The final quantitative analysis technique is the coulometric stripping of the coating. This technique consists of the anodic dissolution of the coating at constant imposed current. The potential of the dissolving coating takes on a different value with respect to a reference electrode for each Fe-Zn intermetallics phase in the coating. The potentials are recorded with time and each potential is characteristic of a specific phase. Knowing the rate at which each phase is stripped by the anodic dissolution, the thicknesses of each phase can be estimated [43].

The methods described as quantitative represent indirect measurements where the thicknesses of the phases have to be calculated with a series of assumptions. On the other hand, the methods described as qualitative, especially the cross section images, are the ones where direct measurements of the thicknesses of the phases could be performed. In reality, the GA coating line producers had calibrated a preferred characterizing technique for their use. The direct measurement of the thicknesses of the phases in cross sections is not the most practical, taking into consideration the amount of time it takes to make the metallographic mount. A systematic comparison between a significant number of measurements and any other technique would provide sufficient experience to trust a faster testing technique, like GD-QDP or XRD. In this study, LOM, SEM, GD-QDP, and x-ray diffraction were used to give a defined measure of the phase distributions.

## 3.2.3 Surface intermetallic distribution measurements

Identification of the intermetallic phases present in the coating is possible using the characterization methods described in the previous sections. Any of the techniques could quantify the intermetallic phase distributions, but calibration and significant refinement of the method would be needed. Because of the nature of the coatings studied, some of them having a small amount of $\zeta$-phase on the surface, it was difficult for the characterization techniques to quantify the full range of distributions found in the experimental steels.

Coating I-02 presents traces of $\zeta$-phase on the surface, which can be observed in SE-images (Figure 3.5). LOM of the coating do not show any evidence of the presence of the $\zeta$-phase at the surface (Figure 3.2). XRD patterns do not show all of the peaks for the $\zeta$-phase but does have an indication of the strongest peak angle. The diffraction pattern for I-02 is different when compared to coating I-00, as a small protuberance is present where the peak should be present (XRD patterns are presented in Chapter 4). In the GD-QDP, although inconclusive about the presence of the $\zeta$-phase, the profile shows a slightly higher content of Zn for sample I-02 as compared to I-00 (depth profiles are presented in Chapter 4).

The different characterization methods had contributed evidence of the presence of the $\zeta$-phase on the surface. There is not much consideration for the other phases, as $\delta$-phase is always present in the GA coatings and the $\Gamma$-phase has close to no influence in the frictional response of the sheet.

The $\zeta$-phase on the surface of the coating was quantified using the SEM-SE images. From knowledge of the morphology of the phase, it can be identified and quantified. Digital image processing was used to measure the fraction of the phases present on the surface. Figure 3.9 shows a SEM-SE image of sample I-04, which contains a small fraction of $\zeta$-phase on the surface. The $\zeta$-phase is identified and marked as shown in Figure 3.9 (b). With the use of image processing software developed by the National Institute of Health (NIH) called *Image-J* 44the fraction of the marked $\zeta$-phase is measured. Figure 3.10 shows the quantification example of the same image presented on Figure 3.9. Five images per coating were taken and quantified, and the phase distribution represents the average of the five measurements. In the coatings where the $\zeta$-phase predominated the surface, the $\delta$-phase was selected for identification instead.

38
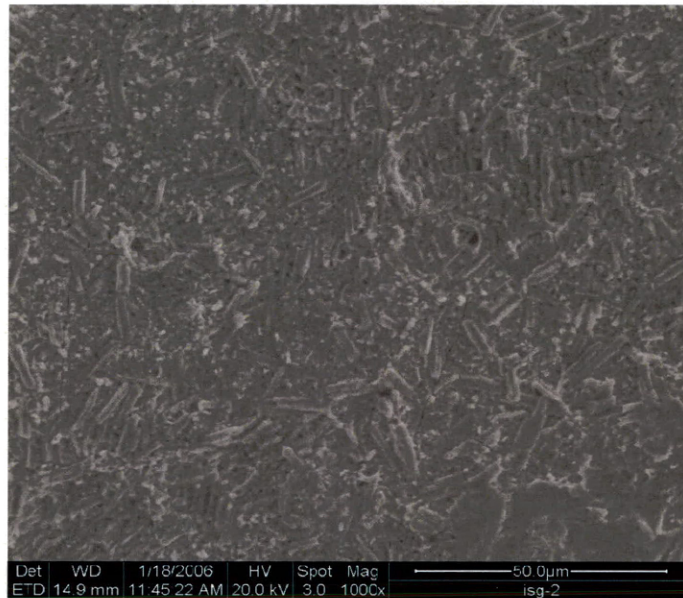
(a)
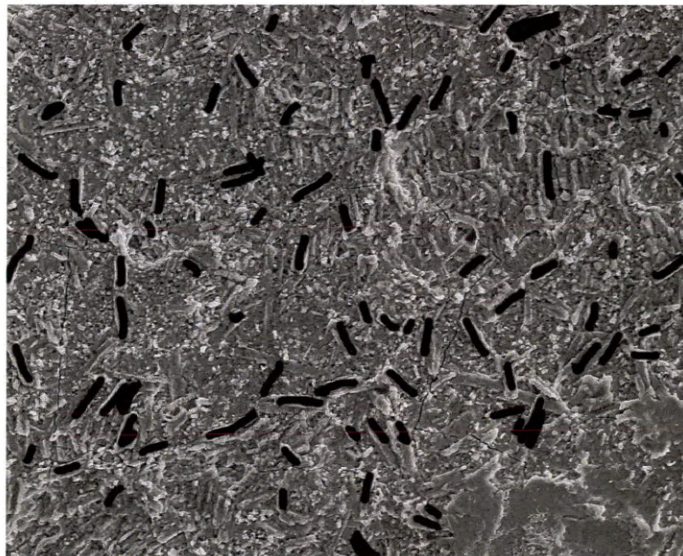


(b)

**Figure 3.9**      **Scanning electron microscope SE-image of sample I-04, with small fraction of $\zeta$-phase present at the surface. (a) Shows the original SE-image; (b) shows the same image with the $\zeta$-phase identified for quantification.**

Threshold: 0-128

Count: 105

Total Area: 45920.000 pixel^2

Average Size: 437.333 pixel^2

Area Fraction: 5.1%

**Figure 3.10 Example of phase quantification from image shown in Figure 3.9**

### 3.2.4 Roughness measurements

Contact surfaces are not perfectly flat; they consist of peaks, valleys and asperities. The roughness of surfaces in contact affects their frictional responses, as the real contact between two surfaces happens at the high points. The size of the asperities and their distribution are important when trying to explain friction behavior.

A surface profiler is the instrument that maps the heights of a surface and registers them either along a line (2D profiler) or along a plane (3D profiler). There are two types of surface profilers. The contact surface profiler uses a stylus tip that makes physical contact with the surface. As the stylus is dragged along the surface, it moves up and down with the topography of the surface, and an electromechanical device registers the up and down movement recording the profile of the surface. This type of device is limited by the radius of curvature of the stylus which dictates the measuring resolution. The other type of profiler is the digital optical profiler. This instrument utilizes an optical interferometer array of lenses, and digital imaging processing to register the different heights of the sample. There are two different techniques, phase-shifting and vertical scanning. For both techniques the same

principle operates: the reflected light is interfered with the incident light to create an interference pattern. In the phase shifting scanning mode, the phase of the incident light is shifted by known amounts, and the reflected light will create a diffraction pattern according to the heights of the surface; this scanning mode allows for a very high resolution of around 0.1 nm. The vertical mode utilizes a short coherent white light that creates interference fringes at very shallow depths of field (or only when the surface is in focus). The interferometer is lowered from above the focal point, down focusing every point of the surfaces, and the constant digital scan registers the appearance of fringes by registering the height of each point of the surfaces; the resolutions that can be obtain with this mode are around 3 nm. The lateral resolution is limited by the magnification of the lens used and the digital camera resolution.

The roughness measurements presented in this dissertation were obtained using a WYKO 3D surface profiler with Version 32 software developed by Veeco Instruments, Inc. The scans were performed in VSI mode, using a 5 X magnification objective and an internal objective of 0.5 X for a total magnification of 2.5 X, which represent a scan of 1.9 x 2.4 mm and a sample resolution of 3.32 μm.

The samples did not receive any special preparation prior to the scans, but were degreased with acetone. A magnetic stage was used to secure the samples during scanning.

There are many parameters that can be calculated from the surface profile. Table 3.6 presents a description of the different parameters that can be calculated from the profile. Each of these parameters represents special characteristics of the surface. The most common ones are the $R_a$ and $R_q$, which represent the arithmetic average roughness and its root mean square respectively. $R_q$ is a comparable quantity to the standard deviation when the surface presents a normal distribution. The $R_t$ parameter gives a measure of the difference between the highest and the lowest point in a scan, this parameter is very useful as means to give a sense of the long range variances in a surface, but it needs to be interpreted with care as it can be easily affected by noise. The $R_{sk}$ and $R_{ku}$, the skewness and the kurtosis respectively, are parameters of third and fourth order that give a sense of the distribution of the samples. Skewness indicates if a profiles is predominated by valleys or peaks, while the kurtosis

provides a sense of the distribution, for example, does it approach a normal distribution or not.

## 3.2.5 Contact Area Measurements

During a friction test, the real contact of area is of great importance. For the development of the friction model presented in this dissertation, the real contact areas of the tested samples as well as the contact area of the as received samples that were temper rolled were measured.

There are different ways to measure the real contact area. The simplest way is to measure the fraction of contact area by direct observation of the surface. SEM-SE images have proven to be a reliable way to measure the fraction of the contact area in tested samples. One disadvantage of this technique is that it is time consuming, because of taking samples in and out of the vacuum chamber of the microscope. Micro photography is another option, but careful calibration of the images taken, as well as illumination makes it a complicated option, and not overly accurate, since lighting has a considerable effect on the outcome of the measurements. Another way to measure the real contact area is by analysis of the 3D surface profiles of the tested samples.

Sheets like ISG which were not temper rolled, the distribution of the heights of their surface profiles has a normal distribution. The normal distribution is a result of a random distribution of heights, an expected behavior found in natural processes, such as the growth of the intermetallics on the surface of the coating. Figure 3.11 presents the 3D profile of the I-99 sheet. A normal uniform distribution can be express as:

[ Eq. ] 3-1
$$P(x) = \frac{1}{\sigma\sqrt{2\pi}} e^{-(x-\mu)^2/2\sigma^2}$$

where $P(x)$ is the normalized distribution with a mean value of $\mu$ and a standard deviation $\sigma$. In the profile distribution, the mean value $\mu$, does not have much significance as it is normally set by the measuring system. The standard deviation $\sigma$, represents the extent of variation of the profile.

42

**Table 3.6**      **Definition and description of roughness parameters (from VEECO Tech manuals).**

| Term | Definition | Calculation | Use Ra |
|---|---|---|---|
| $R_a$ | Roughness average is the main height as calculated over the entire measured length or area. It is quoted in micrometers or micro-inches. $R_a$ is calculated per the ANSI B46.1 standard. | Two-dimensional $R_a$ $$R_a = \frac{1}{n}\sum_{i=1}^{n}\left\|Z_i - \overline{Z}\right\|$$ Three-dimensional $R_a$ $$R_a = \frac{1}{MN}\sum_{j=1}^{N}\sum_{i=1}^{M}\left\|Z_{ij}\right\|$$ where M and N = number of data points in X and Y, and Z is the surface height relative to the mean plane. | $R_a$ is typically used to describe the roughness of machined surfaces. It is useful for detecting general variations in overall profile height characteristics and for monitoring an established manufacturing process. |
| Rq | The Root means square (rms) average between the height deviations and the mean line/surface, taken over the evaluation length/area. The parameters "RMS" and "$R_q$" are equivalent in Wyko® Vision® and are computed using the same equation. | Two-dimensiona $R_q$ $$R_q = \sqrt{\frac{1}{n}\sum_{i=1}^{n}\left(Z_i - \overline{Z}\right)^2}$$ Three-dimensional $R_q$ $$R_q = \sqrt{\frac{1}{MN}\sum_{j=1}^{N}\sum_{i=1}^{M}Z^2\left(x_i,y_j\right)}$$ | RMS roughness describes the finish of optical surfaces. It represents the standard deviation of the profile heights and is used in computations of skew and kurtosis. |
| $R_p$ , $R_v$ | Maximum profile peak height and Maximum profile valley depth are the distances from the mean line/surface to the highest/lowest point in the evaluation length/area. | Measured | Peak height provides information about friction and wear on a part. Valley depth provides information about how a part might retain a lubricant. |
| $R_t$ | Maximum height is the vertical distance between the highest and lowest points in the evaluation length/area. | $$R_t = R_p + R_v$$ | Maximum height describes the overall roughness of a surface. |
| $R_z$ | The Average maximum profile of the ten greatest peak-to-valley separations in the evaluation area. Vision excludes an 11 x 11 region around each high (H) or low (L) point such that all peak or valley points won't emanate from one spike or hole. | $$R_z = \frac{1}{10}\left[\sum_{i=1}^{10}H_i - \sum_{j=1}^{10}L_j\right]$$ | $R_z$ is useful for evaluating surface texture on limited-access surfaces such as small valve seats and the floors and walls of grooves, particularly where the presence of high peaks or deep valleys is of functional significance. |
| $R_{sk}$ | Skewness is a measure of the asymmetry of the profile about the mean line. Negative skew indicates a predominance of valleys, while positive skew is seen on surfaces with peaks. | $$R_{sk} = \frac{1}{nR_q^3}\sum_{i=1}^{n}\left(Z_i - \overline{Z}\right)^3$$ | $R_{sk}$ illustrates load carrying capacity, porosity, and characteristics of non-conventional machining processes. Negative skew is a criterion for a good bearing surface. |
| $R_{ku}$ | Kurtosis is a measure of the distribution of spikes above and below the mean line. For spiky surfaces, $R_{ku}$ > 3; for bumpy surfaces, $R_{ku}$ < 3; perfectly random surfaces have kurtosis 3. | $$R_{ku} = \frac{1}{nR_q^4}\sum_{i=1}^{n}\left(Z_i - \overline{Z}\right)^4$$ | Kurtosis describes machined surfaces and is rarely used for optical surfaces. It is sometimes specified for the control of stress fracture. |

There are many ways to represent a profile distribution. The histogram is a count distribution of heights along the surface. Figure 3.12 shows the histogram of the 3D profile of sheet I-99. Bearing ratio curves first developed by Abbott and Firestone [45], represent the cumulative probability distribution of the histogram and have been commonly used to analyze the evolution of surfaces in contact which are subjected to wear. Figure 3.13 presents the bearing ratio of the profile of sample I-99. It is worth noting that the bearing ratio curves are usually presented with the fraction of the distribution on the abscissa in a descending order, while the height is plotted on the ordinate axis.

Another way to present a distribution is as an ordered response or probability plot, Figure 3.14. The ordered response is the inverse of the standard normal cumulative distribution which has a mean of 'zero' and a standard deviation of 'one'. The ordered response is calculated from the cumulative probability distribution. The significance of the probability plot is that if the plot is a straight line, the distribution is a normal distribution. The inverse slope of the curve represents the standard deviation of the distribution, and as discussed earlier, the $R_q$ is a measure of the standard deviation of the profile. Example of this relationship is that sample I-99 had a $R_q$ value of 3.75 $\mu$m, while the inverse slope of the probability plot is 3.79.

44

Mag: 2.5 X
Mode: VSI

**3D Plot**

Date: 11/05/2004
Time: 14:58:12

**Surface Statistics:**
Ra: 3.01 um
Rq: 3.75 um
Rz: 21.23 um
Rt: 21.31 um

**Set-up Parameters:**
Size: 736 X 480
Sampling: 3.32 um

**Processed Options:**
Terms Removed:
Cylinder & Tilt
Filtering:
None
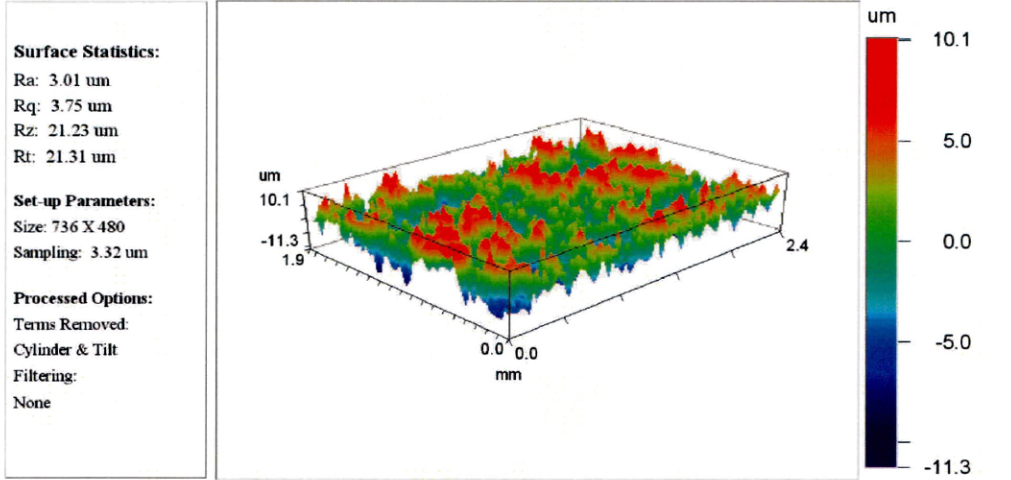
Title: isg-4
Note: 0.5X scan
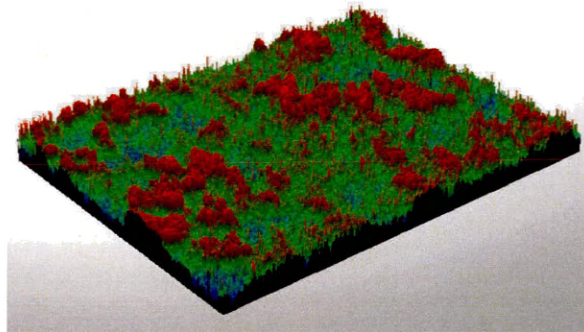


**Figure 3.11      Three dimensional surface profile of sample I-99.**
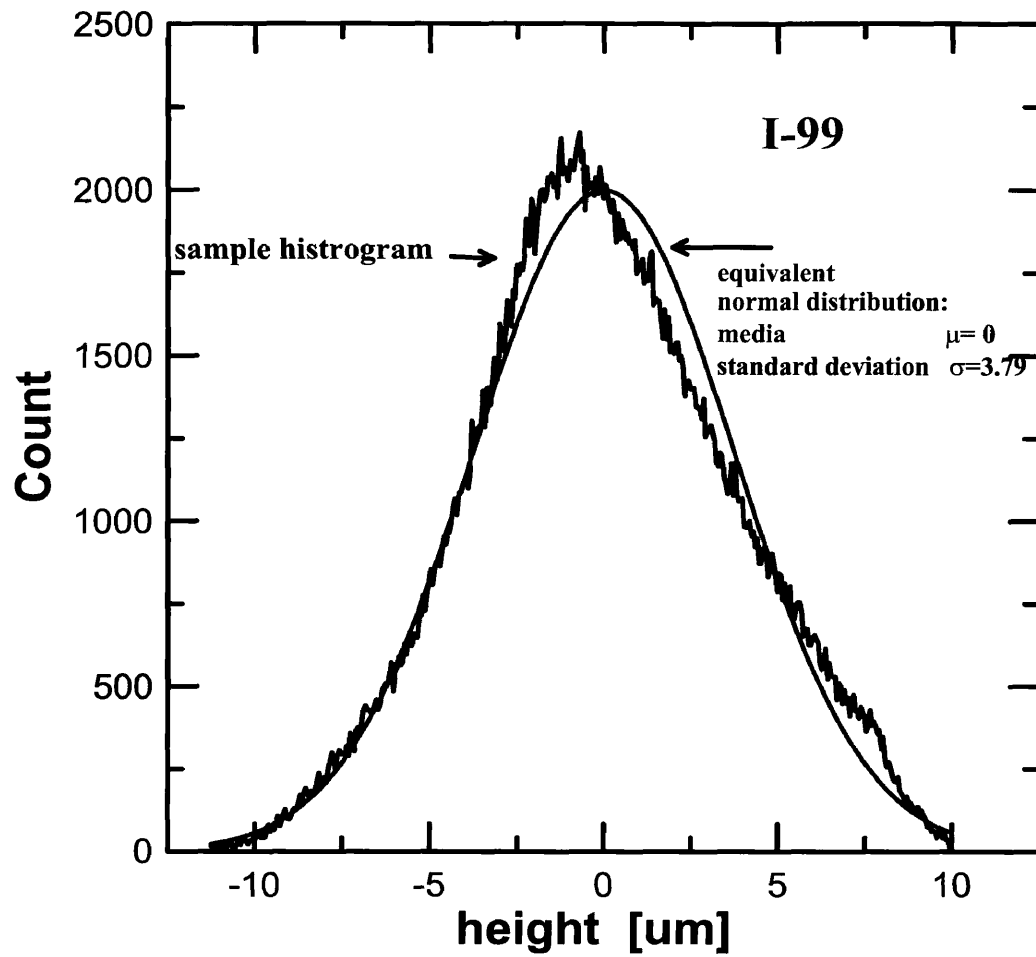
**Figure 3.12**  Histogram of surface profile of sample I-99.
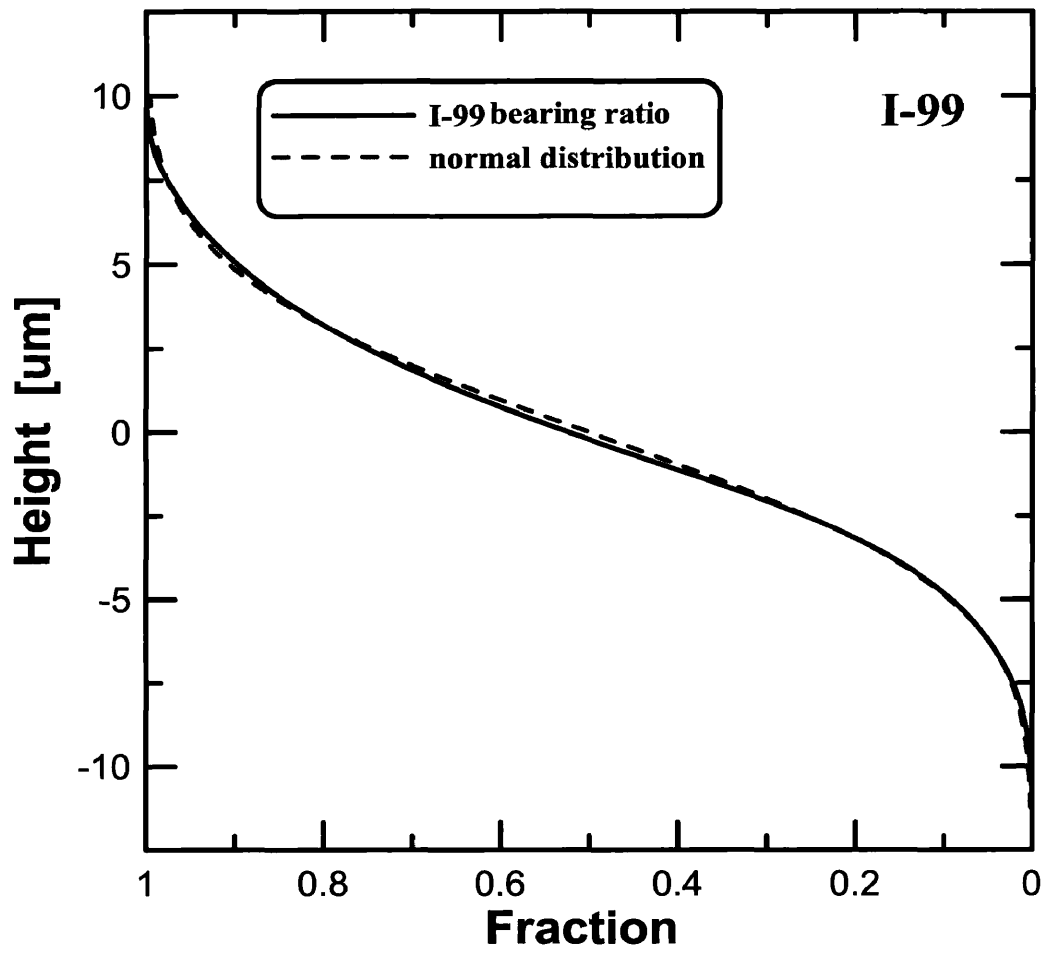
**Figure 3.13**        **Bearing ratio curve for sample I-99.**
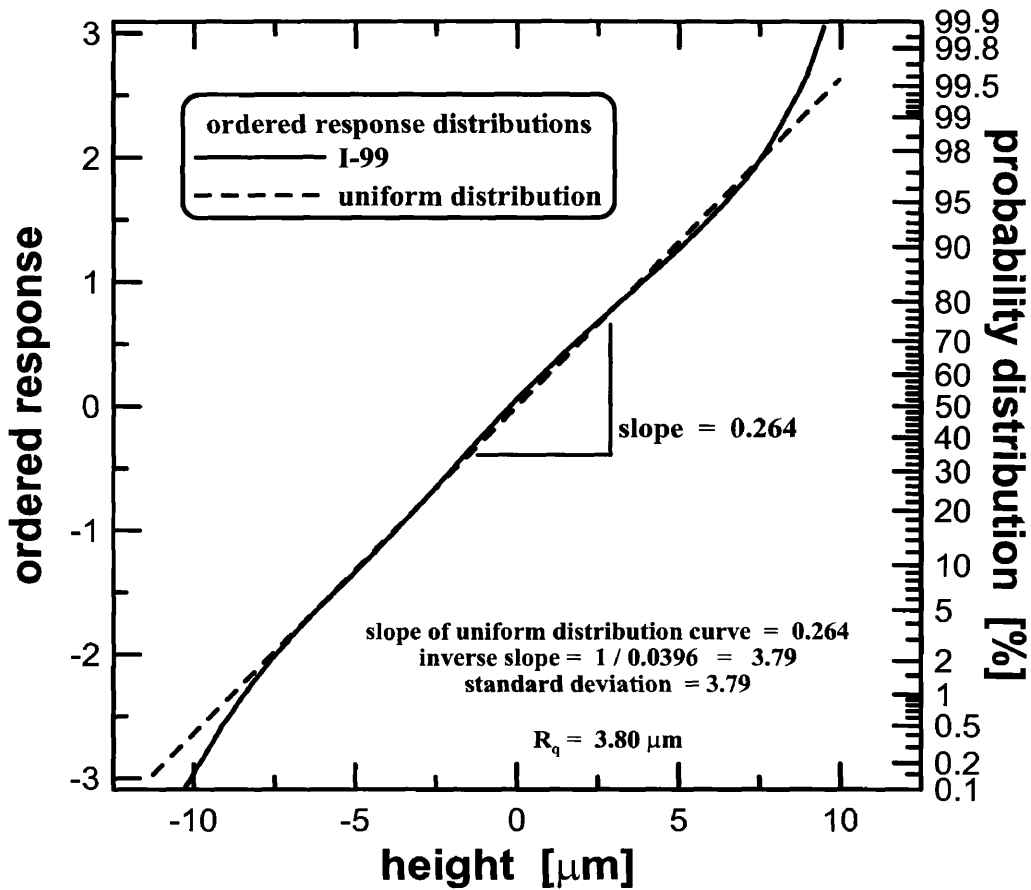
**Figure 3.14**      **Probability plot for the profile distribution of sample I-92.**

In the ISG tested samples, their surface profile histograms exhibited a bimodal behavior. Figure 3.15 shows a 3D profile of a FDT tested sample of I-99 sheet. In the 3D image of the surface the contact area is shown in dark sections. Figure 3.16 presents the normalized distribution of the same sample, which is the same histogram with the area under the curve set equal to one. Each hump in the curve represents a different distribution, the widest distribution on the right, represents the distribution of the un-touched sample, while the narrow distribution of the left represents the flat areas caused by the contact with the die during the friction test. Each hump can be described by its own distribution. In the example, the wide hump, representation of the un-touched part of the sample, can be represented by a normal distribution with a standard deviation $\sigma=2.45$ $\mu$m. The narrow part can be represented

by a second distribution with a standard deviation of $\sigma=0.86$ μm. In the bearing ratio curve of the tested sample profile presented in Figure 3.17, the contact is indicated by the change in slope of the curve. In the normal distribution curve, the slope decreases continuously from the fraction value of 1 towards the middle part of the curve, while in the bearing ratio curve of the tested sample, there is a change of slope at a fraction ~ 0.79.



Title: f4ic-25 -3
Note: fdft, 8.08 MPa
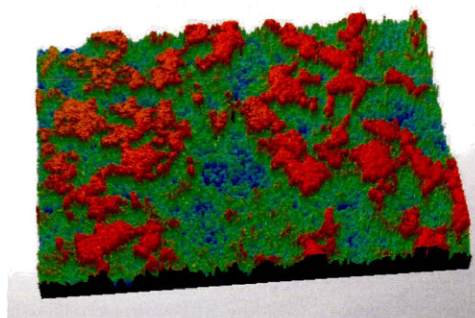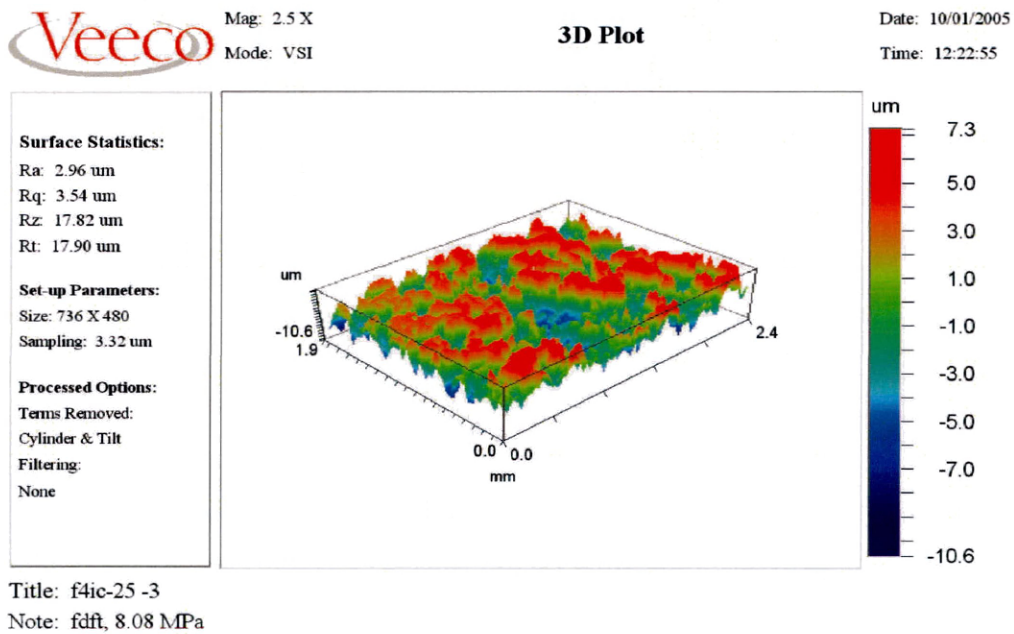


**Figure 3.15**       **Three dimensional surface profile of flat die tribometer tested sample I-99.**
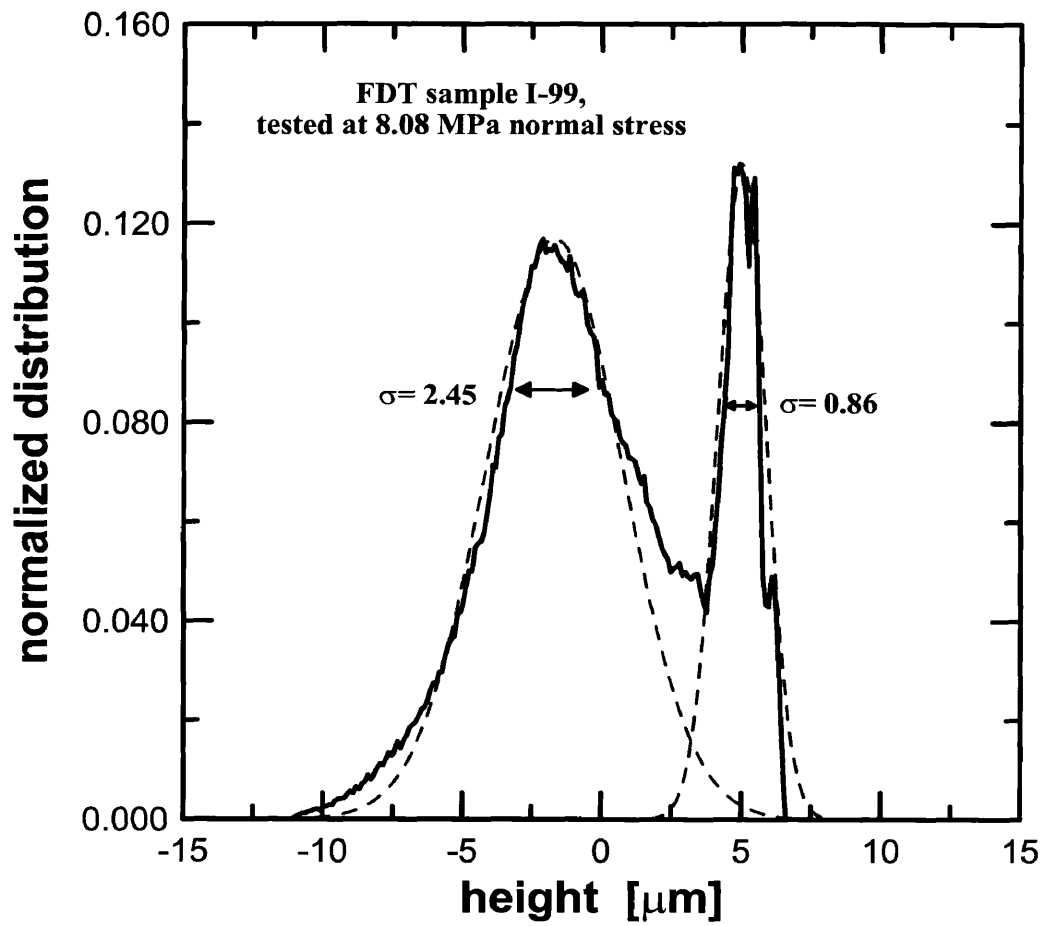
**Figure 3.16**    Histogram of flat die tribometer tested sample I-99 shown in Figure 3.17. The histogram in this figure has been normalized where the area under the curve equals one.
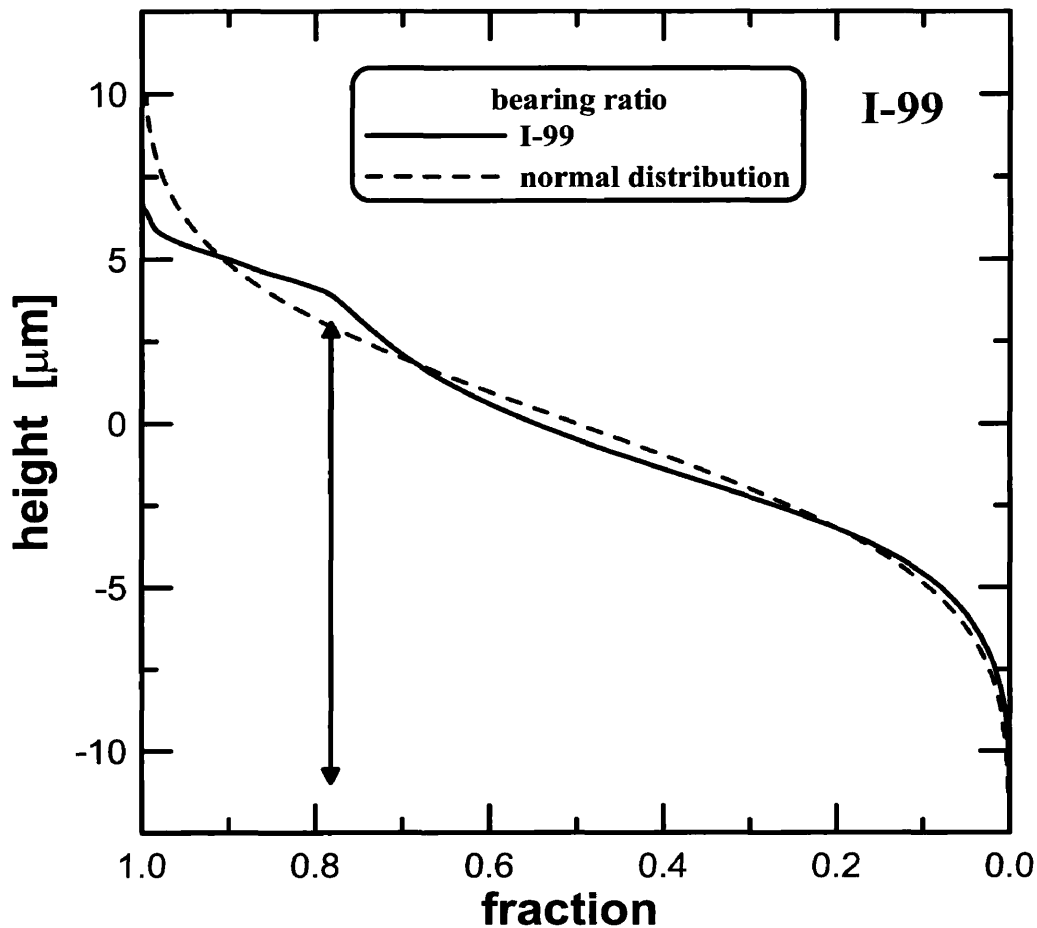
**Figure 3.17**    Bearing ratio curve of flat dies tribometer sample I-99 tested at a normal stress of 8.08 MPa.  Notice the change of slope in the curve, indication of contact area.

When the ordered response is calculated the two distributions can be observed in the probability plot, as a change in slope as seen in Figure 3.18.  The change in slope represents a change in the standard deviation.  The slope of the first portion of the curve has a value of 0.253, the inverse of the slope is 3.90.  Although this value is somewhat higher than the standard deviation presented in the distribution for the un-touched portion of Figure 3.16, it is similar to the standard deviation of 3.75 μm of the as-received sample.  The second slope of the probability plot represents the standard deviation of the second distribution, the distribution of the flat spots of the surface, corresponding to the contact area.  The real

contact area can be considered as the fraction of the profile which contains a different distribution as compared to the un-touched fraction. In the example, the slope of the probability plot changes at around 79 %, indicating that the un-touched percent of the profiles is 79 %, and the remaining 21 % represents the portion of the profile that contains the flat features, or the real contact area.
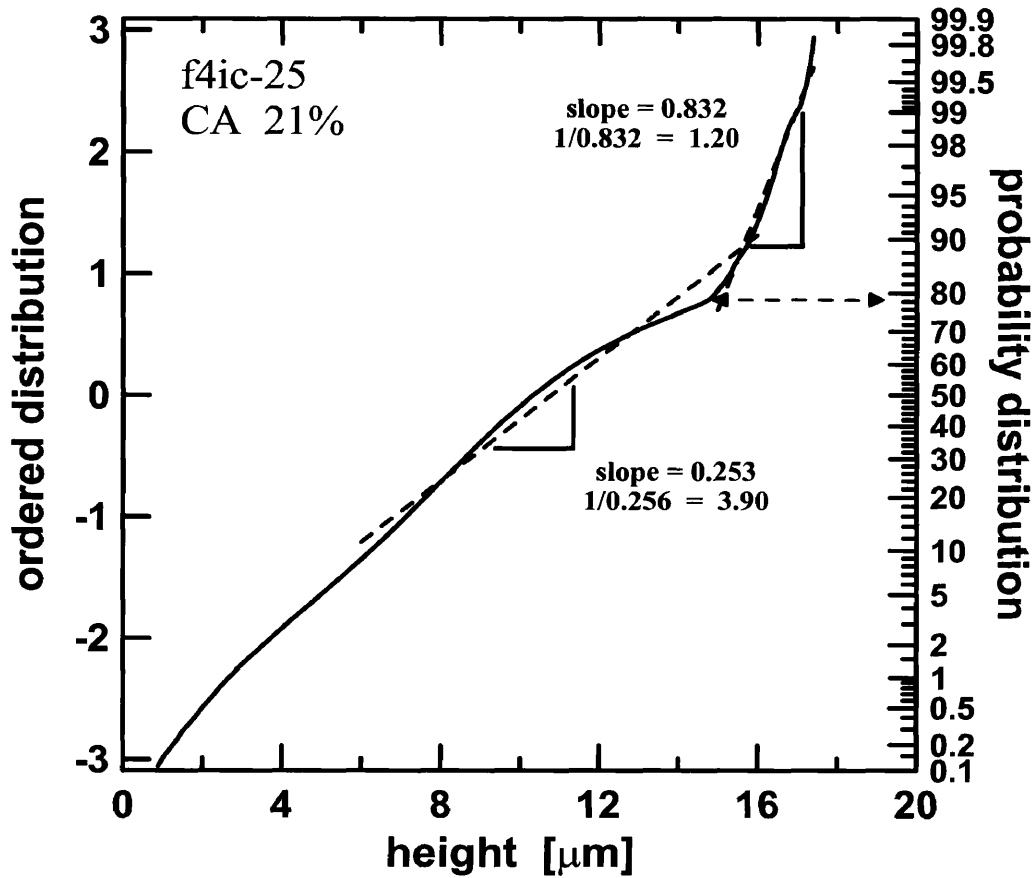


**Figure 3.18**     Probability plots of flat die tribometer sample I-99, tested at 8.08 MPa of normal stress.

It has been shown that there are different ways to measure the real contact area of the friction tests. In the specific example, observations of the bearing ratio curve and the probability curve show comparable results. This specific example was selected because it illustrates well the technique. For the rest of the samples there was more challenge in

identifying the change in slope in the bearing ratio curves, especially in the samples with very small fraction of real contact area, and in samples that were temper rolled, which have a larger fraction of real contact area. For this reason the analysis of the probability curves was selected as the methodology for measuring real contact area. Three 3D profiles per samples were analyzed and the real contact area reported is the average of the three measurements. To verify the accuracy of the technique, SEM-SE images of selected tested samples were taken and analyzed. The same technique used for measuring the distribution of phases on the surface was used for measuring the contact area. The flat regions on the surface were selected and marked on the image. The image was then digitally processed and the fraction of marked areas quantified. Figure 3.19 presents one example of real contact area quantification performed using SE-images. Three images per selected sample were taken, and the measure of real contact area is the average of the three.

## 3.3 Experimental Methods, Coating Mechanical Testing

The coating mechanical testing consists on friction and powdering tests, direct and indirect testing. The two main friction tests are the flat die tribometer and the bending under tension tribometer. An alternative friction test commonly used in hard coatings is the scratch test. The double-Olsen powdering test was used to measure quantify the adherence of the coatings to the substrate. And finally the limiting drawing ratio, a forming sheet type of test, gives an indirect measure of friction. In the following part of this section all those testing methodologies will be introduced and described.

### 3.3.1 Flat die tribometer

The flat die tribometer (FDT) is one of the simplest friction testing apparatus. The FDT consists of two flat dies that clamp on the testing strip sample, which is then pulled through the dies. Figure 3.20 presents a diagram of the FDT setup. This test was first developed by Wojtowicz in the 1950s [46]. Although the test is based on a very simple principle, it must be conducted with care. Alignment of the dies is important, the flatness of

the dies has to be controlled, as well as the entry radius of the dies because these factors affect the lubrication of the sample.



Threshold: 0-0

Count: 17

Total Area: 84529.000 pixel^2

Average Size: 4972.294 pixel^2

Area Fraction: 9.4%
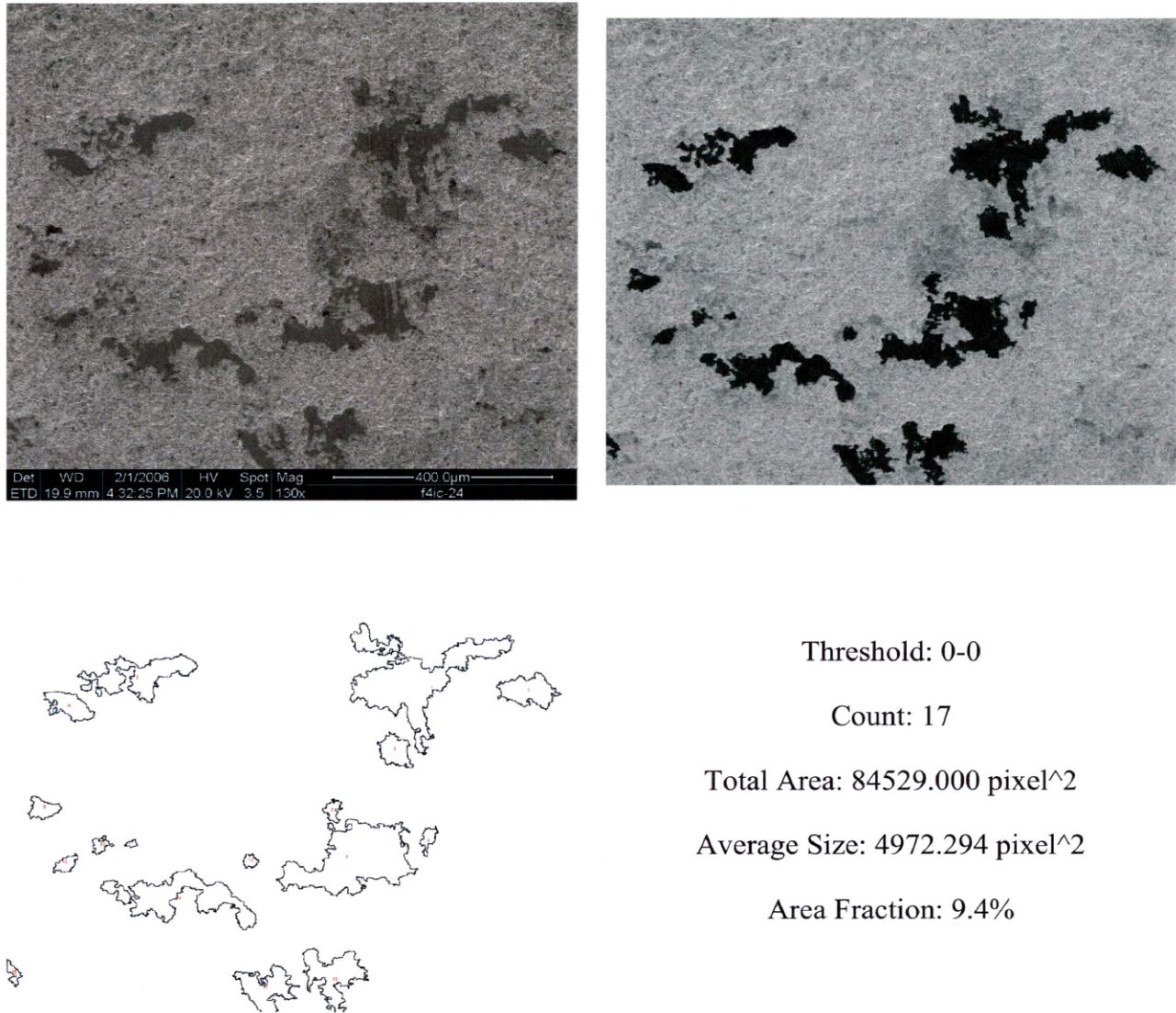
**Figure 3.19**      **Digital image processing analysis of real contact area of SEM-SE images. On the top left, the original SE-image is shown. On top right, the flat portions corresponding to the real contact area had been marked. On the bottom the results of the analysis is shown.**
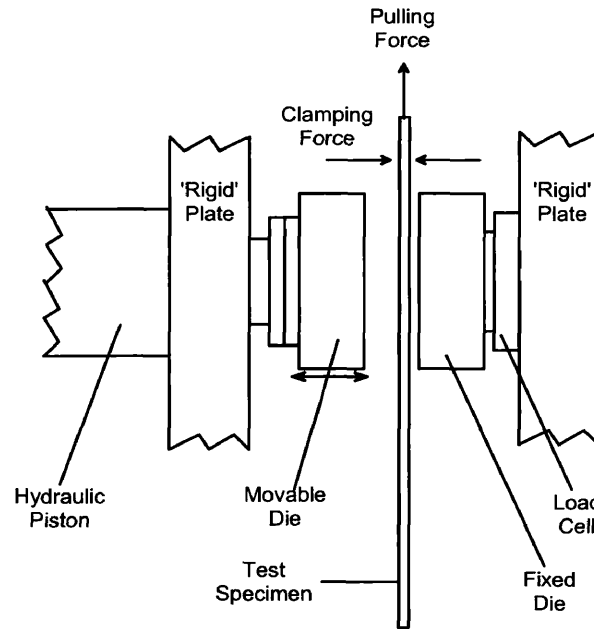
**Figure 3.20     Diagram of the flat die tribometer.**

The FDT consists of a frame attached to a 10-kip MTS frame with the actuator on the top.  The FDT frame provides support for the clamping dies and load-cell, while the MTS actuator pulls the samples.  In the FDT there are two load cells, one located at one of the clamping dies, which measures the clamping force; and the second is attached to the pulling grip and measures the pulling force.  The dies are two metal rectangles made of A2 tool steel with a roughness of $R_q = 0.06$ $\mu$m and a hardness of 60 HRC.  The clamping dies are designed with a self-guiding system to ensure they stay parallel to one another during the test.  The clamping force is imposed by a manual hydraulic pump; the cylinder that pushes the die is attached to a gas accumulator.  The gas accumulator provides pressure to compensate for any small variances of thickness in the testing sample that would result in variances of applied force.  Figure 3.21 presents a photograph of the FDT.
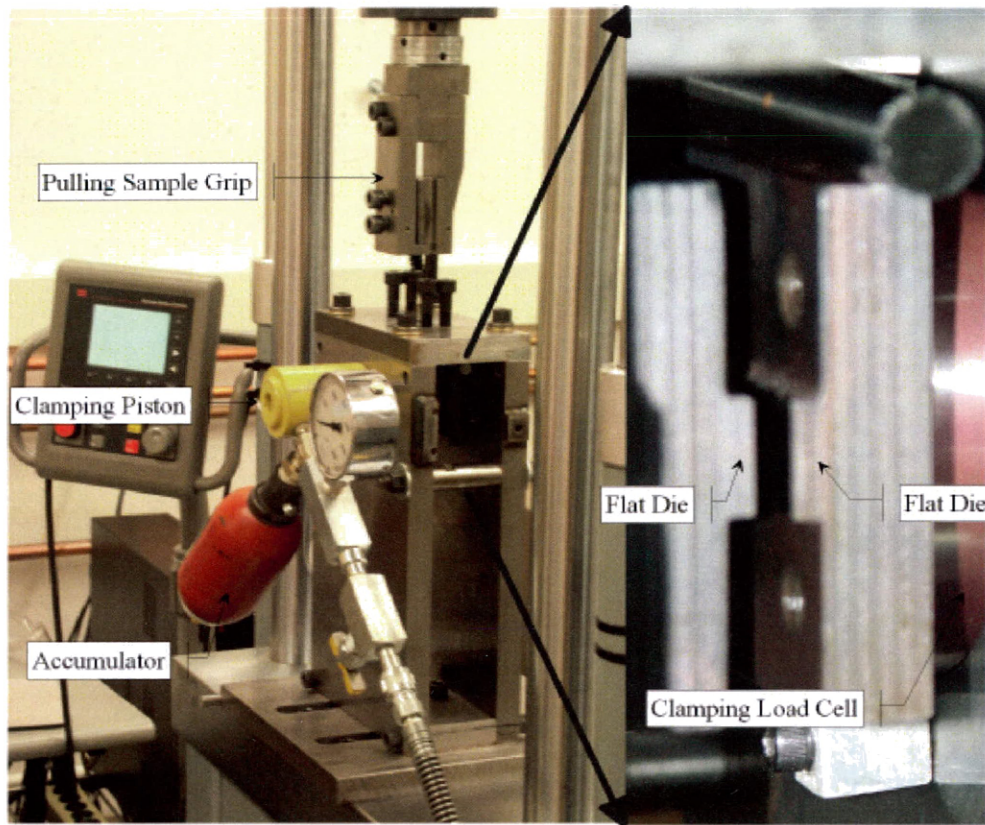
**Figure 3.21** **Photographs of the flat die tribometer set-up.**

The contact face of the dies is 12.7 x 63.5 mm (0.5 x 2.5 in); the samples could be up to 50.8 mm (2 in) wide and 500 mm long (about 20 in), and testing length is up to 150 mm, limited by the travel of the pulling actuator. The shearing of the samples leaves a sharp edge on the sides, before testing the sharp edge was filed off. The samples were then cleaned thoroughly with acetone to eliminate any debris and residual oils. Before testing, the samples were lubricated with Almag® (Texaco), a common stamping oil. The oil was applied with a brush to saturate the surface of the sample before testing.

Various test conditions were evaluated such as pulling velocities and clamping forces. The conditions under which the testing was conducted are as follows. Samples were pulled at a constant velocity of 25.4 mm/s (1 in/s) at three constant clamping force levels ~ 1800, 3600, and 5400 N. The limitation of the clamping force level was the resulting

pulling force limited by the coefficient of friction (COF), the yield strength and thickness of the sample. After testing, the samples were cleaned and sectioned for post testing observations. The contact surface of the dies was polished with a 6 μm diamond slurry every time a new coating was tested.

In the FDT friction test two forces are measured, the clamping force $F_c$, and the pulling force $F_p$. Normal stress component $\sigma_N$ and shear stress component $\tau$ can be calculated from these forces and the contact area, which is the width of the sample multiplied by the length of the die: $A_c$ = 645.16 mm$^2$ (50.8 x 12.7 mm).

[ Eq. ] 3-2 $$\sigma_N = \frac{F_c}{A_c}$$

[ Eq. ] 3-3 $$\tau = \frac{F_p}{2A_c}$$

where the shear stress component $\tau$ is divided by 2, because there are two areas of contact, one on each die. And the COF, $\mu$, is calculated as:

[ Eq. ] 3-4 $$\mu = \frac{\tau}{-\sigma_N}$$

[ Eq. ] 3-5 or, $$\mu = \frac{F_p/2A_c}{-F_c/A_c} = -\frac{F_p}{2F_c}$$

Since the normal stress component $\sigma_N$ is compressive its sign is negative, thus the reason for the negative sign present in [ Eq. ] 3-4, and followed in [ Eq. ] 3-5, in order to obtain a positive sign friction coefficient. Figure 3.22 presents an example of the measured forces and the calculation of the COF. It can be observed that the forces present small variation during the test. To calculate $\mu$, the average value of the forces is used, without including the noisy initial part of the test, which represents the boundary between the static and the dynamic friction measurement and a small stabilization period.
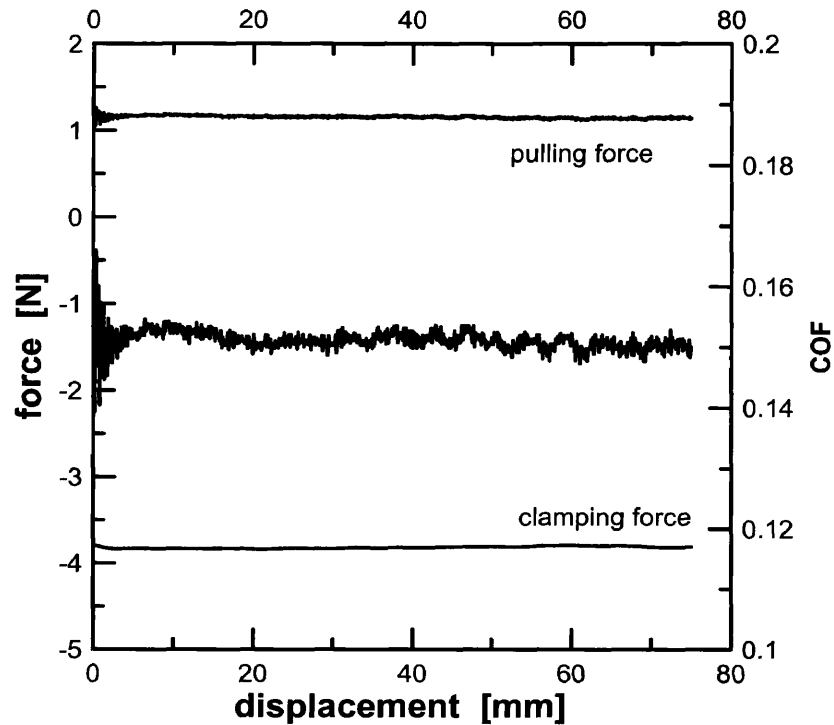
**Figure 3.22**      Data of a flat die tribometer test and coefficient of friction calculation.

## 3.3.2 Bending under tension tribometer

The bending under tension tribometer (BUTT) measures friction by bending a strip sample over a cylindrical roller die and pulling the strip at one end while keeping a back tension at the other end. Swift was the first to describe the mechanics of drawing of a sheet in contact with a circumferential pin, modifying the normal pulley equation balancing the forces involved and calculating friction[47]. In the book *Tribology in Metalworking* by Shey [48], Doege and Witthüser [49] are reported to have developed the bending under tension tribometer by modifying and adding free rollers to a previous draw bead simulator design by Littlewood and Wallace [50]. This testing technique was later studied by Vallance and Matlock. [51] and later explored by Coubrough [52], providing a more extensive understanding of the forces involved. Friction testing with the BUTT consists of a two-step process. First, the bending force is measured with the use of a free roller; this is the force

required to impart the bending deformations to the sheet and is dependent on the roller geometry, sample thickness, and strength. In the second step, the strip sample is pulled over a fixed roller from which the friction is measured. If it is assumed that the COF is independent of normal pressure the first step, the free roller testing can be eliminated according to Wenzloff *et al.* [53]. Figure 3.23 shows a diagram of the BUTT.
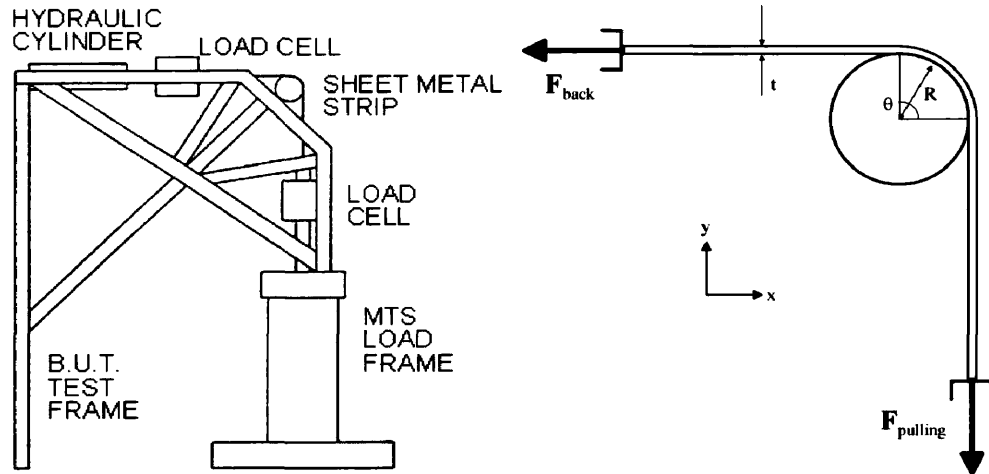


**Figure 3.23**     **Diagram of the bending under tension tribometer.**

The BUTT consists of a fixture addition that attaches to a 20-kip MTS frame. The additional frame supports an actuator that provides the back force, this actuator is controlled by an additional unit MTS 458, which controls only force. The regular MTS frame with the actuator at the bottom provides the pulling forces and is controlled by the usual Star Test software. The BUTT frame has the capability of exchanging fixed and free rollers of different diameters as well as being capable of performing bending tests at wrap angles of 45° and 90°. The load cells that measure the back and pulling forces are attached between the actuators and the sample grips and have a load limit of 44.5 kN (10,000 lb). The roller dies were manufactured from A2 tool steel, hardened to 60 HRC, with an average initial roughness of $R_q = 0.25$ μm (± 0.05 μm). The back actuator was controlled by a second control unit, MTS 458, capable of programming a ramping load. Figure 3.24 presents a photograph of the BUTT.
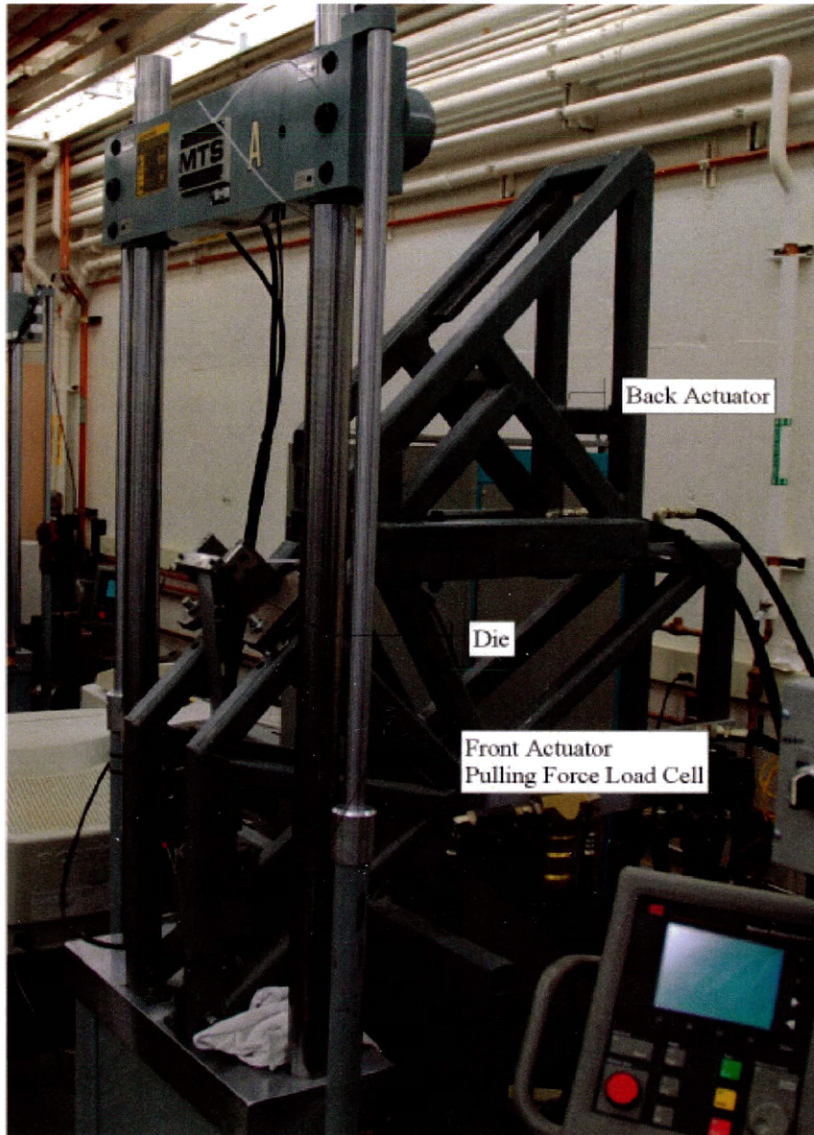
**Figure 3.24**     **Photograph of the bending under tension tribometer frame.**

The samples used in this study were 50.8 mm (2 in) wide and 533.4 mm long (21 in). The length of a test is limited to 150 mm by the travel of the actuators. The limiting factors in this test are the yield strength of the sheets and the thickness, which can bring the pulling and back force above the limit of the fixture, in which case samples of 25.4 mm width (1 in) should be use instead. The shearing of the samples leaves a sharp edge on the sides, before

testing the sharp edge was filed off. The samples were then cleaned thoroughly with acetone to eliminate any debris and residual oils. Before testing, the samples were lubricated with Almag® (Texaco), a common stamping oil. The oil was applied with a brush to saturate the surface of the sample.

All tests in the BUTT were performed at a sliding velocity of 25 mm/s (~1 in/s), and the length of the test was 150 mm (5 in). A back tension ramping force was used to measure the bending forces, programmed to increase from 0 to 9000 N at a rate of 1800 N/s, resulting in an applied ramping force of 2000 to 8000 N at a lower rate of 1500 N/s caused by the controlling unit changes. For friction measurement with the fix dies, the ramping back force was attempted, but the resulting COF showed significant variations that indicated dependence with normal pressure. The ramping force testing procedure of 2000 to 8000 N resulted in back and pulling forces that exceeded the yield strength of some samples. This caused some deformation in the sample prior to coming in contact with the die. Deformation of the samples prior to die contact alters the characteristics of the coating and invalidates the friction measurements. In addition to post-testing observations of the coating damage, it was important to determine the exact pressures applied at all surfaces of certain tests. For these reasons, the friction measurement was performed at constant back force at three levels: 0.4, 0.6, and 0.8 of the yield force of the sample.

For the friction testing two die diameters were used, 50.8 mm (2 in) and 12.7 mm (0.5 in). The 50.8 mm diameter die, the largest die diameter available, was selected because it represent a steady forming situation as well as resulting in a well behaved test. The 12.7 mm die, the smallest die diameter available, was selected because it represents a small radius of curvature, close to the radii in a deep drawing operation.

Before friction testing a sample, the die was conditioned by grinding it with a 600-grit SiC sanding paper by hand. The sand paper was wrapped over the die and held in place with one hand and, applying only the pressure of the closed hand and turning the die with the other hand (in the unfortunately case of being a single handed person, come up with a smarter way to proceed! or seek for professional help). After the die has been cleaned in order to simulate a working die, a sample is run at a medium load level (pulling load at about 0.5 the

yield strength of the sample) for a few passes (about 10), to create a steady pick up film on the die. It was found that the frictional force varied as the die was used, and after a few passes the forces became steady. The die conditioning was performed every time a different coating was tested.

The first step in measuring the COF of the BUTT involves measuring the bending force of the samples. As first indicated by Doege and Witthüser [49], the bending force is the difference between the pulling and back forces with a free roller die (frictionless) [ Eq. ] 3-6.

[ Eq. ] 3-6 $$F_{bending} = F_{pulling} - F_{back}$$

It was found by Coubrough [52] that the bending force decreases as the back force increases and is not constant as indicated by Wenzloff *et al.* [51]. A linear fit of the bending force as a function of the back force was calculated and used to determine the bending force. Figure 3.25 shows an example of the test data and the fitted line of the bending force.

The COFs were calculated using the equation proposed by Fox *et al.* [54] and Sulonen *et al.* [55], which will be referred to in this document as the modified Swift's equation. The procedure followed for the COF calculations was the procedure described by Vallance and Matlock [51].

Swift's equation

[ Eq. ] 3-7 $$\mu = \frac{1}{\theta} \ln\left( \frac{F_{pulling} - F_{bending}}{F_{back}} \right)$$

Modified Swift's equation

[ Eq. ] 3-8 $$\mu = \frac{1}{\theta} \left( \frac{r + 0.5t}{r} \right) \ln\left( \frac{F_{pulling} - F_{bending}}{F_{back}} \right)$$

where $\theta$ is the contact angle, which in this case is $\pi/2$, $r$ is the roller radius, and $t$ is the sheet thickness. Swift was the first to develop an expression that describes the COF in the bending under tension test, from integration of forces [47]; the resulting expression is similar. There are different equations that calculate COF from the BUTT test that were developed after Swift. The COF calculated with Swift's equation with the 50.8 mm diameter die are not too

different from the others, while the COF calculated with the 12.7 mm diameter die fall in the middle of the other values [52]. It has been indicated by Coubrough that any calculation of the COF using the Swift equation [ Eq. ] 3-7 or the modified Swift equation [ Eq. ] 3-8, in which its constant makes the COF even a little higher, are an overestimation especially at low angles of wrap and small die radii.

Figure 3.26 (a) presents an example of the data collected from a friction test, using the 50.8 mm diameter die. From these data, the forces are averaged between the displacements that represent the steady part of the test (between the displacements of 40 to 100 mm). For each coating, the various pairs of forces for the three different back force levels are plotted together as an adjusted force (which is the back force minus the bending force) versus the pulling force, normalized by the yielding force. A linear curve through origin was fitted to the data points, and the slope is used to calculate the COF. Figure 3.26 (b) presents an example of the calculation. Triple tests were conducted per coating, and back force level to assure some statistical significance.

(a)



Equation Y = -0.02119 * X + 408.26
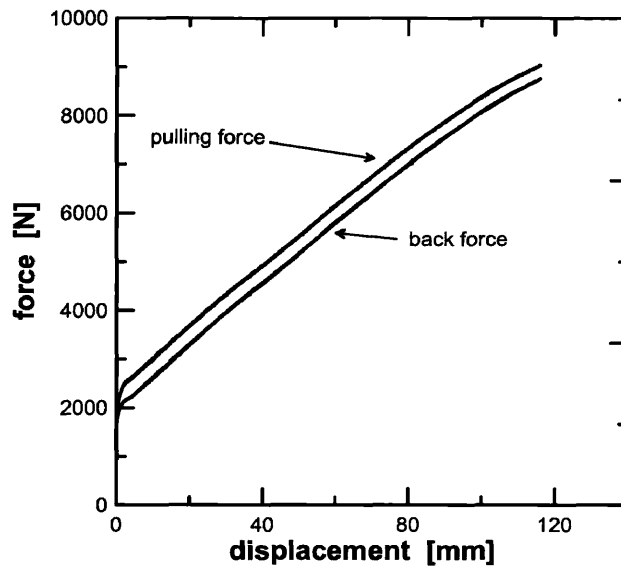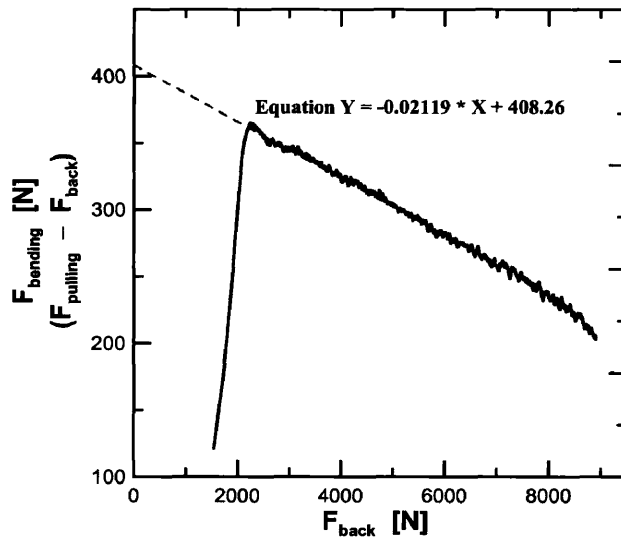
(b)

Figure 3.25     Bending under tension tribometer free roller testing for bending force calculation.
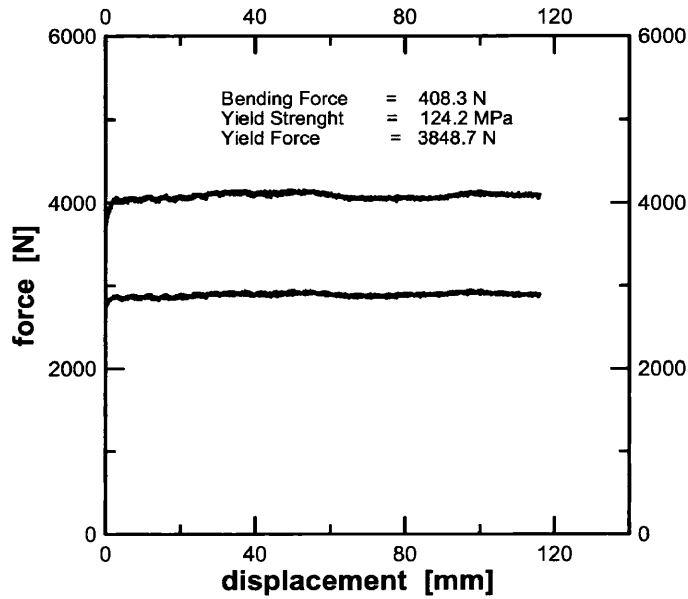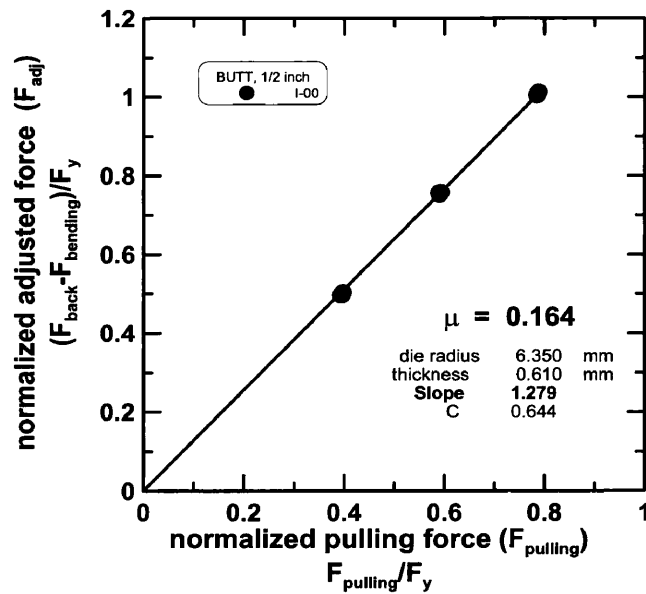
Figure 3.26     Bending under tension tribometer, friction testing example. (a) Shows the pulling force and the back force are plotted versus displacement of the test. (b) Presents an example of the coefficient of friction calculation is presented, where six different test are plotted for the three back force levels.

The COFs are calculated from the plots as follows:

[ Eq. ] 3-9 $\qquad F_{adj} = F_{back} - F_{bending}$

[ Eq. ] 3-10 $\qquad C = \dfrac{2}{\pi}\left(\dfrac{r + 0.5t}{r}\right)$

The slope of the curve of adjusted back force versus pulling force represents:

[ Eq. ] 3-11 $\qquad slope = e^{\mu/C}$

From which the COF can be calculated as:

[ Eq. ] 3-12 $\qquad \mu = C\ln(slope) \ \text{ or } \ \mu = \dfrac{2}{\pi}\left(\dfrac{r + 0.5t}{r}\right)\ln\left(\dfrac{F_{adj}}{F_{pulling}}\right)$

A modified BUTT COF calculation method was developed by Coubrough [52]. In his calculation method, he separated the analysis of the shear stress and the normal stress. For the normal stress, a vector analysis results in a prediction of the angle of conformity. The angle of conformity is often lower than the nominal testing angle and it is dependent on the applied back force. His equations are:

[ Eq. ] 3-13 $\qquad R = \sqrt{F_{back}^{2} + F_{pulling}^{2}}$

[ Eq. ] 3-14 $\qquad \beta = \tan^{-1}\left(\dfrac{F_{back}}{F_{pulling}}\right)$

[ Eq. ] 3-15 $\qquad \alpha = 2\left[\beta - \left(\pi/2 - \theta\right)\right]$

where $R$ is the resultant force experience by the roller die, $\alpha$ is the angle of conformity, and $\theta$ is the bending angle, which is $\pi/2$ for 90° wrap angle. Significant difference in the methods is the cord length of contact which is assume to be the full extent of $\pi/2$ for the modified Swift's equation [ Eq. ] 3-8. Coubrough, instead of calculating the contact cord length from the angle of conformity, he gave a justification to assume it perpendicular to the line of action of R.

**[ Eq. ] 3-16**  $\qquad C = 2r\sin\left(\alpha/2\right)$

where $r$ is the roller die radius.

The average normal stress is then calculated from the resultant force divided by the area which is the product of the contact cord length multiplied by the width of the sample, $w$:

**[ Eq. ] 3-17**  $\qquad \sigma_N = \dfrac{R}{C * w}$  or  $\sigma_N = \dfrac{\sqrt{F_{back}^2 + F_{pulling}^2}}{2rw\sin\left(\alpha/2\right)}$

A simple force balance is used to calculate the shear force:

**[ Eq. ] 3-18**  $\qquad F_{shear} = F_{pulling} - F_{back} - F_{bending}$

And the shear stress is calculated from using this force divided by the area calculated with the angle of conformity, $s = 2r\alpha$:

**[ Eq. ] 3-19**  $\qquad \tau = \dfrac{F_{shear}}{2r\alpha w}$

The COF is calculated as the shear stress divided by the normal stress. The expression for the COF is as follows:

**[ Eq. ] 3-20**  $\qquad \mu = \dfrac{\tau}{\sigma_N}, \quad \mu = \dfrac{2F_{shear}}{R\alpha}\sin\left(\alpha/2\right)$, or

$$\mu = \dfrac{2\left(F_{pulling} - F_{back} - F_{bending}\right)}{\alpha\sqrt{F_{back}^2 + F_{pulling}^2}}\sin\left(\alpha/2\right)$$

### 3.3.3 Scratch tribometer

The scratch test is most commonly used for testing the breakdown of hard coatings, and it is commonly used in the thin films industry. The equipment used for this test was the Teer Coatings ST-2200 Scratch Tester. It consists of an indenter with interchangeable tips, from different sizes of TiC or Cr-steel spheres and diamond tips that move downward and touch the sample which is placed on a moving table.

The normal load applied can be program to a constant or to a ramping increasing load. The speed of the table as well as the direction is also programmable. Figure 3.27 presents a schematic of the scratch tester.
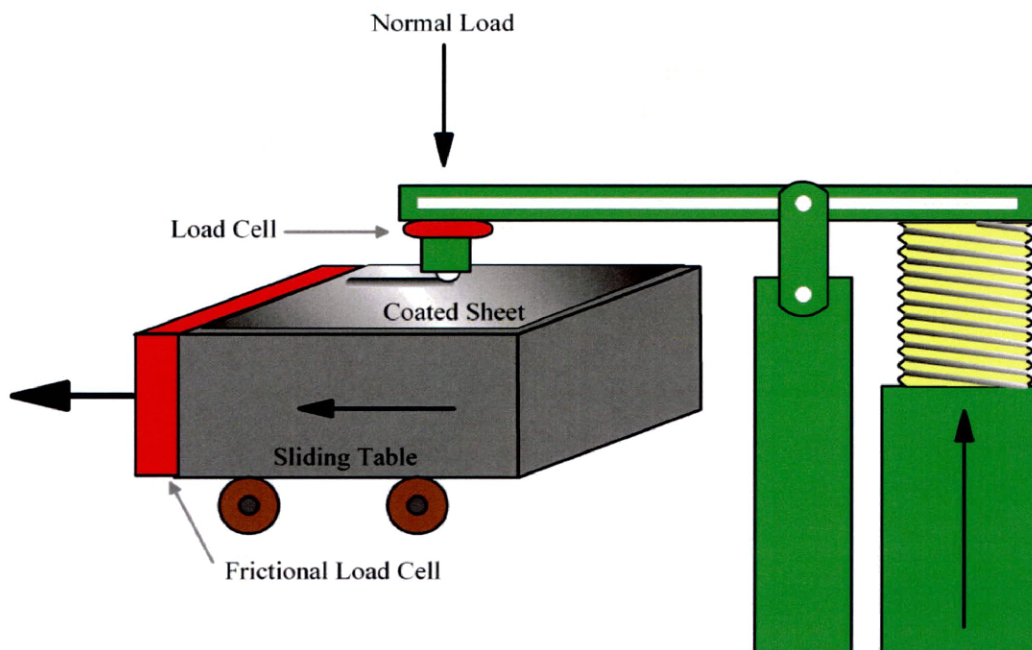


**Figure 3.27      Diagram of the scratch tester.**

The scratch tester uses a very simple loading program. A moment arm arrangement imparts the normal loading. The loading is transferred by a screw driving mechanism attached with a spring that avoids overload situation. The loading rates are programmed to match a speed of the screw movement, meaning that it is a fixed rate instead of a controlled rate from a feed-back system. The contact tips are interchangeable, with options of diamond and sphere tips. For the testing in this study a 3.97 mm (5/32 in) Cr-steel bearing ball was used for every test, with a fresh contact surface for each coating.

The samples were sheared to blanks of 25 x 50 mm (1 x 2 in) to fit the testing table. The samples were cleaned with acetone to remove any debris and oil. The samples were mounted into a metal holder glued with wax.

Two testing conditions were explored, lubricated and non-lubricated. The table speed was 20 mm/min for all the tests. The normal load was setup at a quasi-static rate of 5 N/min at three different levels of approximately 16, 32, 46 N. The need to run a quasi-static test instead of a constant normal load test came about due to the programmability of the testing instrument to record loads while testing. A constant normal load test would not have given the option of recording normal load while testing, losing loading information created by variances of the surface topography. Figure 3.28 presents an example of the data collected in a scratch test.
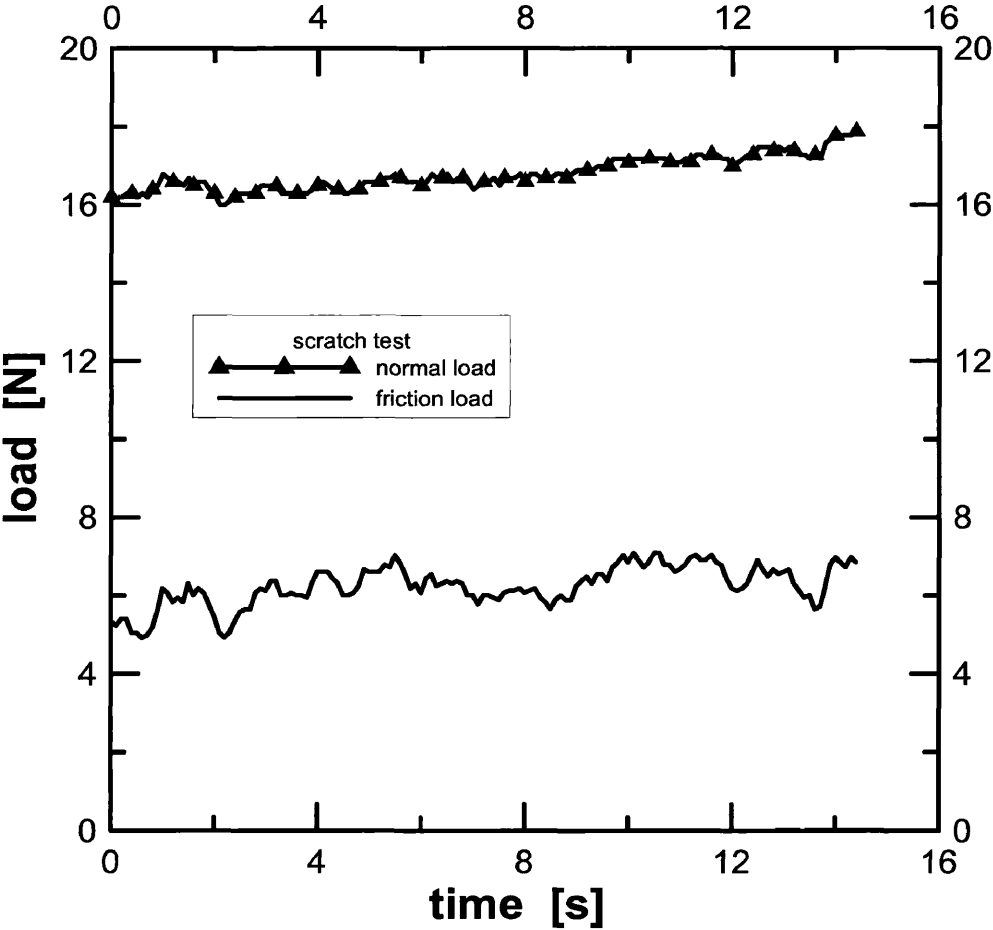


**Figure 3.28**       Scratch test example, sample I-02 tested at a normal load of 16 N.

The COF were simply calculated using the ratio of the forces, assuming that the areas of contact are the same.

[ Eq. ] 3-21
$$\mu = \frac{F_{frictional}}{F_{normal}}$$

Although the loads applied in this test were low compared to a macroscopic test set up, the contact areas were small and result in very high stresses components, often above the yield point of the samples. This characteristic makes this test fundamentally very different from the other friction tests.

### 3.3.4  Double – Olsen powdering test

The double-Olsen powdering test is widely used in industry to evaluate adhesion of coatings. It consists of a reversed dome upsetting of a blank that imparts a bidirectional bending deformation; the initial bending produces compressive stresses followed by unbending. The effects of the bending and unbending deformation cause weak adhesion of the substrate coating to fail [56]. Figure 3.29 shows a schematic of the double-Olsen powdering test. The testing was performed at ISG Research Homer Labs in Bethlehem, PA.
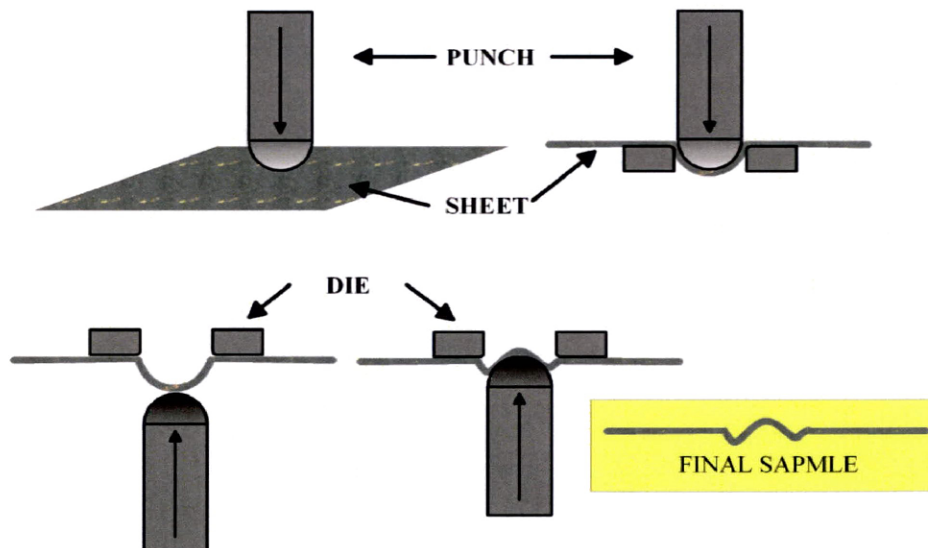
**Figure 3.29**      **Diagram of the double-Olsen powdering test.**

The Olsen test apparatus is comprised of a blank holder and a spherical punch. In the double-Olsen test (or also called reversed-Olsen test) the blank is deformed by the spherical punch with the clamping dies securing the blank to prevent any level of drawing of the blank. Once the dome is formed, the blank is turned upside down and another dome is punched in the reverse direction. The diameter of the punch sphere is 22.2 mm (0.875 in), and it is made of hardened tool steel and precision ground. The axially aligned clamping dies have a 25.4 mm (1.000 in) diameter hole with a 0.65 mm (0.25 in) profile radius. The nominal clamp pressure of the dies is about 1.21 MPa (175 psi) or enough to prevent drawing of the blank. The samples used for this test are square blanks of 57 mm x 57 mm (2.25 x 2.25 in). The specifications for the double-Olsen test are the one specified by Daimler-Chrysler Corporation laboratory procedures MS-6000 and MS-8056 [57]. Figure 3.30 shows the forming evolution of a blank.
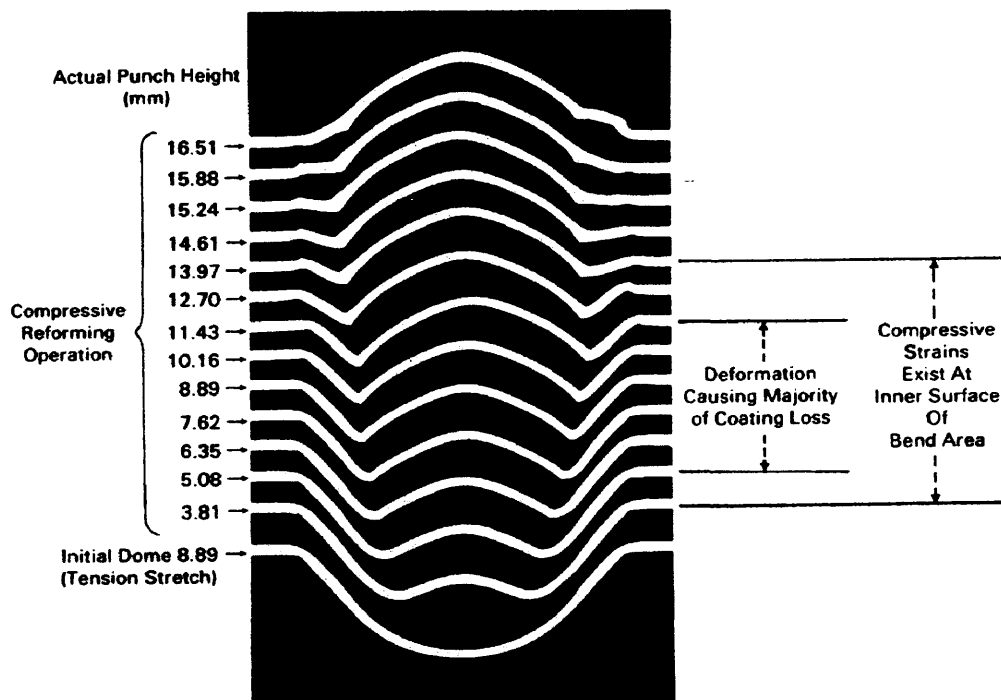


**Figure 3.30**        **Incremental forming evolution of the double-Olsen dome 56**

71

The punch speed is kept between 3.4 to 4.2 mm/s (8-10.0 in/min) for the entire test. The first cup is drawn to a height of 8.9 mm (0.350 in) with the surface of interest facing the punch. The blank is released and turned around and secured. The second cup is drawn up to a height of 6.3 mm (0.250 in) from the original zero [57].

The samples are carefully degreased with acetone before being weighed in a precision balance, to record the initial weight. A light film of rust preventative oil is applied on both sides of the sample as a lubricant. After testing, the sample is degreased in acetone, and the excess coating debris is cleaned with a brush. The coating is then pulled with a *3M Scotch Brand "898"* tape, or similar, several times; this pulls any coating particles that came loose of the substrate. Then the sample is cleaned again in acetone to remove any remaining tape. The sample is weighed again in the precision balance to register the final weight. Figure 3.31 presents an example of a double-Olsen test sample.
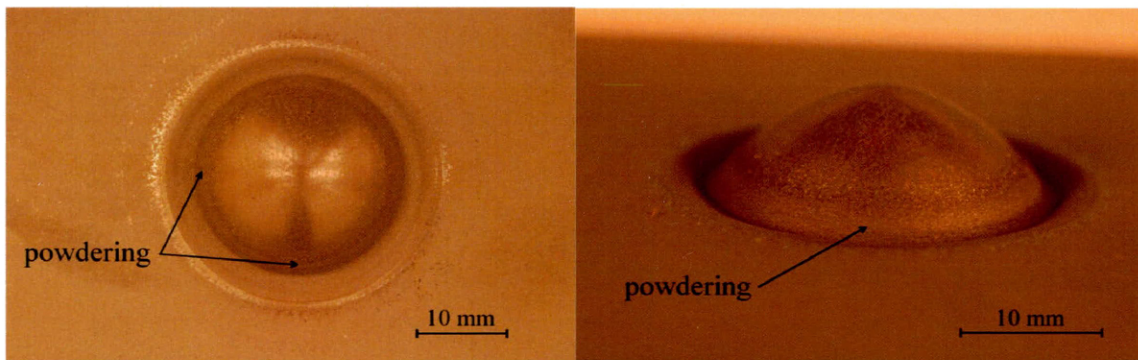


**Figure 3.31** **Example of one of the double-Olsen test samples. Notice the rim in the lower part of the dome where the coating is lost.**

The coating loss is calculated from the difference between the initial weight of the blank and the weight of the blank after testing.

[ **Eq.** ] **3-22**    coating mass loss $= M_i - M_f$

where $M_i$ is the initial mass and $M_f$ is the final mass.

Pure visual inspection is another way to evaluate the coating adhesion performance. After testing, the samples are cleaned, and the excess coating is pulled with the tape as

described above, but then the sample are compared to a table of previously tested samples and are ranked based on their appearance. Although a quicker way to evaluate the coating, this method is not as precise as the coating mass loss.

## 3.3.5 Limiting draw ratio

To measure the limiting draw ratio (LDR) of a material the Swift cup test is used. The Swift test is a cup drawing test, where different circular blank diameters are drawn with cylindrical punch [58]. The ratio of the blank diameter and the punch diameter gives the LDR. Figure 3.32 shows a typical Swift cup test configuration.
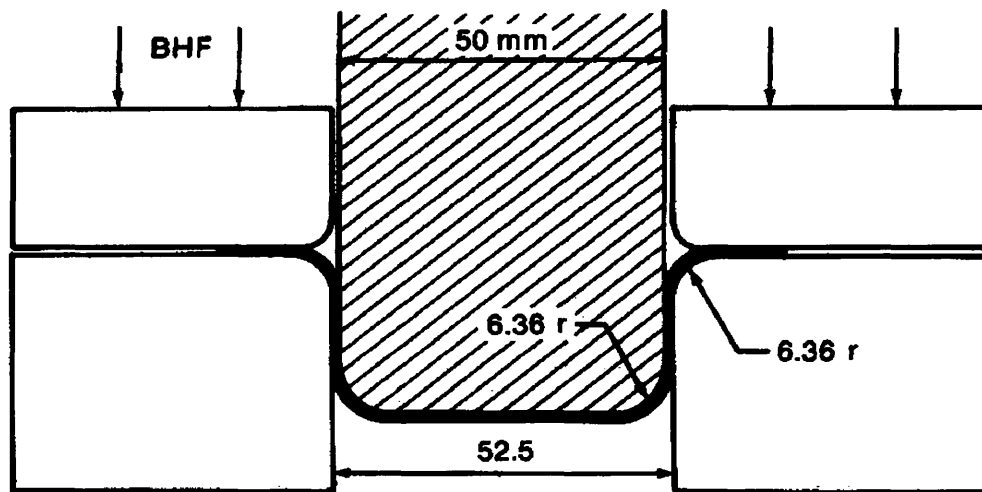


**Standard dimensions for the Swift cup test.**

**Figure 3.32      Typical Swift cup test configuration.58**

The punch of the Swift testing apparatus is 50.8 mm (2.00 in) in diameter. The die set is 54.5 mm (2.144 in) in diameter. The die and punch profile have a radius profile of 6.35 mm (0.250 in). The testing was performed at ISG Research Homer Labs in Bethlehem, PA.

The LDR Swift cup test is a trial and error process where several blank diameters are tested until the limit is found. Although several attempts have been made to instrument the LDR Swift cup test, most materials fall into a LDR value of 2.0, providing a good starting

point. The blanks are punched to the different diameters from 101.6 mm to 114.3 mm in increments of 1.27 mm (which represents diameters from 4 to 4.5 in, in increments of 0.05 in), cleaned thoroughly, and well lubricated before the testing.

There are a few testing variables that need to be addressed, but overall it is a very well defined test. There is an empirical expression to calculate the blank-holder force (BHF), and the force should be enough to prevent the sheet from wrinkling before drawing.

[ Eq. ] 3-23 $$BHF = \frac{\pi}{4}\left(D^2 - d^2\right)\frac{\sigma_y + \sigma_u}{200}$$

where $D$ is the blank diameter, $d$ is the cup punch diameter, and $\sigma_y$ and $\sigma_u$ are the yield and ultimate strengths of the material. Since the operation of the test was done manually by an experience operator, there was no measure of the exact rate at which the blanks were drawn, but a rate of 0.423 mm/s (1 in/min) is an adequate estimation.

The LDR is defined as the maximum blank diameter $D_{max}$ that can be successfully drawn in to a cup of diameter $d$.

[ Eq. ] 3-24 $$LDR = \frac{D_{max}}{d}$$

Two blanks of each diameter were drawn. A common practice in industry is to define the maximum blank diameter when the two blanks are successfully drawn. In this study, the maximum blank diameter was taken as the average of the two successfully drawn blanks, for example, if two blanks were successfully drawn with a diameter of 109.22 mm and only one of two with a diameter of 110.4 mm, the maximum blank diameter will be taken as (109.22 + 110.43)/2 = 109.885 mm, the average between the two diameters.

# CHAPTER 4

# RESULTS

This chapter presents all results of the experimental testing and characterization completed for the dissertation. Experimental methods are described in Chapter 3. The discussions presented in the Chapters 5 and 6, and the conclusions given in Chapter 7 are based entirely on the results presented in this chapter. This chapter is organized into three sections: the first section presents the results of the coating characterization of the galvannealed (GA) steel sheets; the second presents the results of the mechanical testing performed on the coated sheets; and the last presents the results of the characterization of the tested samples, a crucial part of the conclusions formulated in this dissertation.

## 4.1 Coating Characterization

The distribution of intermetallics in the GA coating is known to affect the frictional and powdering response. The materials description includes a chemical analysis of the experimental coatings. This chemical analysis accurately describes the amount of Fe in the coating and provides an overview of the intermetallic phases present in the coating, but does not specify which phases are present or their exact distribution. The coating characterization makes it possible to measure the intermetallic phase distribution at the surface of the coating and to understand the effect of the phases on friction and powdering.

### 4.1.1 Metallography and chemical analysis

The metallographic observations are presented in Chapter 3 along with the experimental materials. The observations of the cross-section samples present a good example of the morphology of the phase on the surface, and together with the observations of the scanning electron microscope images (SEM) of the surface, phase identification is

possible. The chemical analysis is also presented in the coatings descriptions in the Chapter 3. Coating mass and weight percent of Fe in the coating are also listed in Table 3.5.

## 4.1.2 Glow discharge quantitative profiling

The ISG samples designated as I-00, I-04, I-92, I-99; USS samples designated as U-02T, U-93T, U-99T; as well as the AK samples designated as A-15T and A-85T, were analyzed by glow discharge quantitative depth profiling (GD-QDP). A series of elements were profiled in each test such as Al, B, C, Cr, Cu, Fe, Mn, Mo, N, Nb, Ni, O, P, S, Si, Ti, V, and Zn. Not all the elements are important for the coating characterization. The key elements used to characterize the coatings are Fe and Zn, and in some cases Al and C content are also important. Figure 4.1 shows an example of an element profile. Nevertheless, observing the concentration of the other elements, as shown in Figure 4.2, provides a good idea of the thickness of the coating, such as Ti and Mn, which indicates where the substrate starts. It is also important to note the oxygen profile, as evidence of the presence of oxide products at the surface such as ZnO and AlO.

The intermetallic phase distribution is evident when the Zn profile is plotted for several samples. Figure 4.3, Figure 4.4, and Figure 4.5 present the Zn depth profile for all the sheets. The solubility of Zn in the δ-phase is indicated by the shaded box. If the profile curve falls into the shaded area the phase present at that depth is the δ-phase, while if the profile curve stands above the shaded area the phase is either a combination of ζ+δ or pure ζ-phase. As shown in the figures, at distances close to the surface, the profiles of I-00 and I-04 are clearly below the profiles of I-92 and I-99, indicating the difference between coatings with ζ-phase and the coating without it. It can also be observed that the profiles of the sample I-04 contains more Zn near the surface than the sample I-00, which could indicate the presence of a minimal ζ-phase at the surface, since the ζ-phase contains more Zn. For this characterization technique, the information at the surface and 0.25 μm below is not accurate.
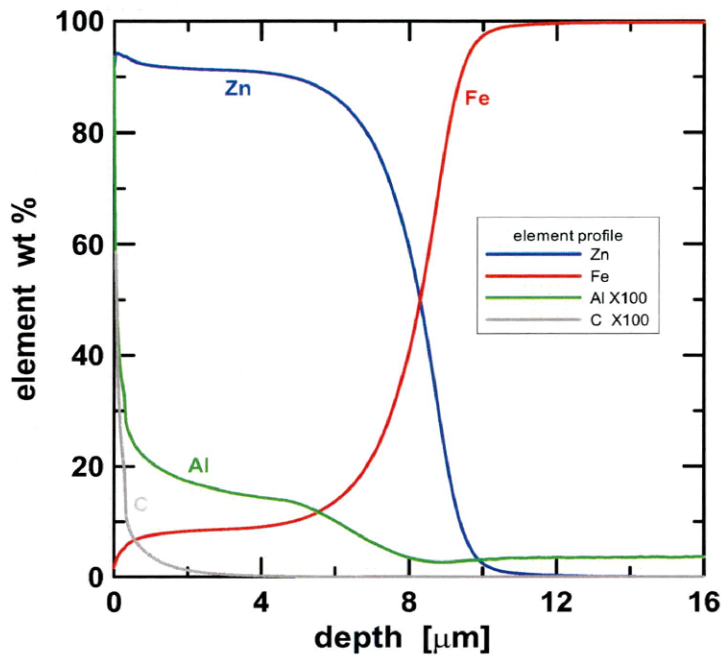
**Figure 4.1**      Glow discharge quantitative depth profiling for sample I-04. This figure shows the weight percent for only Al, C, Fe, and Zn, where the Al and C are scale 1:100 to appear in the curve.
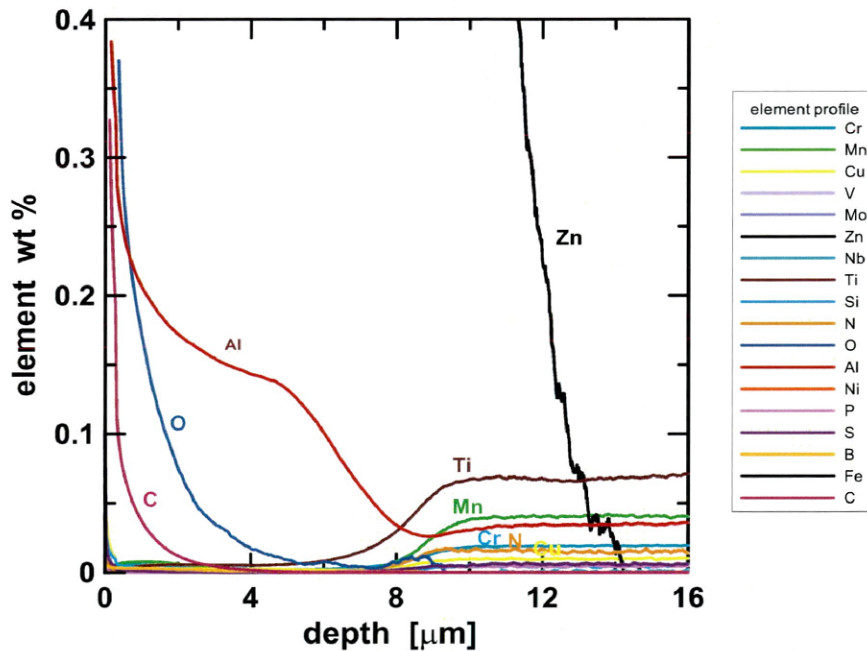


**Figure 4.2**      Glow discharge quantitative depth profiling for sample I-04. This figure presents all the elements profiled at a lower percent scale.
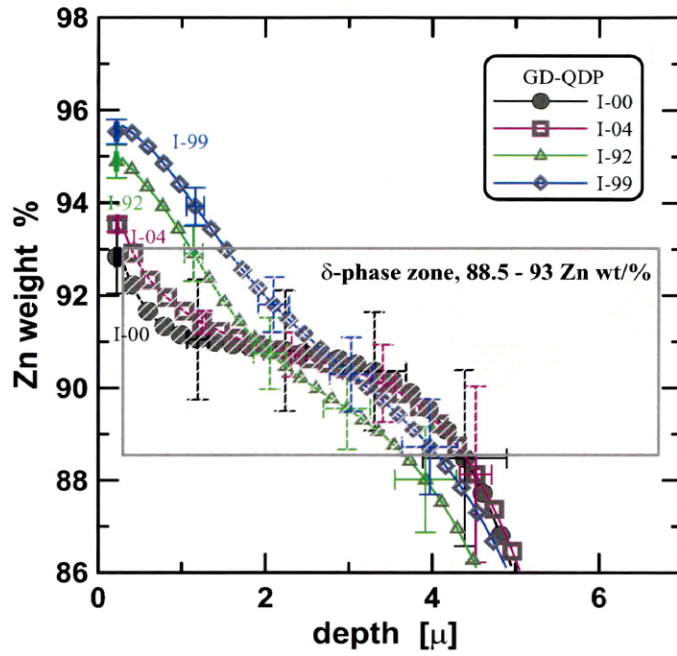
**Figure 4.3**  **Zn profile for ISG sheets, I-00, I-04, I-92, and I-99.**
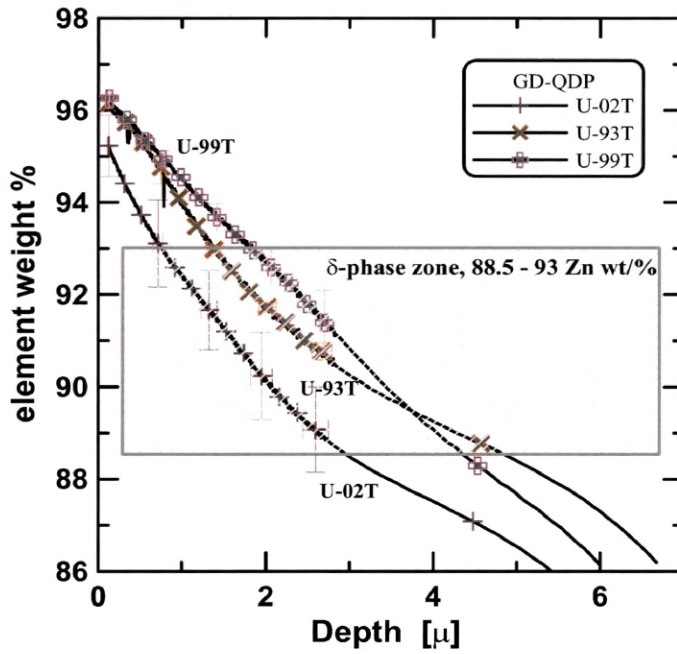


**Figure 4.4**  **Zn profile for USS sheets, U-02T, U-93T, and U-99T.**
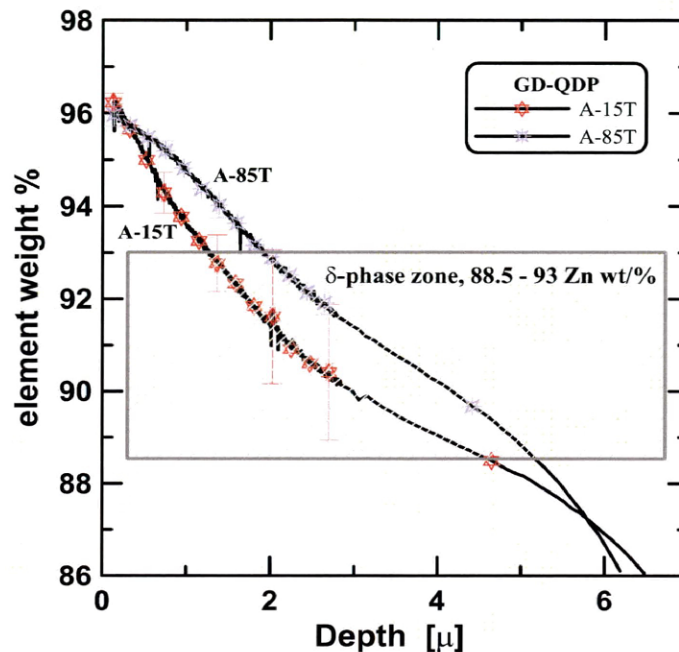
**Figure 4.5**        **Zn profile for AK sheets A-15T and A-85T.**

## 4.1.3 X-ray diffraction

X-ray diffraction patterns were obtained from the ISG, USS and AK coatings, Figure 4.6 Figure 4.7, Figure 4.8, Figure 4.9, and Figure 4.10 present the patterns obtained. Peaks corresponding to the ζ-phase are present for samples I-92 and I-99, an expected result because the LOM and SEM cross-sections along with SEM observations of the surfaces clearly indicate the ζ-phase is present in the surface. For sample I-04, which in cross-section observations reveal no presence of the ζ-phase (Figure 3.2) although SEM observations of the surface indicate the presence of the ζ-phase (Figure 3.5), the x-ray diffraction patterns do not show a clear peak corresponding to the ζ-phase (Figure 4.6). Nevertheless, at 63.5°, the highest ζ-phase peak, there is indication of a small dimple, sign of the presence of the crystal structure at the surface but in a quantity so minimal that the intensity of the peak is almost nonexistent, Figure 4.6. In the other figures, the ζ-phase peaks at 63.5° are identified with arrows. The automatic phase identification of the analysis software did not identified the ζ-

phase in sample A-15T shown in Figure 4.9, however the large $\zeta$-phase peak is noticed in the figure. From LOM and SEM-SE images of the surface, the presence of the phase is known.

The thickness of the coating and the scale of the phases in the coating, sometimes representing a fraction of a micron thick, can make normal x-ray diffraction a complicated characterization technique. Quantification of the phases of the coating makes for a particularly challenging experiment. Special diffraction techniques such as low angle of incidence could give better results, for a quantitative analysis. Nonetheless, x-ray diffraction analysis should be supported by other types of analyses such as cross-section observations and chemical analysis, in order to make a definitive statement about the quantity of phases present at the surface of the coating.

## 4.1.4 Intermetallic phase distributions

The intermetallic phase distribution of the surface was quantified by observation of SEM images of the surface of each coating. With the knowledge of the morphology difference between the $\delta$-phase and the $\zeta$-phase such as size and shape (where the $\zeta$-phase always appears to have a larger size and rectangular shape compared to the smaller size and cubic shape of the $\delta$-phase) and the knowledge of the phase evolutions during the annealing process discussed in Chapter 3, the $\zeta$-phase was identified and quantified. It is believed that the distribution of the $\zeta$-phase at the surface has a significant effect on the contact area between the sheet and a die in the forming process. Table 4.1 presents the distributions of the phases present on the surface of the coatings.
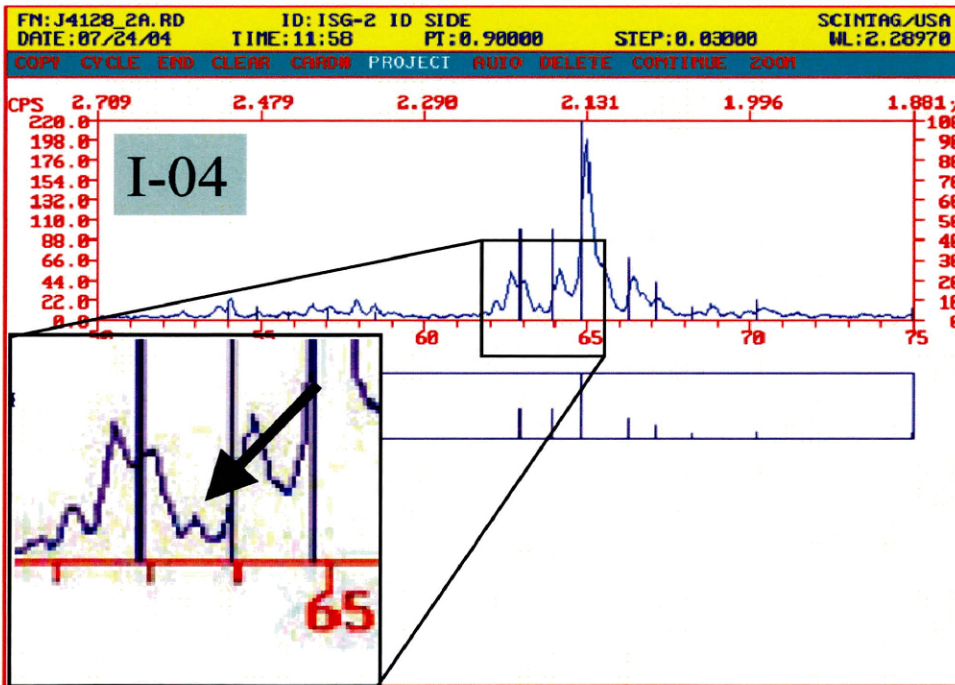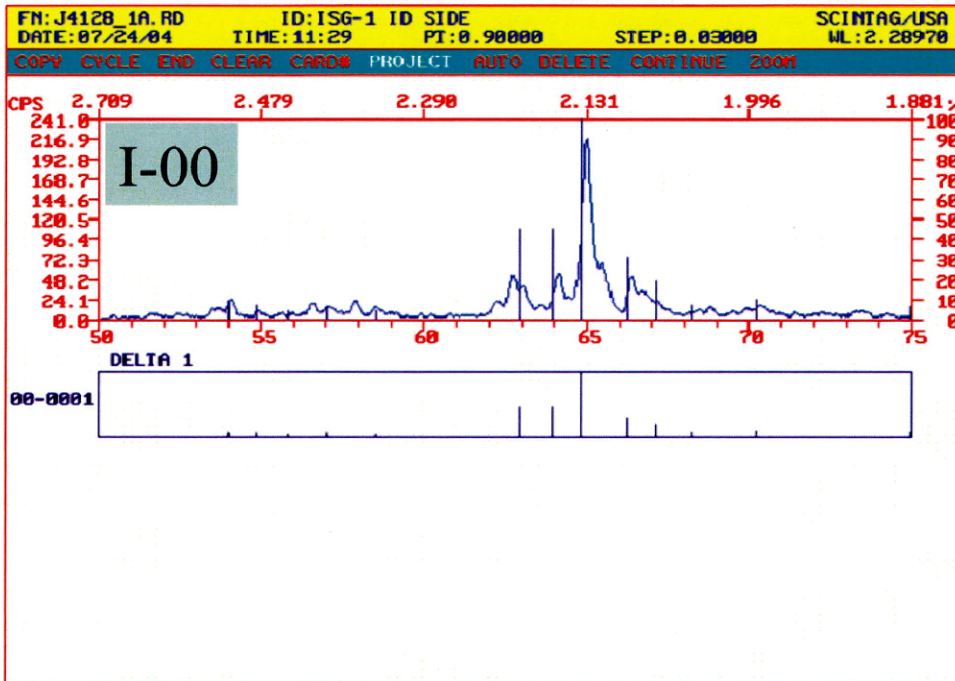
**Figure 4.6**      **X-ray diffraction patterns of samples I-00 and I-04.**
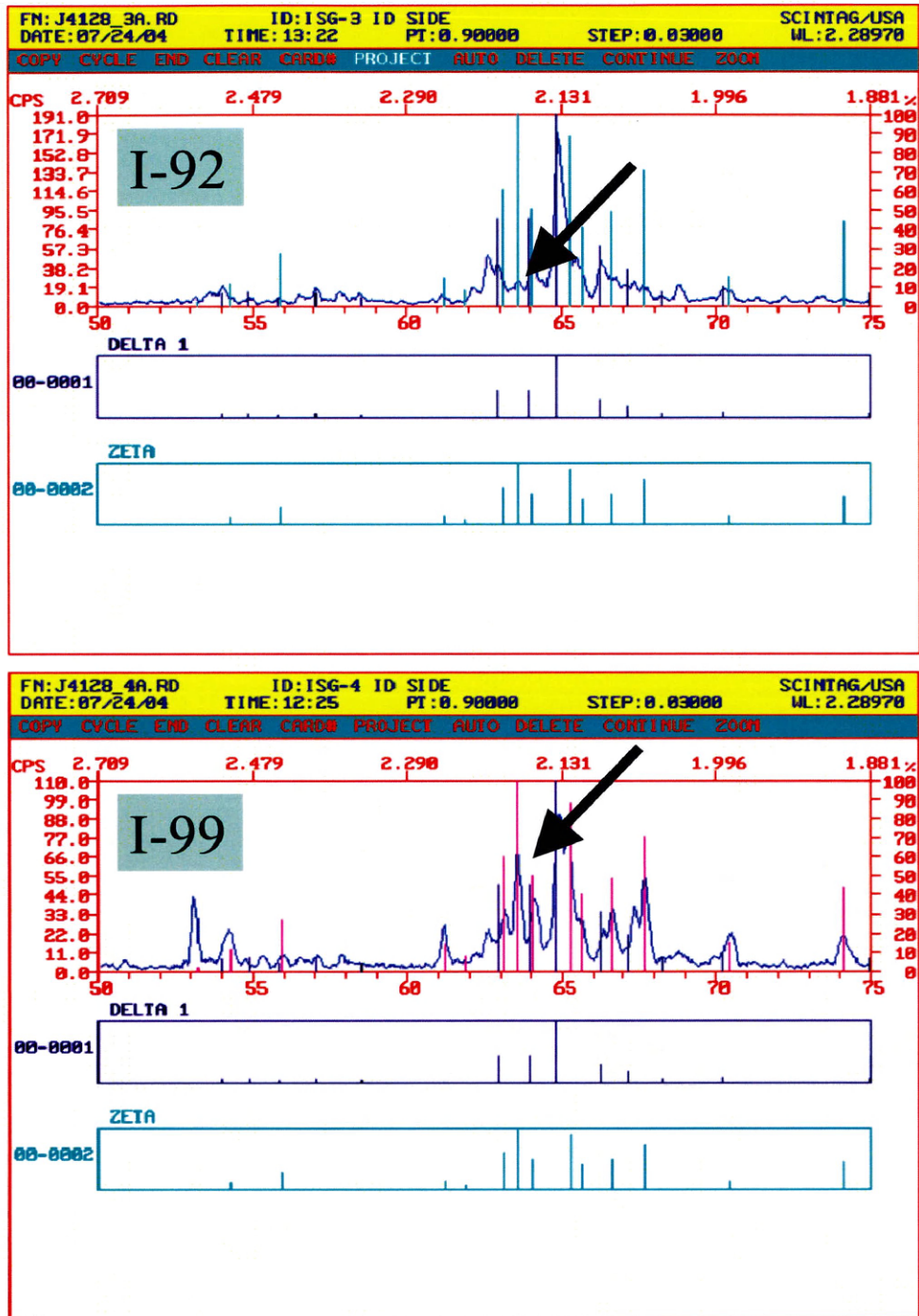
Figure 4.7    X-ray diffraction patterns of samples I-92 and I-99.
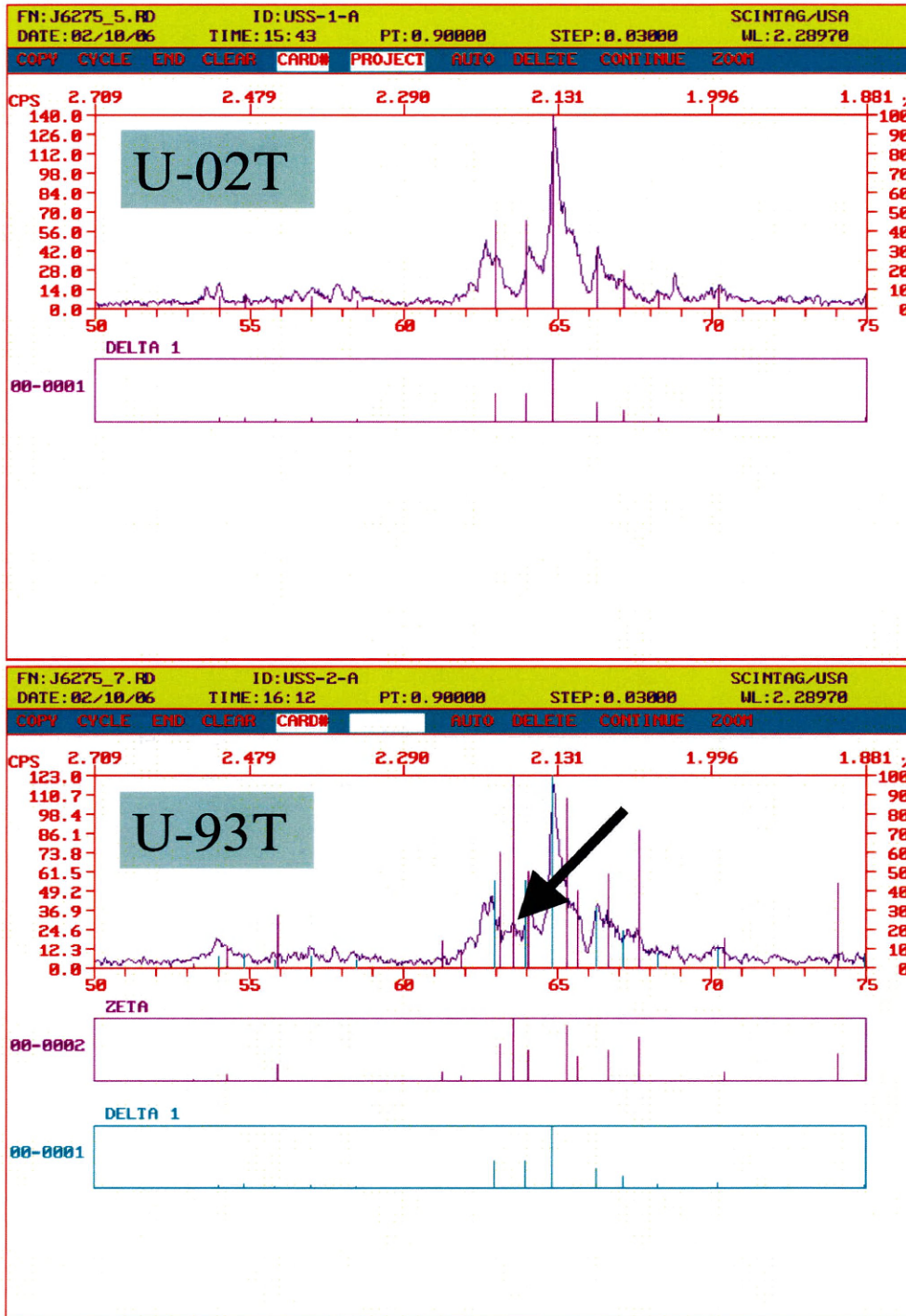
**Figure 4.8        X-ray diffraction patterns of samples U-02T and U-93T.**
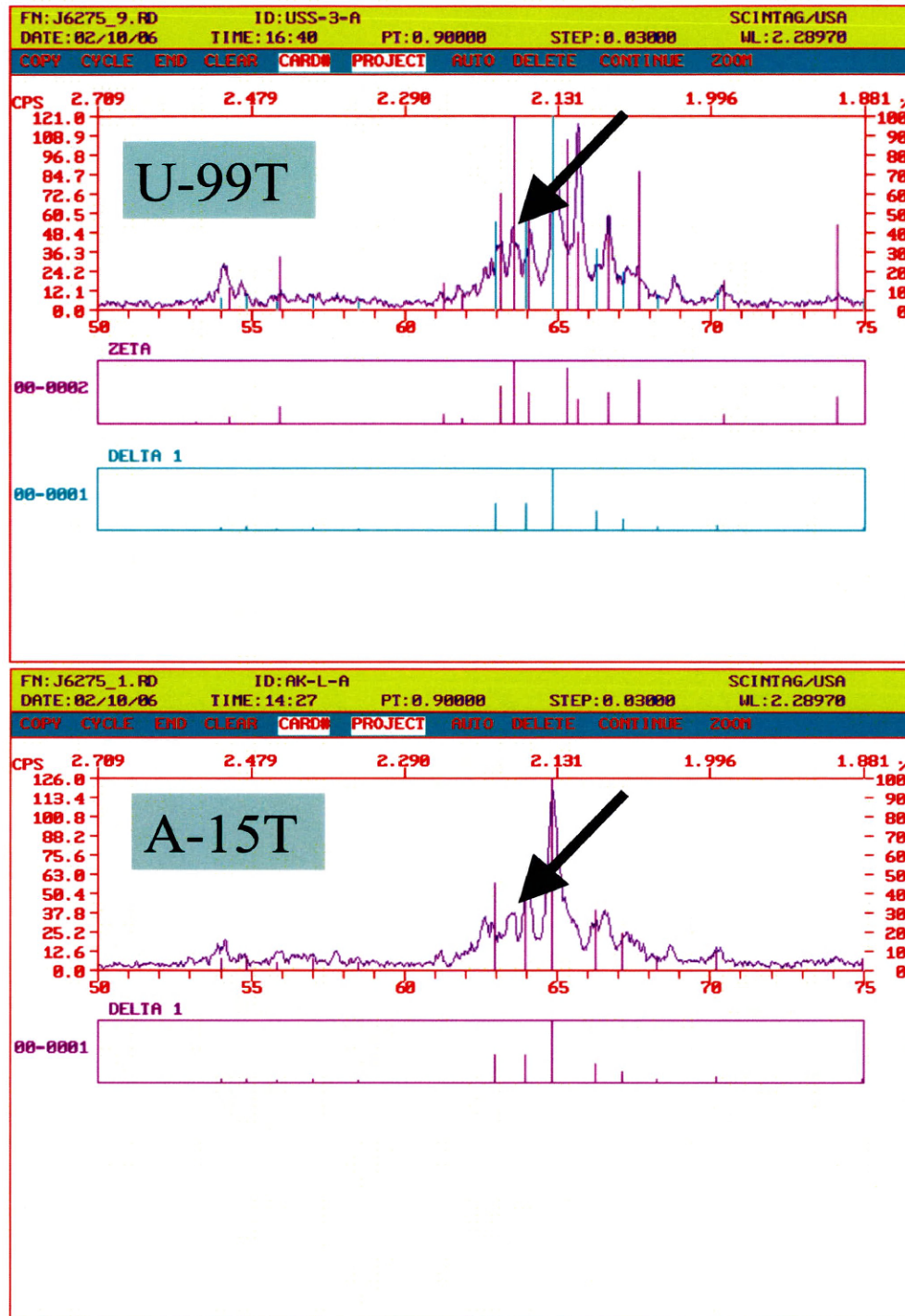
**Figure 4.9** **X-ray diffraction patterns of samples U-99T and A-15T.**
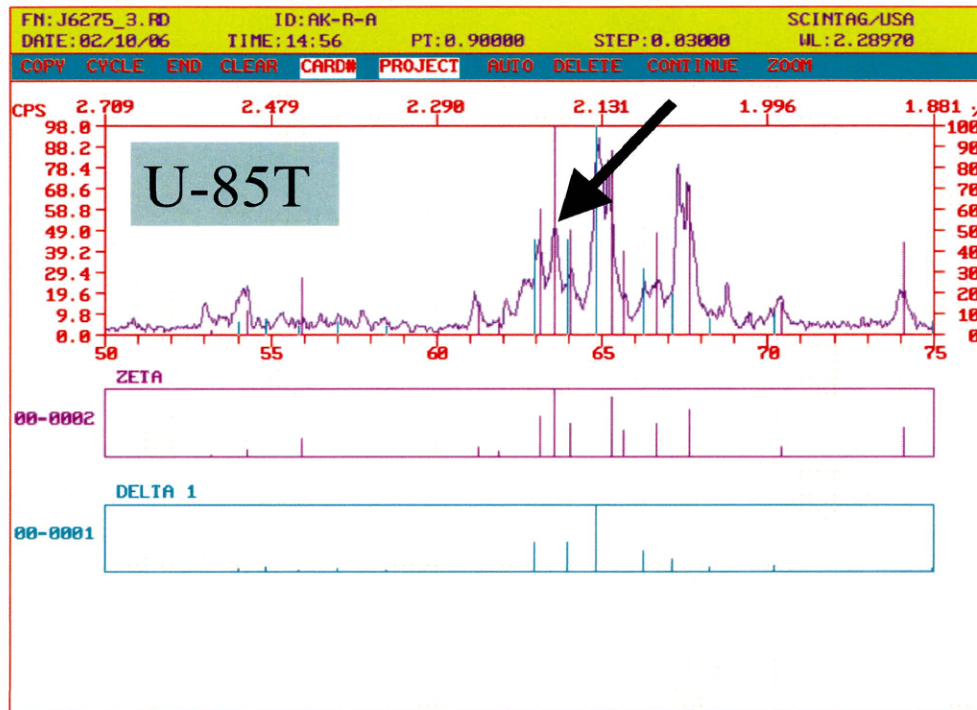
**Figure 4.10**      **X-ray diffraction patterns of sample U-85T.**

**Table 4.1**      **Intermetallic phase distributions on the surface of the coatings.**

| Sample | % of $\zeta$-phase at the surface | % of $\delta$-phase at the surface |
|---|---|---|
| I-00 | 0.0 | 100.0 |
| I-04 | 3.6 | 96.4 |
| I-92 | 92.4 | 7.6 |
| I-99 | 100.0 | 0.0 |
| UT-02 | 1.6 | 98.4 |
| UT-93 | 93.0 | 7.0 |
| UT-99 | 100.0 | 0.0 |
| AT-15 | 15.1 | 84.9 |
| AT-85 | 85.2 | 14.8 |

## 4.1.5 Roughness measurements

The roughness parameters were calculated from the 3D surface profiles. The procedures and description of the profiling technique, as well as the calculation and meaning of the parameters were described in Chapter 3. Roughness parameters were calculated for the as received coated samples as well as for the substrates. For the substrate roughness measurements, the coatings were stripped off with an HCl solution with an Fe inhibitor, a similar procedure described in Chapter 3 for the chemical analysis. The roughness parameter values for the coated sheets as well as for the substrates are presented in Table 4.2 and Table 4.3 respectively. The roughness of the ISG coatings (I-00, I-04, I-92, and I-99), as measured by the $R_q$ value, increased as the amount of $\zeta$-phase increased on the surface. This increase in roughness is also noticed on the SEM-SE images presented in Figure 3.5. The $R_q$ roughness value for the USS coatings (U-02T, U-93T, and U-99T) and AK coatings (A-15T and A-85T), also increased as the $\zeta$-phase on the coating increased, but the increase is much lower because of the temper rolled process that suppresses some of the high asperities. The roughness values of the substrates are very similar for all the sheets.

**Table 4.2          Roughness parameter values for coated samples.**

| Sample | $R_a$ ($\mu$m) | $R_q$ ($\mu$m) | $R_z$ ($\mu$m) | $R_t$ ($\mu$m) | $R_{sk}$ | $R_{ku}$ |
|--------|--------|--------|--------|--------|--------|--------|
| I-00   | 1.86 | 2.31 | 13.86 | 14.15 | 0.71 | 3.24 |
| I-04   | 2.19 | 2.67 | 16.15 | 16.21 | 0.22 | 2.55 |
| I-92   | 2.70 | 3.44 | 21.23 | 21.31 | 0.34 | 3.25 |
| I-99   | 2.77 | 3.49 | 20.32 | 20.38 | 0.19 | 3.04 |
| U-02T  | 1.49 | 1.91 | 11.42 | 11.44 | -1.15 | 4.36 |
| U-93T  | 1.18 | 1.60 | 10.53 | 11.35 | -1.83 | 6.66 |
| U-99T  | 1.61 | 2.04 | 11.44 | 11.46 | -1.05 | 3.69 |
| A-15T  | 1.61 | 2.05 | 11.33 | 11.35 | -1.27 | 4.15 |
| A-85T  | 2.07 | 2.60 | 13.33 | 13.36 | -1.41 | 4.27 |

| Table 4.3 | | | Roughness parameter values for uncoated samples. | | | |
|---|---|---|---|---|---|---|
| Sample | $R_a$ ($\mu$m) | $R_q$ ($\mu$m) | $R_z$ ($\mu$m) | $R_t$ ($\mu$m) | $R_{sk}$ | $R_{ku}$ |
| I-00 | 1.75 | 2.14 | 12.11 | 12.17 | 0.48 | 2.77 |
| I-04 | 1.52 | 1.87 | 10.61 | 10.97 | 0.61 | 2.90 |
| I-92 | 1.82 | 2.22 | 12.07 | 12.11 | 0.65 | 2.84 |
| I-99 | 1.65 | 2.05 | 11.72 | 11.78 | 0.66 | 3.04 |
| U-02T | 0.69 | 0.87 | 5.59 | 5.61 | 0.04 | 2.97 |
| U-93T | 0.68 | 0.85 | 5.13 | 5.14 | -0.20 | 2.74 |
| U-99T | 0.83 | 1.03 | 6.49 | 6.51 | 0.24 | 2.92 |
| A-15T | 0.81 | 1.03 | 8.64 | 9.56 | -0.18 | 3.28 |
| A-85T | 0.93 | 1.21 | 8.62 | 10.14 | 0.10 | 2.83 |

## 4.2 Coating Mechanical Testing: Friction and Powdering

This section presents the results of the mechanical testing performed on the coatings. The data presented represent the direct measurements of each individual test. The methodology used to calculate the different parameters is described in the Chapter 3. Trends and behaviors will be pointed out in this section, but the true interpretation of the data is presented in the Chapters 5 and 6.

### 4.2.1 Flat die tribometer

The flat die tribometer (FDT) is one of the most basic friction tests. The conditions under which the testing took place as well as the methodology to calculate the COF is described in the Chapter 3. Figure 4.11, Figure 4.12, and Figure 4.13 present the results from the FDT testing. Table 4.4 lists the COF measured by the FDT; values presented are the average of the values for different applied normal stresses. The COF values presented were calculated from the linear regressions as described in Chapter 3. The level of confidence was calculated from the average standard deviation of all the regressions. The calculated uncertainty of the COF values reported is ±0.003.

**Table 4.4**        **Coefficients of friction measured with the flat die tribometer.**

| Sample | COF |
|--------|-------|
| I-00   | 0.137 |
| I-04   | 0.141 |
| I-92   | 0.148 |
| I-99   | 0.159 |
| U-02T  | 0.137 |
| U-93T  | 0.164 |
| U-99T  | 0.166 |
| A-15T  | 0.154 |
| A-85T  | 0.164 |
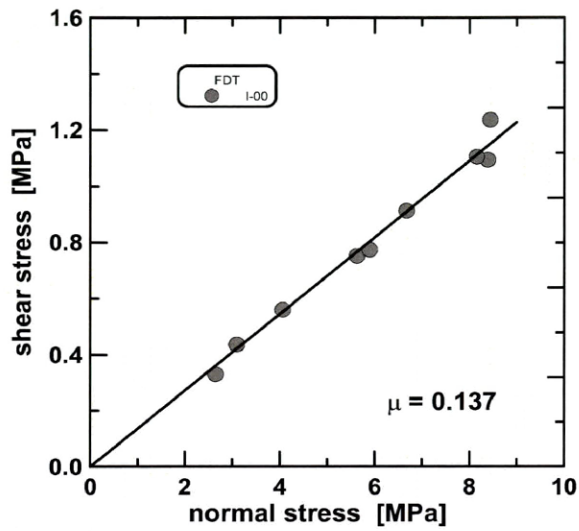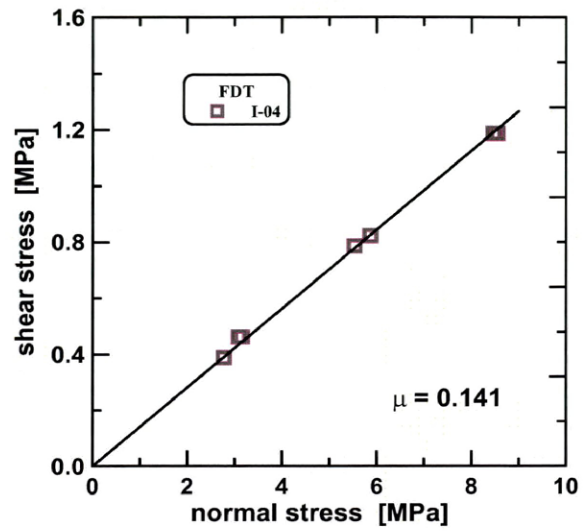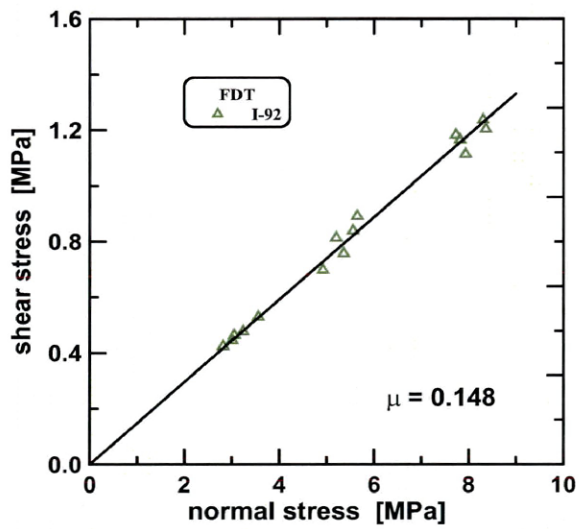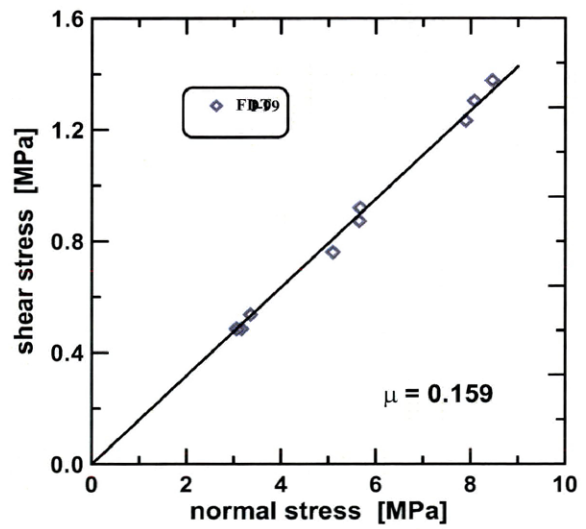
**Figure 4.11** Flat dies tribometer, normal stress—shear stress graphs for ISG sheets. (a) I-00, (b) I-02, (c) I-92, and (d) I-99.
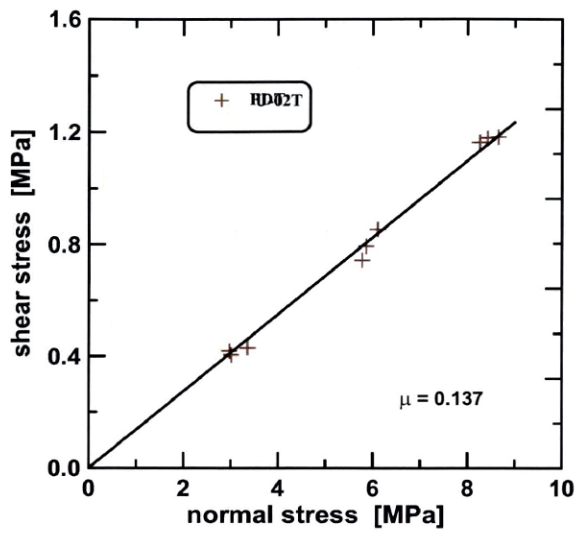
(a)
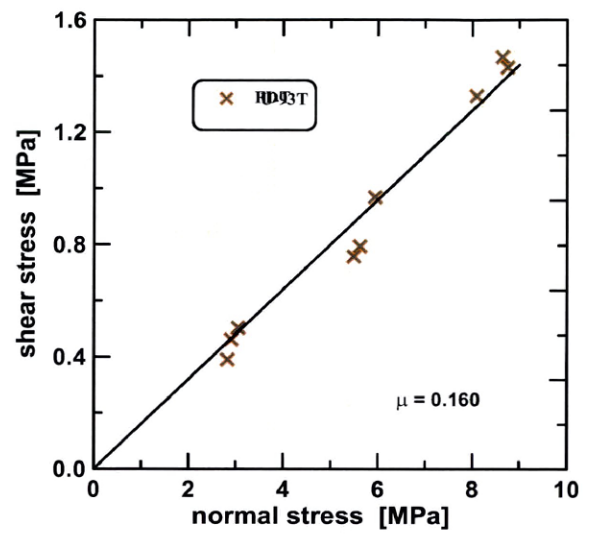


(b)
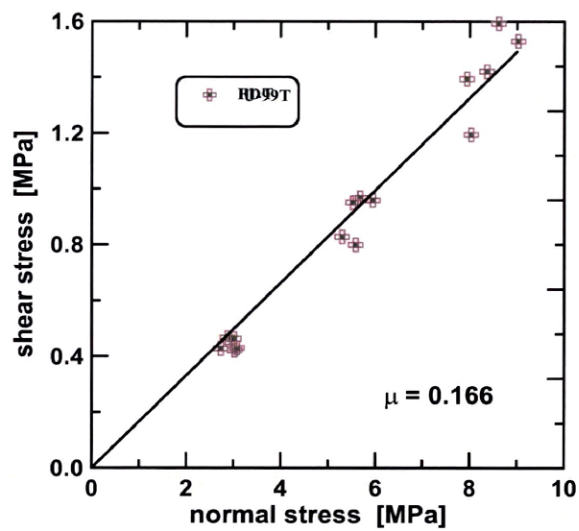


(c)

Figure 4.12    Flat die tribometer, normal stress—shear stress graphs for USS sheets.
(a) U-02T, (b) U-93T, and (c), U-99T.
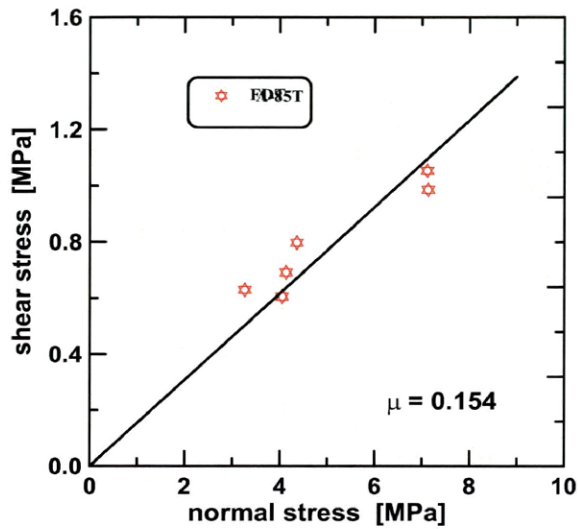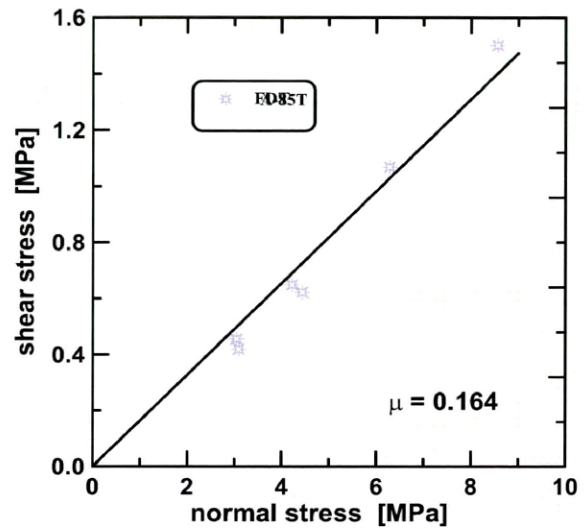
**Figure 4.13** Flat die tribometer, normal stress—shear stress graphs for AK sheets. (a) A150T, and (b) A-85T.

## 4.2.2 Bending under tension tribometer

The bending under tension tribometer (BUTT) is a common friction test. The testing methodology, sample preparation, as well as COF calculation methods were described in Chapter 3. Two different diameter dies were used: 50.8 mm diameter and 12.7 mm diameter. Table 4.5 presents the summary of COF measured with the BUTT, calculated with the Vallance and Matlock method. Table 4.6 presents the summary of COF measured with the BUTT, calculated with the Coubrough method. Figure 4.14, Figure 4.15, Figure 4.16, and Figure 4.17 present the summary of COF measured using the Vallance-Matlock method. The level of confidence was calculated from the average standard deviation of all the regressions for both methods. The calculated uncertainty of the COF values reported is ±0.003 for both methods.

| Table 4.5 | Coefficients of friction measured with the bending under tension tribometer, calculated with the Vallance & Matlock method. |
|:---|:---|

| Sample | COF 50.8 mm | COF 12.7 mm |
|:---|:---:|:---:|
| I-00 | 0.161 | 0.164 |
| I-04 | 0.168 | 0.160 |
| I-92 | 0.171 | 0.184 |
| I-99 | 0.188 | 0.196 |
| U-02T | 0.164 | 0.169 |
| U-93T | 0.168 | 0.181 |
| U-99T | 0.187 | 0.181 |
| A-15T | 0.165 | 0.174 |
| A-85T | 0.178 | 0.197 |

| Table 4.6 | Coefficients of friction measured with the bending under tension tribometer, calculated with the Coubrough method. |
|:---|:---|

| Sample | COF 50.8 mm | COF 12.7 mm |
|:---|:---:|:---:|
| I-00 | 0.174 | 0.173 |
| I-04 | 0.182 | 0.165 |
| I-92 | 0.187 | 0.186 |
| I-99 | 0.203 | 0.201 |
| U-02T | 0.178 | 0.172 |
| U-93T | 0.181 | 0.186 |
| U-99T | 0.202 | 0.186 |
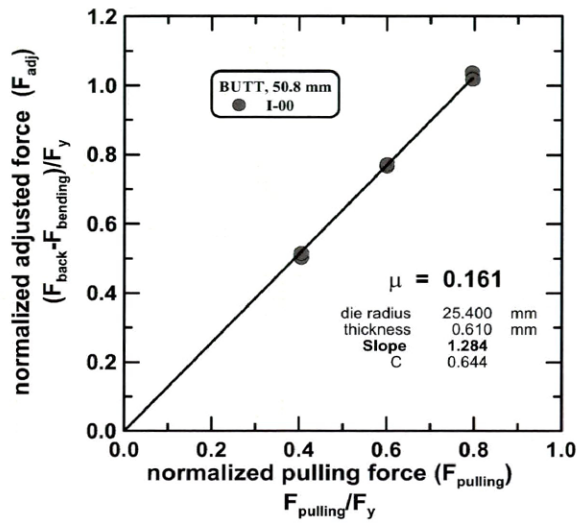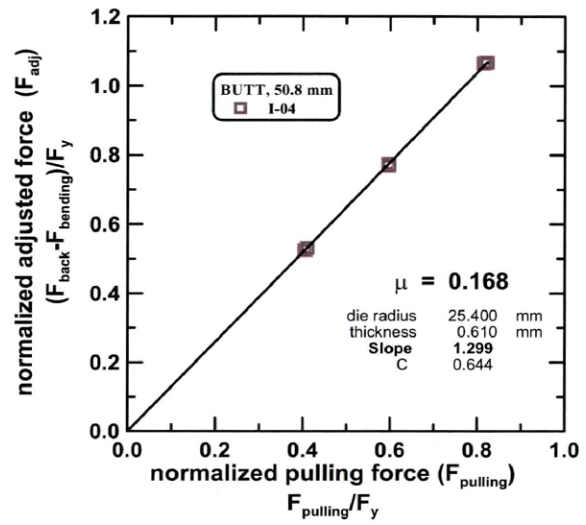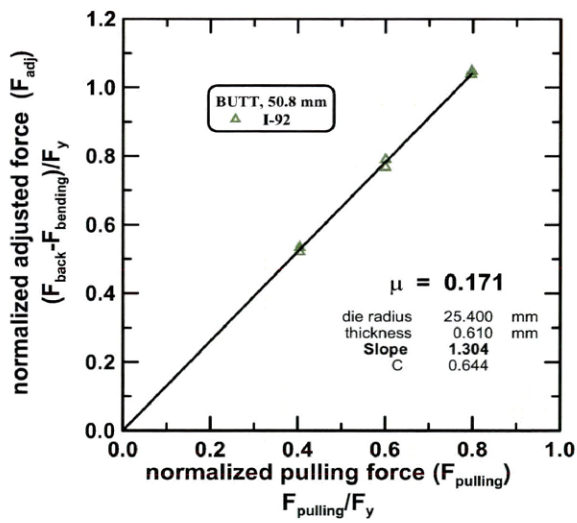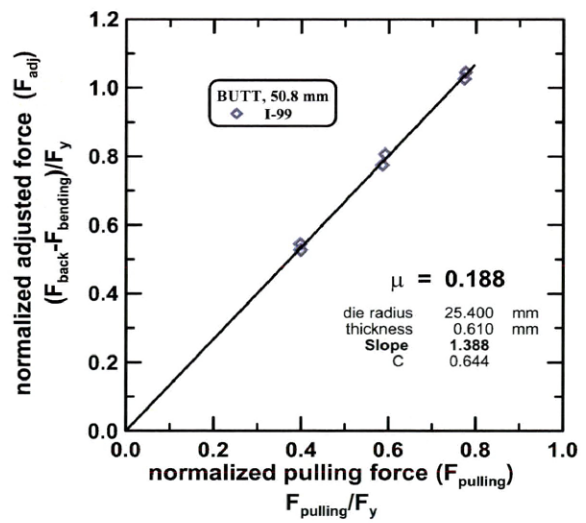
Figure 4.14    Bending under tension tribometer coefficients of friction for the ISG sheets, measured with the Vallance-Matlock method for the 50.8 mm diameter die.  (a) I-00, (b) I-02, (c) I-92, and (d) I-99.
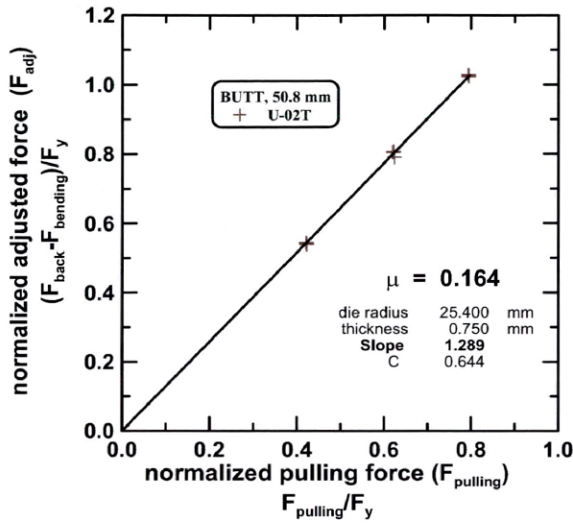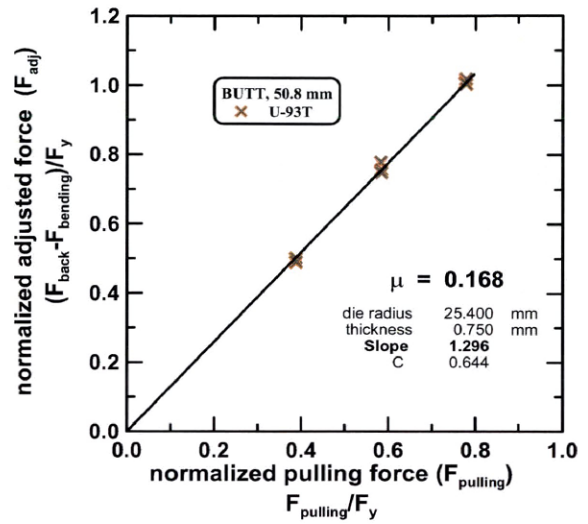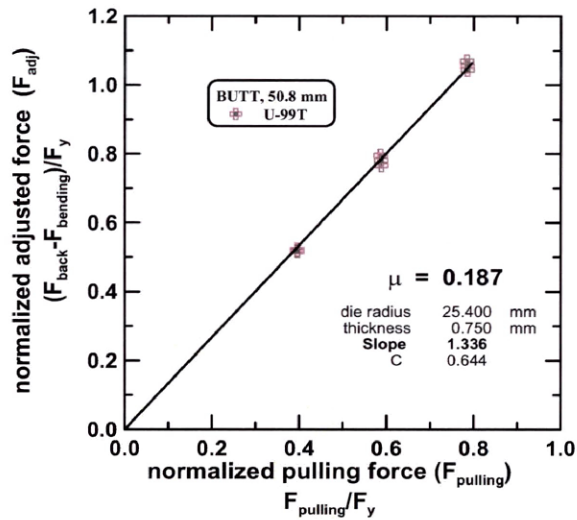
Figure 4.15    Bending under tension tribometer coefficients of friction for the USS sheets, measured with the Vallance-Matlock method for the 50.8 mm diameter die.  (a) U-02T, (b) U-93T, and (c) U-99T.

94
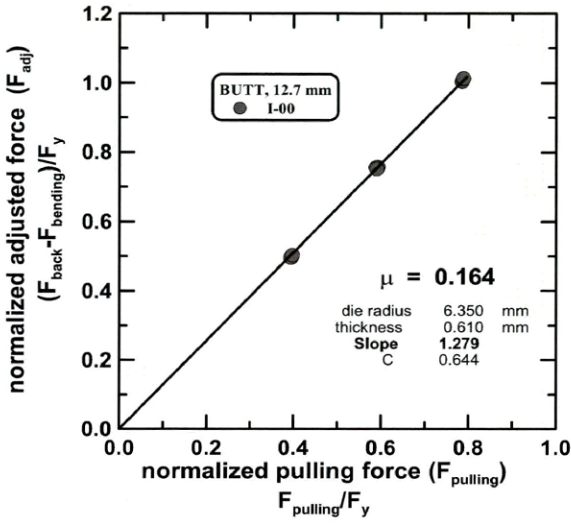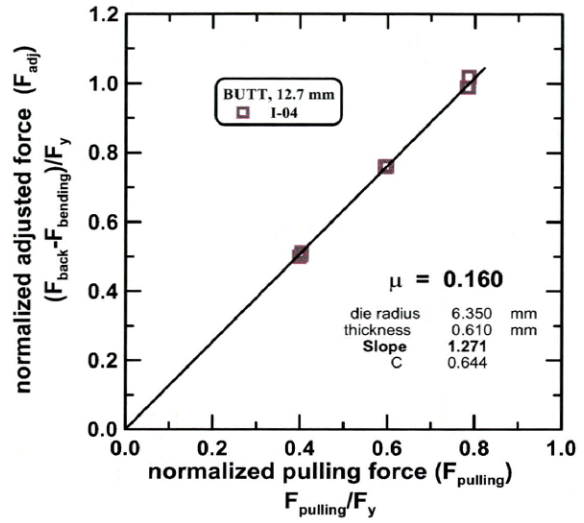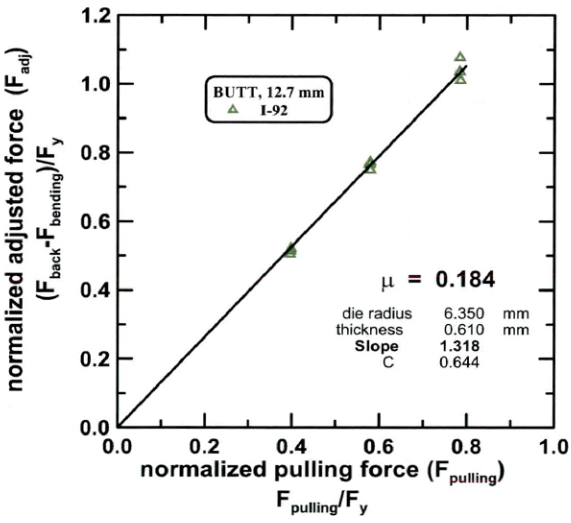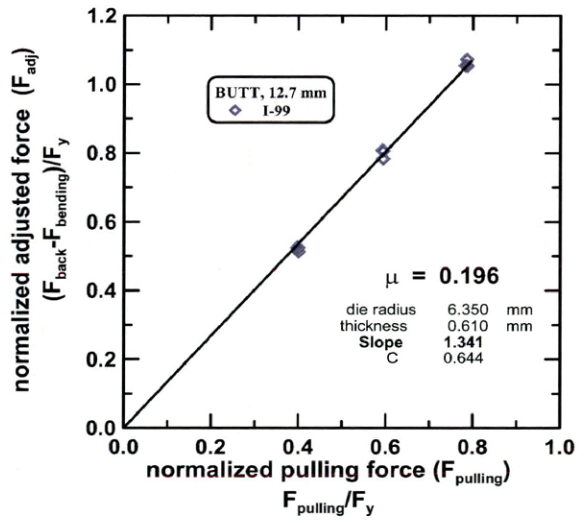
**Figure 4.16** Bending under tension tribometer coefficients of friction for the ISG sheets, measured with the Vallance-Matlock method for the 12.7 mm diameter die. (a) I-00, (b) I-02, (c) I-92, and (d) I-99.
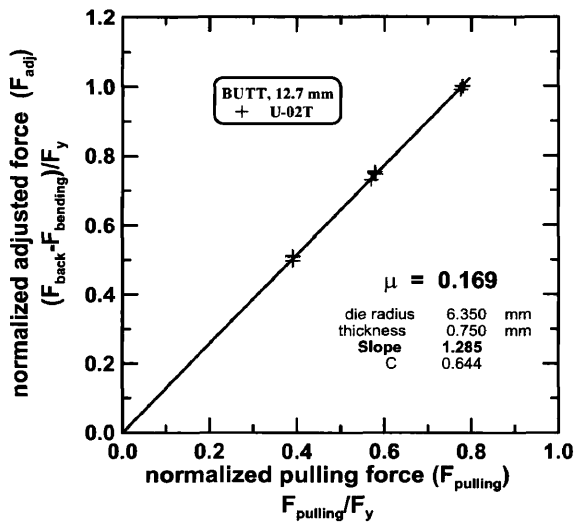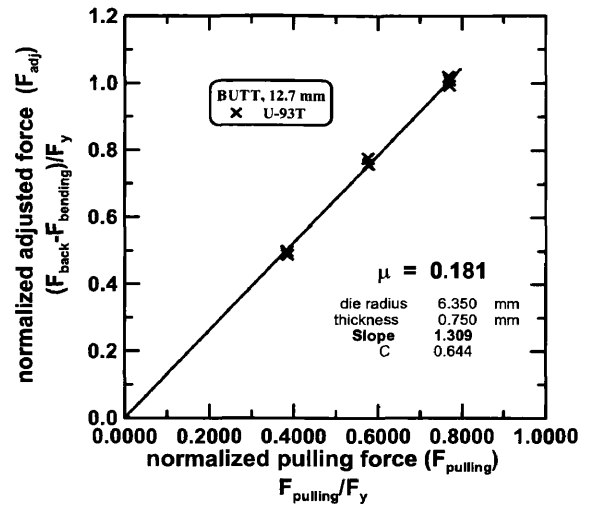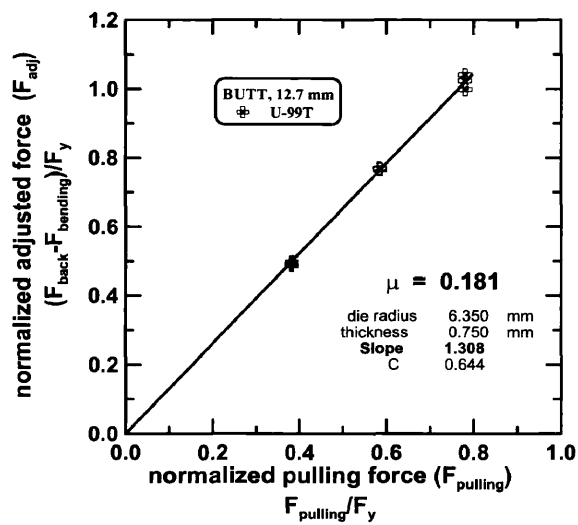
Figure 4.17    Bending under tension coefficients of friction for the USS sheets,
measured with the Vallance-Matlock method for the 12.7 mm diameter
die. (a) U-02T, (b) U-93T, and (c) U-99T.

96

## 4.2.3 Scratch test

The conditions under which the scratch testing was performed as well as the methodology to calculate the COF is described in the Chapter 3. Table 4.7 presents a summary of COF measured with the scratch test. Figure 4.18, Figure 4.19, and Figure 4.20 present the results of the scratch testing for the different sheets. The COF values presented on the table and in the figures is the slope of the normal force and the frictional force, measured from the figures. The level of confidence was calculated from the average standard deviation of all the regressions for both methods. The calculated uncertainty of the COF values reported is ±0.004.

**Table 4.7        Coefficients of friction measured with the scratch test.**

| Sample | COF |
| --- | --- |
| I-00 | 0.237 |
| I-04 | 0.256 |
| I-92 | 0.255 |
| I-99 | 0.279 |
| U-02T | 0.259 |
| U-93T | 0.280 |
| U-99T | 0.298 |
| A-15T | 0.255 |
| A-85T | 0.241 |
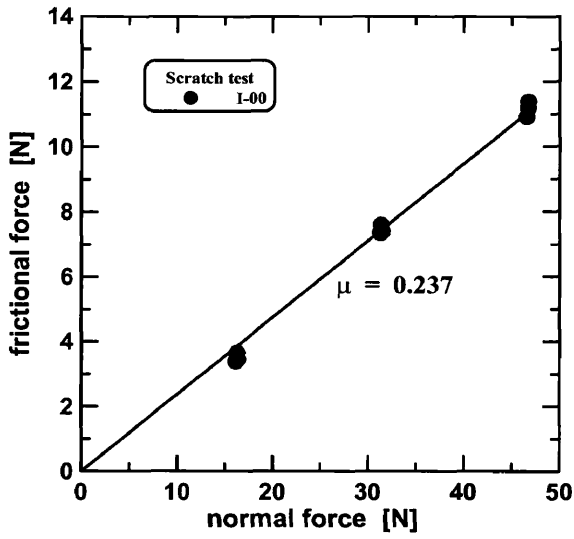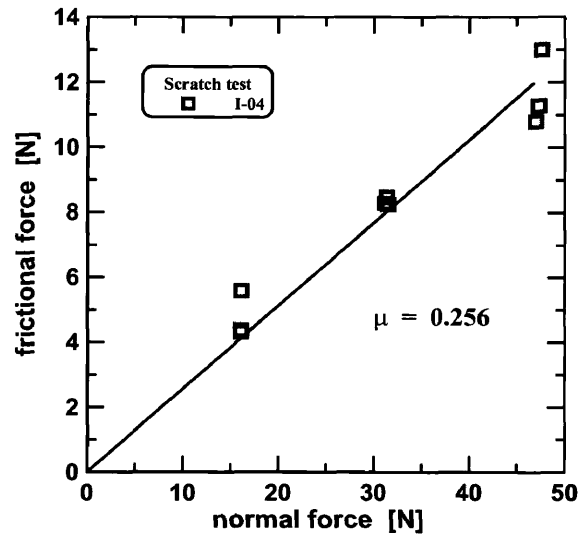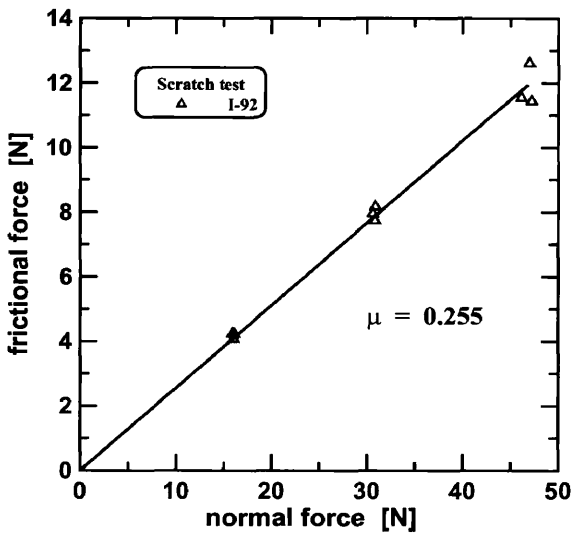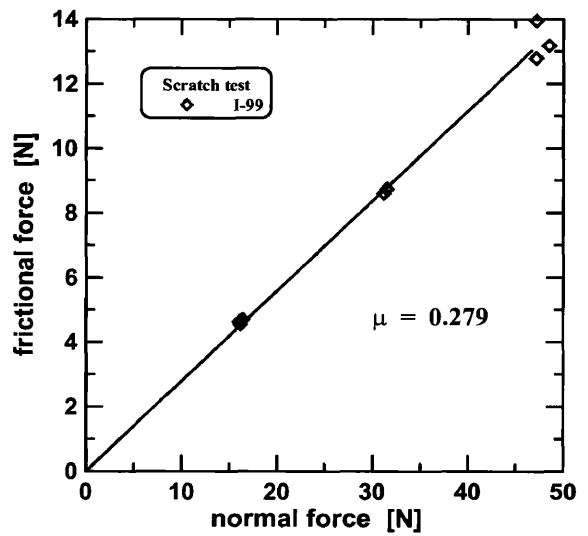
Figure 4.18    Scratch test results for ISG sheets.  (a) I-00, (b) I-02, (c) I-92, and (d) I-99.
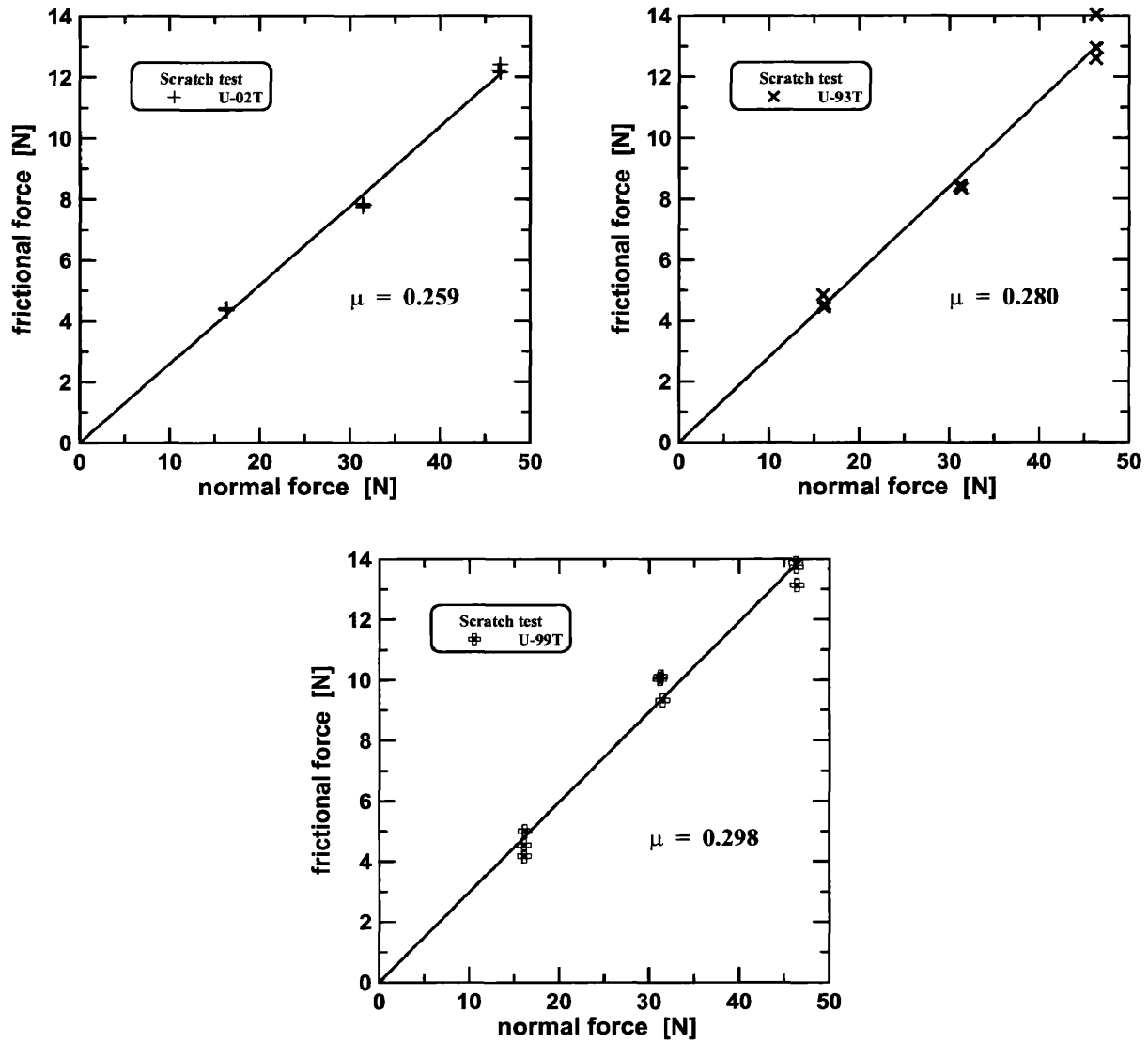
Figure 4.19    Scratch test results for USS sheets. (a) U-02T, (b) U-93T, and (c) U-99T.
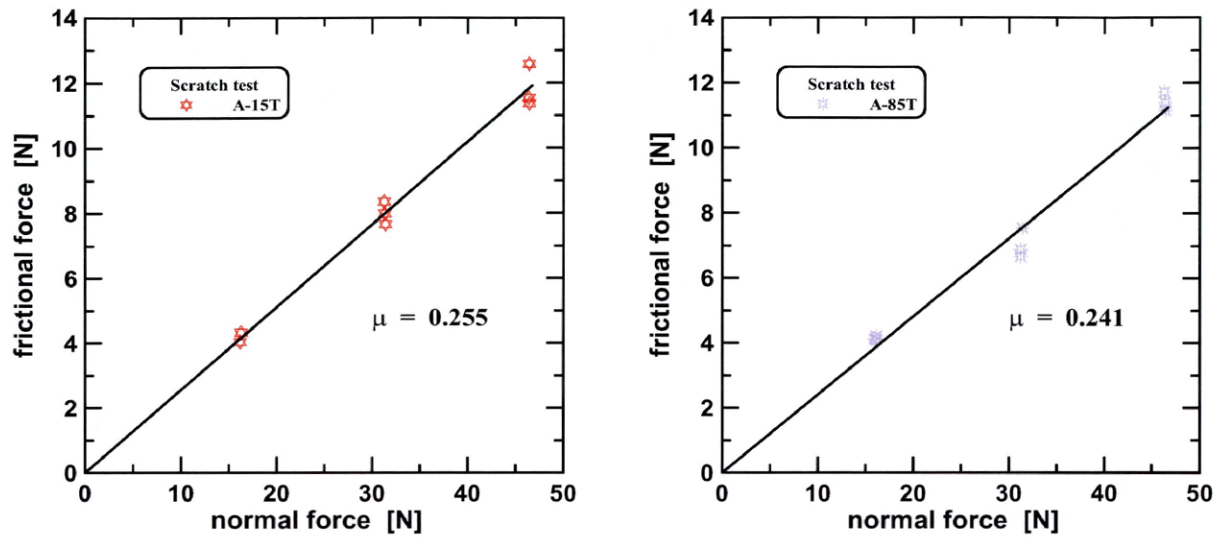
**Figure 4.20**    **Scratch test results for AK sheets.**

## 4.2.4 Limiting drawing ratio

To calculate the limiting drawing ratio, different blank diameters were drawn with a Swift punch. Details about the test and the methods to calculate the LDR are described in Chapter 3. Table 4.8 presents the list of LDR values for the different samples. The values of LDR show little variance, an expected result because all the samples represent basically the same substrate with similar mechanical properties. Nevertheless, samples I-92 and I-99, presented a lower value of LDR than samples I-00 and I-04 in the same manner as they showed a higher COF. In a similar way, samples U-93T and U-99T presented a slightly lower LDR than U-02T, which also showed a higher COF respectively. And lastly, A-85T presents lower LDR than A-15T.

| Table 4.8 | Limiting drawing ratios for the different sheets. |
|---|---|

| Sample | Limiting Drawing Ratio (LDR) |
|---|---|
| I-00 | 2.2125 |
| I-04 | 2.2125 |
| I-92 | 2.1875 |
| I-99 | 2.1875 |
| U-02T | 2.1875 |
| U-93T | 2.1875 |
| U-99T | 2.1750 |
| A-15T | 2.1875 |
| A-85T | 2.1750 |

## 4.2.5 Double-Olsen Powdering Test

To measure the powdering on the coatings, the double-Olsen test was performed. The methods and details for this test are described in Chapter 3. Table 4.9 presents the test results as metal loss per sample.

| Table 4.9 | Metal loss measured with the double-Olsen powdering test. |
|---|---|

| Sample | Metal Loss [mg] |
|---|---|
| I-00 | 10.12 |
| I-04 | 9.80 |
| I-92 | 8.75 |
| I-99 | 9.08 |
| U-02T | 10.32 |
| U-93T | 9.40 |
| U-99T | 4.80 |
| A-15T | 7.27 |
| A-85T | 4.63 |

## 4.3 Tested Samples Coating Characterization, Contact Area Quantification

Probability curves calculated from the 3D surface profiles were used to quantify real contact areas of tested samples as well as temper rolled coatings in the as-received conditions. The methodology and criteria are described in Chapter 3. The real contact area measures of single samples constitute the average of three measurements. Real contact area was not measured for all tested samples; however, at least one sample per testing condition was measured. The real contact area measurements were confirmed by observation of SEM-SE images.

The temper roll process is performed to provide quality control of the thickness of the finish sheet. This temper roll controls the roughness of the coating, reducing the final $R_t$ value, the difference between the higher and the lower profile value. The temper roll process smoothes the high asperities found in the coating, creating a fraction of flat asperities similar to mesas. These mesas could act as an instantaneous real contact area in a forming process. The percent of mesas of real contact area of the samples that were temper rolled such as U-02T, U-93T, U-99T, A-15T, and A-85T, is ~24 %. The measured real contact areas of the tested samples for the FDT, BUTT 50.8 mm roller die, and BUTT 12.7 mm roller die friction test are presented in Table 4.10, Table 4.11, and Table 4.12 respectively. The differences in real contact area are believed to be the cause of the differences in COF and will be discussed in Chapters 5 and 6. The level of confidence of the contact area measurements reported, is ±1.6 % for the ISG coatings (I-00, I-04, I-92, and I-99), while the level of confidence for the rest of the coatings (U-02T, U-93T, U-99T, A-15T, and A-85T) is ±6.4 %. These uncertainties were calculated by averaging the standard deviations of all the measurements. The uncertainty of the real contact area measurements of the ISG coatings is lower than the rest of the samples because the ISG coatings were not temper rolled, making the height distributions easier to analyzed.

**Table 4.10      Real contact area of flat die tribometer samples.**

| Sample | applied normal stress MPa | real contact area percent |
|--------|---------------------------|---------------------------|
| I-00   | 4.1                       | 3.0                       |
|        | 6.7                       | 4.3                       |
|        | 8.2                       | 6.7                       |
| I-04   | 3.1                       | 3.7                       |
|        | 5.5                       | 6.0                       |
|        | 8.6                       | 7.0                       |
| I-92   | 3.6                       | 7.7                       |
|        | 5.6                       | 8.0                       |
|        | 7.7                       | 9.3                       |
| I-99   | 3.2                       | 5.3                       |
|        | 5.7                       | 10.0                      |
|        | 8.1                       | 13.3                      |
| U-02T  | 3.4                       | 6.3                       |
|        | 5.8                       | 9.0                       |
|        | 8.7                       | 17.3                      |
| U-93T  | 3.1                       | 26.0                      |
|        | 6.3                       | 36.0                      |
|        | 8.7                       | 45.3                      |
| U-99T  | 3.1                       | 14.0                      |
|        | 5.6                       | 27.0                      |
|        | 9.0                       | 40.0                      |
| A-15T  | 3.3                       | 19.7                      |
|        | 4.4                       | 34.0                      |
|        | 7.1                       | 10.0                      |
| A-85T  | 3.1                       | 10.3                      |
|        | 6.3                       | 6.7                       |
|        | 8.6                       | 35.0                      |

| Table 4.11 | Real contact area of bending under tension tribometer 50.8 mm roller die diameter samples. |
| --- | --- |

| Sample | applied normal stress MPa | real contact area percent |
| --- | --- | --- |
| I-00 | 1.7 | 3.7 |
| | 2.6 | 4.7 |
| | 3.4 | 6.0 |
| I-04 | 1.7 | 4.3 |
| | 2.5 | 5.7 |
| | 3.4 | 6.3 |
| I-92 | 1.6 | 9.3 |
| | 2.4 | 9.7 |
| | 3.2 | 11.3 |
| I-99 | 1.6 | 10.3 |
| | 2.4 | 12.7 |
| | 3.1 | 16.0 |
| U-02T | 2.8 | 10.3 |
| | 4.1 | 17.3 |
| | 5.2 | 27.3 |
| U-93T | 2.4 | 30.0 |
| | 3.6 | 38.7 |
| | 4.8 | 40.0 |
| U-99T | 2.7 | 26.0 |
| | 4.0 | 27.3 |
| | 5.4 | 40.7 |

| Table 4.12 | Real contact area of bending under tension tribometer 12.7 mm roller die diameter samples. | |
|---|---|---|
| Sample | applied normal stress MPa | real contact area percent |
| I-00 | 7.5 | 9.7 |
| | 10.9 | 13.3 |
| | 14.3 | 15.0 |
| I-04 | 7.3 | 10.3 |
| | 10.6 | 12.3 |
| | 13.8 | 17.3 |
| I-92 | 7.2 | 16.0 |
| | 10.1 | 19.3 |
| | 13.3 | 22.7 |
| I-99 | 7.4 | 20.0 |
| | 10.7 | 22.7 |
| | 13.7 | 25.0 |
| U-02T | 11.6 | 30.0 |
| | 16.2 | 36.0 |
| | 21.7 | 46.0 |
| U-93T | 10.9 | 32.0 |
| | 15.7 | 40.7 |
| | 20.4 | 47.0 |
| U-99T | 11.6 | 34.0 |
| | 17.2 | 44.7 |
| | 22.3 | 50.3 |

# CHAPTER 5

# FORMABILITY BEHAVIOR OF GALVANNEALED COATED STEEL SHEETS: FRICTION AND POWDERING DISCUSSION

This chapter presents the behaviors and trends found in the testing results of Chapter 4. The behaviors presented are followed by an analysis of the causes for the behavior. The findings serve to formulate the friction model presented in the Chapter 6. This chapter is divided in three sections: first the friction testing observations, followed by the formability test and LDR analysis, and finally the powdering test analysis.

## 5.1 Friction Testing Observations

This section presents the observations and discussion resulting from friction testing. First, it describes trends indicated by the flat die tribometer testing, and then presents observations of the bending under tension tribometer. Finally, it summarizes the findings and observations common to both testing methods.

### 5.1.1 Flat die tribometer observations

The flat die tribometer (FDT) is in principle a very simple friction test; however, the implementation of the test is somewhat complex. By nature, the friction calculation from the FDT is the simplest, and since the sample is not subject to deformation by bending, the stress measurements are direct. Some plastic deformation takes place during the test, and as will be demonstrated, variation in the contact area under normal stress provides evidence that plastic deformation occurs in the coating. Uniaxial tension deformations were avoided by maintaining the pulling stresses below the yield strength of the samples.

The first step in trying to determine a behavior of the coefficient of friction (COF) of the galvannealed coatings (GA) is to compare it with the iron content in the coating. As Figure 5.1 shows, the COF presents a well-behaved trend in which the COF increases as the

amount of Fe in the coating decreases. The same COF are plotted as a function of the amount of $\zeta$-phase percent present at the surface of the coating as shown in Figure 5.2.
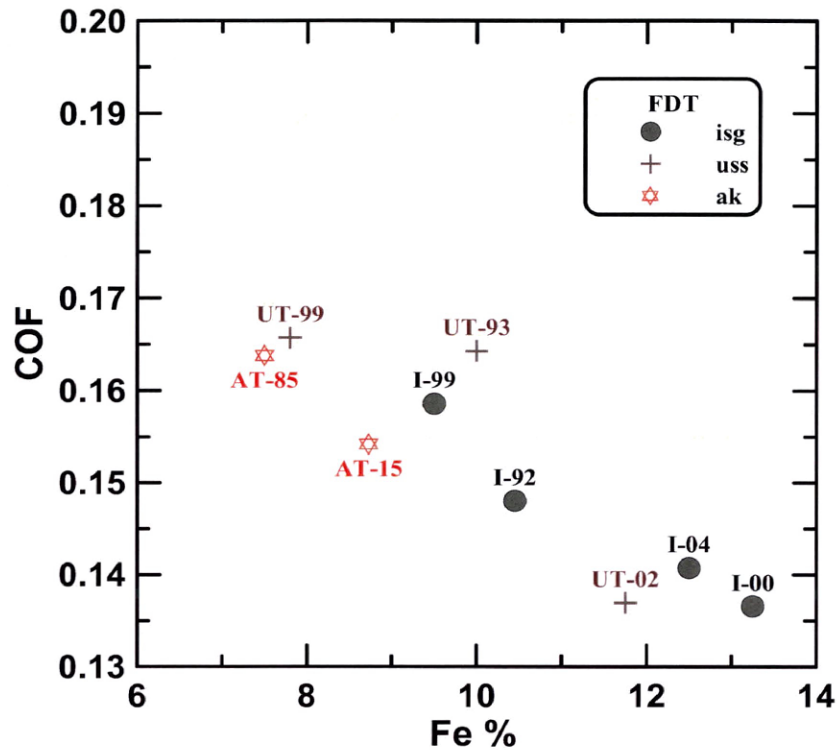


**Figure 5.1**      **Flat die tribometer COF plotted as a function of Fe wt % in the coating.**

The COF behavior presented Figure 5.1 could give the impression that friction is controlled by the amount of Fe in the coating. However, the samples I-92, I-99, U-93T, and A-15T, which contain similar amounts of Fe in the coating, have a range of COF values from 0.148 to 0.164. In observing the differences in Figure 5.2, the samples with high percent of $\zeta$-phase on the surface (I-92, I-99, U-93T, U-99T, and A-85T) had range of values of COF, from 0.148 to 0.166. Although containing similar amounts of $\zeta$-phase on the coating, the phase which is thought to control the COF, samples U-93T, U-99T, and A-85T which are temper rolled before testing, have a higher COF as compared to samples I-92 and I-99. Samples with lower amounts of $\zeta$-phase have lower COF, temper rolled or not.
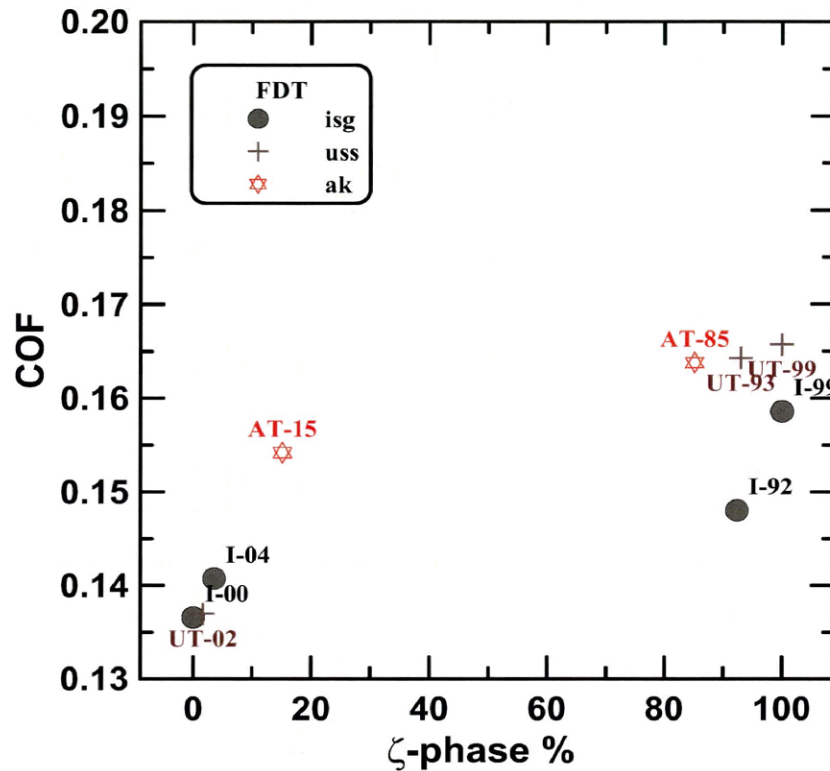
**Figure 5.2**      **Flat die tribometer COF plotted as a function of amount of $\zeta$-phase percent present on the surface of the coating.**

The COF values calculated for each individual test are presented as a function of applied normal stress as in Figure 5.3. While Figure 5.3 presents many dispersed data points, some subtle trends can be observed. Each individual coating shows a slight increase of COF with increase of applied normal stress. For each normal stress level, the coatings with less $\zeta$-phase on the surface such as I-00, I-04, and U-02T, appear in the lower part with of the plot with a lower COF than the coating with higher $\zeta$-phase percent, such as I-99, U-93T, and U-99T.

A similar but more well-defined trend is found when the real contact areas are plotted as a function of the applied normal stress, Figure 5.4. In the figure the trends for samples I-00 and I-99 have been indicated by dotted lines, as well as trends for samples U-93T and U-99T. It is clear that the real contact area increases as the applied normal stress increases.

This increase is greater for samples that contain larger amounts of ζ-phase compared to the samples that contain little or no ζ-phase on the surface.

In summary, the first observation indicates some connection of the COF with the amount of Fe in the coating, an observation commonly seen in the literature [59,60,61,62]. The amount of ζ-phase at the surface of the coating appears to be a more significant factor affecting the COF between the samples. The temper rolled characteristic of some of the samples has the effect of increasing the COF as compared to the samples that were not temper rolled. Finally, a common trend is indicated when all the COFs are plotted with the applied normal stress, and the same trend is followed by the real contact area. This last observation raises the question of a relationship between the increase of COF with applied normal stress and the increase of real contact area with applied normal stress.
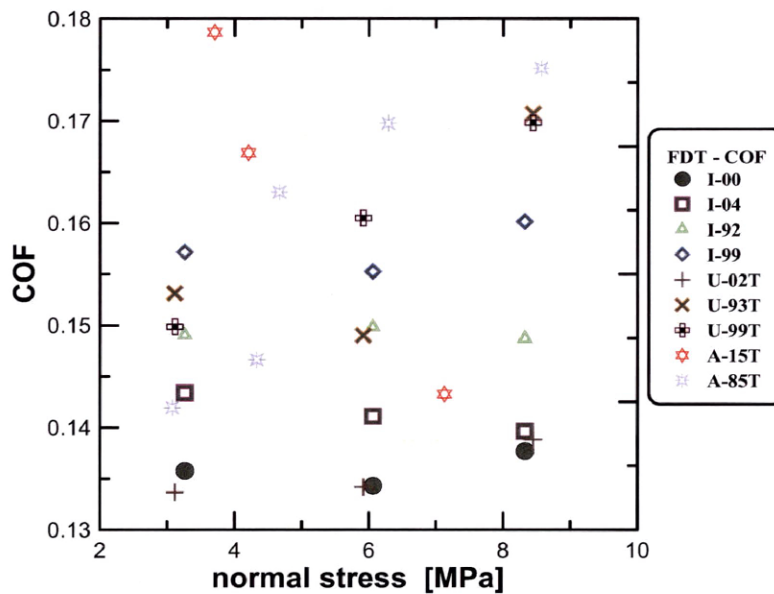


Figure 5.3    Flat die tribometer coefficients of friction plotted as a function of applied normal stress.
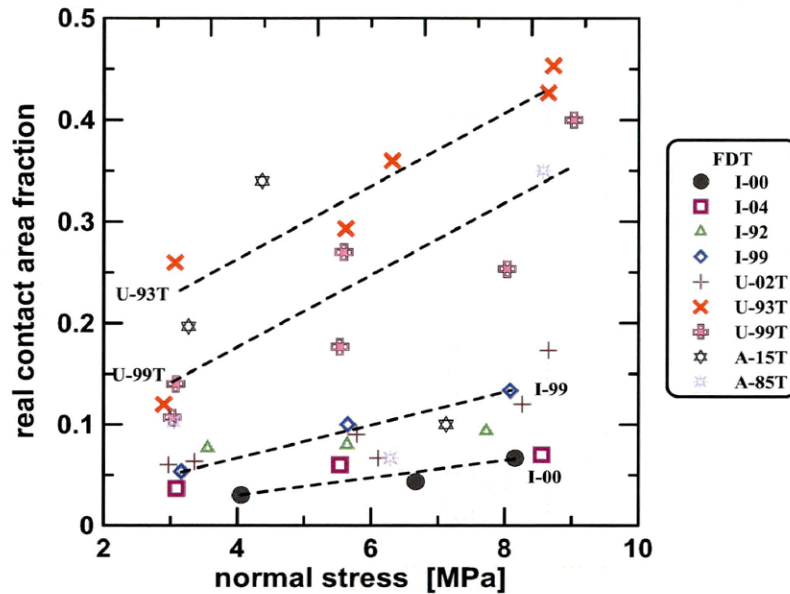
**Figure 5.4**     **Flat die tribometer real contact area as a function of the applied normal stress.**

## 5.1.2 Bending under tension tribometer observations

The bending under tension tribometer (BUTT) is a common friction test. The test involves a bending and unbending a sample, a process which makes the friction calculations more complicated. At the same time, the nature of the test simulates closely a forming operation, where bending and friction happen at the same time. Different roller dies can be used to measure COF, and it is known that the COF value calculations for larger roller diameter roller dies present very similar results compared to smaller roller diameters where the COF calculations differ more [52]. However, forming processes often require small radii, creating the need to measure the COF using small roller dies. In this study, two roller die diameters were used, 50.8 mm and 12.7 mm.

Figure 5.5 shows the COF measured with the BUTT each of the two roller die diameters. As with the FDT, these calculated COF represented a trend where the COF increases with a decrease in Fe content in the coatings. On average, the COF values shown in the 12.7 mm roller die are higher than the ones shown in the 50.8 mm roller die. When

observing the distribution of COF plotted as function of $\zeta$-phase percent at the surface of the coating in Figure 5.6, there are some noticeable separations. The COF of the samples with largest percent of $\zeta$-phase show the highest values in the 12.7 mm diameter roller die, while in the 50.8 mm diameter roller die, the COF shown are more scattered.

The COF are plotted as a function of the applied normal stress for both roller die diameters in Figure 5.7. Again, as observed with the FDT, individual trends are seen, where for each coating and for each roller die diameter, the COF data tend to increase with the applied normal stress. In Figure 5.8, the real contact area of the BUTT samples are plotted as a function of the applied normal stress. It clearly shows how the real contact area increases with applied normal stress, not only among the samples that share similar amounts of $\zeta$-phase at the surface, but the trend is also common between the two roller die diameters. This increase of contact area with applied normal stress is a clear indication of a commonality in between the different friction tests.

112
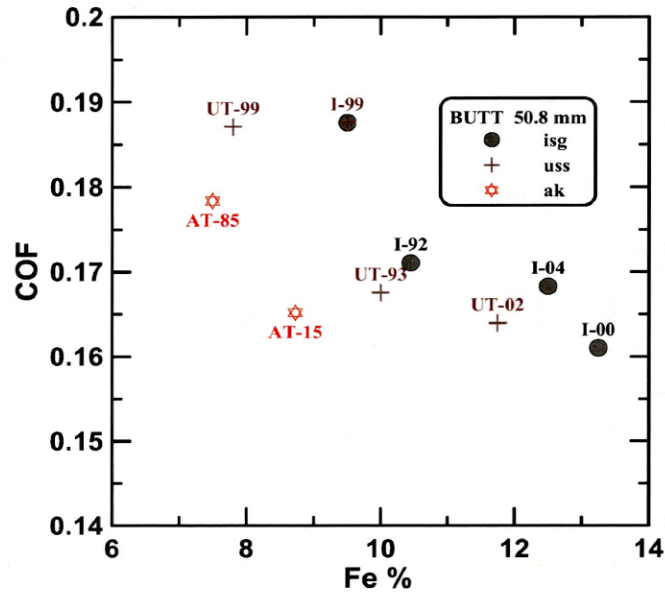
(a)
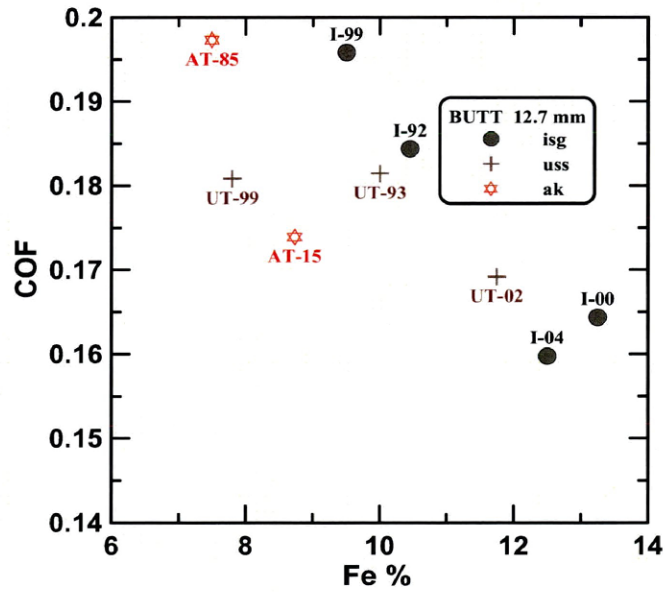


(b)

**Figure 5.5**    Bending under tension tribometer coefficients for friction plotted as a function of Fe wt% in the coating.  (a) Coefficients of friction measured with the 50.8 mm roller die; (b) coefficients of friction measured with the 12.7 mm roller die.
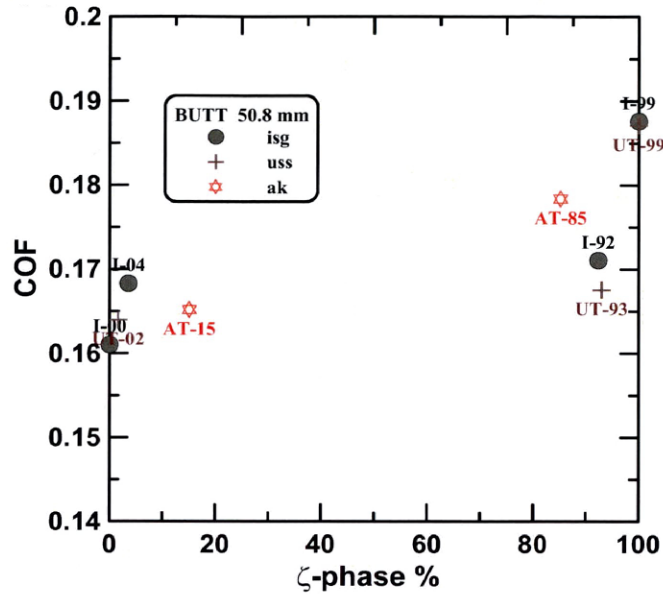
(a)
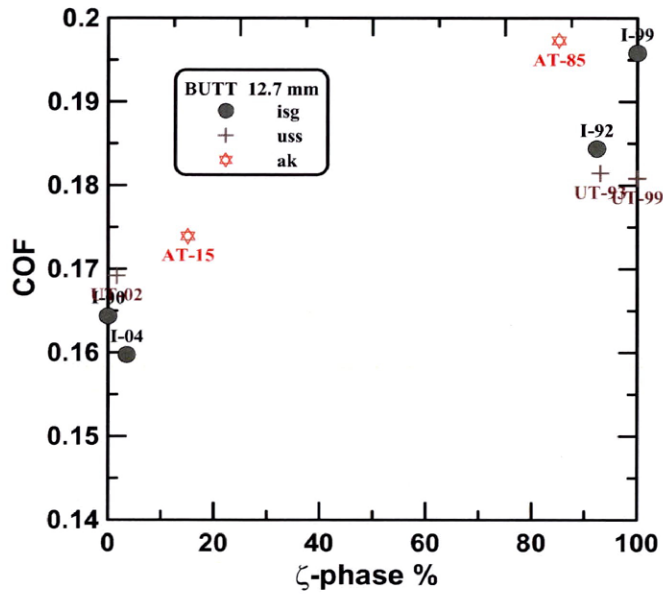


(b)

**Figure 5.6**      Bending under tension tribometer coefficients of friction plotted as a function of ζ-phase percent at the surface of the coating. (a) Coefficients of friction measured with the 50.8 mm roller die; (b) coefficients of friction measured with the 12.7 mm roller die.

114
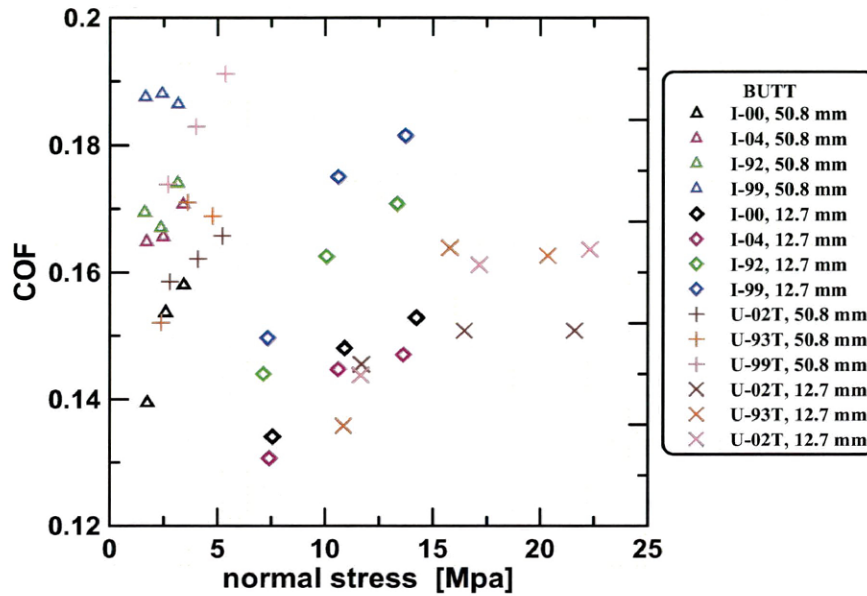
**Figure 5.7**    Bending under tension tribometer coefficients of friction plotted as a function of the applied normal stress.
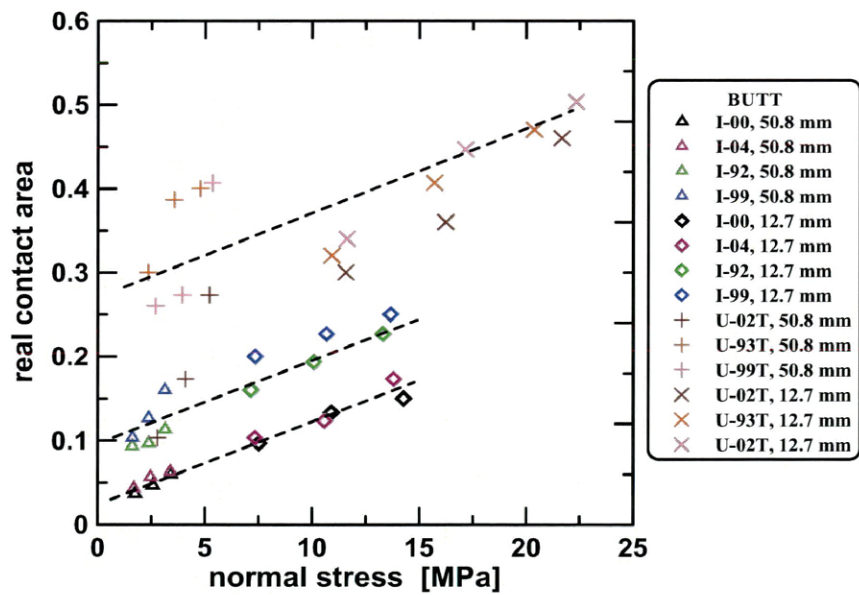


**Figure 5.8**    Real contact area as a function of applied normal stress for the samples tested with the bending under tension tribometer.

### 5.1.3 Coating surface deformation during friction testing

Every friction sample had some fraction of contact area due to flattening. Samples that contain $\zeta$-phase at the surface, for a given applied normal stress, showed a higher real contact area when compared to samples that did not contain $\zeta$-phase. The GA coating is often considered brittle, however it is reported that the $\zeta$-phase becomes ductile at temperatures above 150 °C [63]. Micrographs of tested samples show that the $\zeta$-phase is flatten and compacted into a thinner layer (Figure 5.9). The micrographs also show no evidence of extraction or decohesion of the $\zeta$-phase. The $\zeta$-phase deformed and redistributed into itself, creating a flat area of contact as shown in Figure 5.9. In the coatings that contain no $\zeta$-phase on the surface, the asperities of the $\delta$-phase are worn down. There is no indication of any major plastic deformation, Figure 5.10. The cracking behavior of the two coatings is very different when comparing both figures. Sample I-99 does not exhibit any extraordinary cracking. On the other hand, for sample I-00 the contact zone shows heavy cracking, some of which seems to penetrate into the substrate. The two samples shown in Figure 5.9 and Figure 5.10 are from samples tested with the FDT, which were not subjected to any bending. In a forming process that involves bending, the cracking severity presented by sample I-00 in Figure 5.10, would had result in powdering and even flaking defects.

Samples tested with the BUTT exhibit similar results; however, the bending and unbending creates more cracking and decohesion of the coating. Figure 5.11 and Figure 5.12 show micrographs of samples I-99 and I-04 respectively, tested with the BUTT 12.7 mm roller die diameter at ~14 MPa. The cracking and decohesion of the coating is more severe in sample I-04, where some of the cracks penetrate into the coating. Latter in this chapter, a discussion of the relationship of real contact area, COF, and cracking behavior is presented, and the difference between these two behaviors is explained.

116
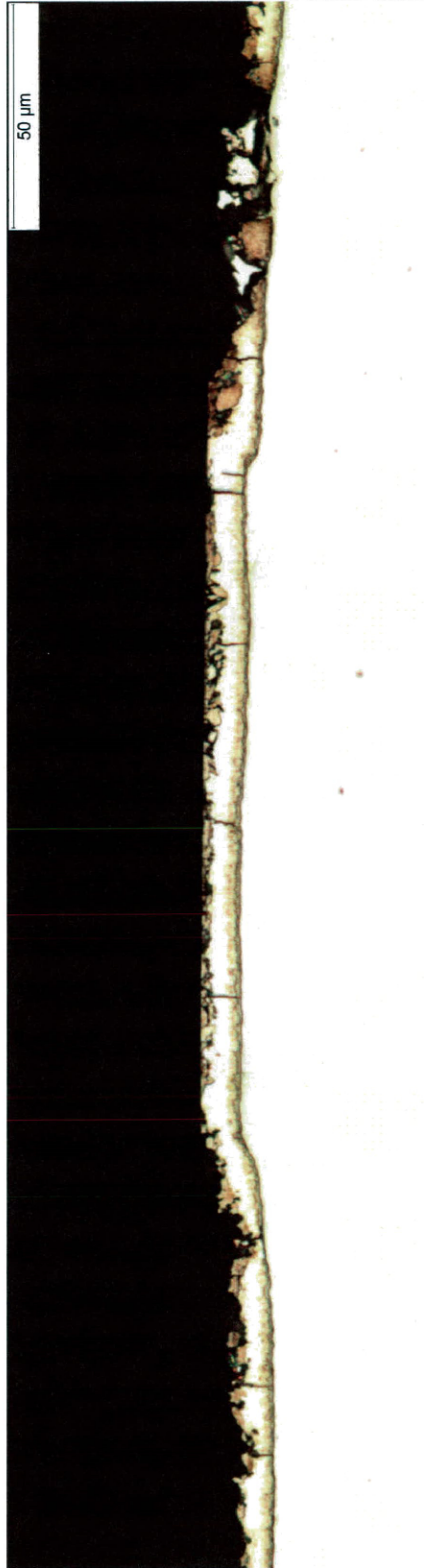
**Figure 5.9** Flat die tribometer I-99 sample tested at ~6 MPa of applied normal stress. Cross section view parallel to the test direction.

117
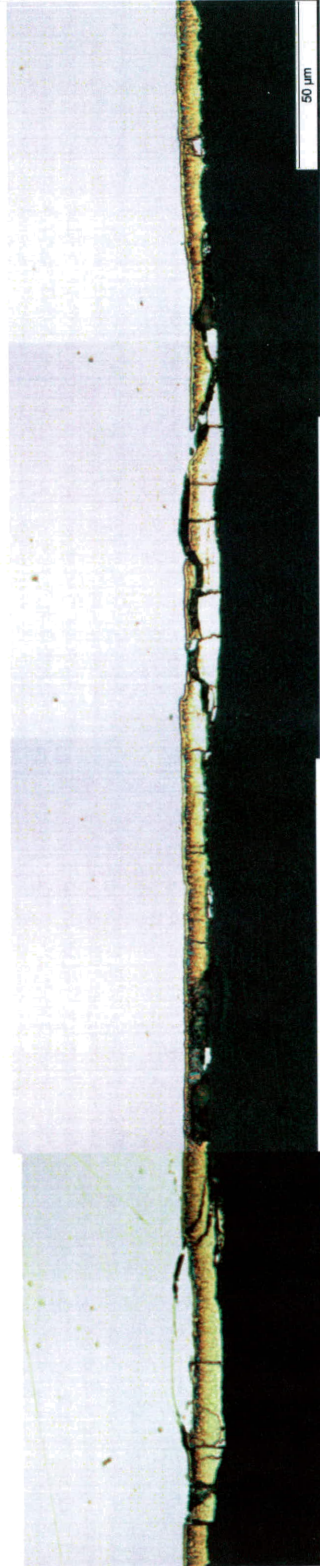
**Figure 5.10**    Flat die tribometer I-00 sample tested at ~ 8 MPa of applied normal stress.  Cross section view parallel to the test direction.
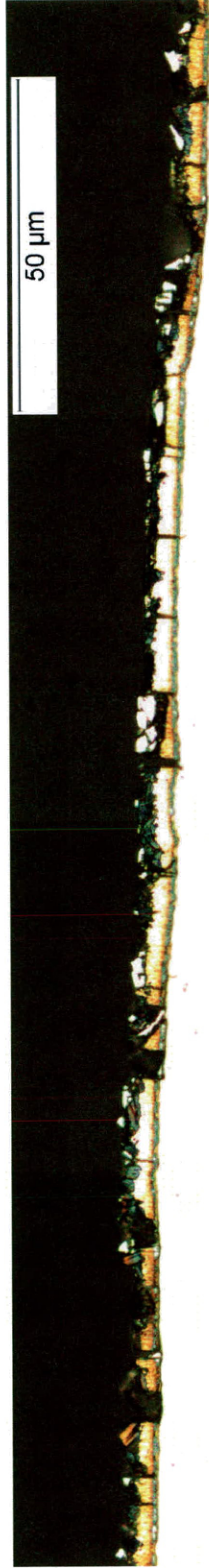
**Figure 5.11** Bending under tension tribometer sample I-99 tested at ~14 MPa of applied normal stress. Cross section view parallel to the test direction.
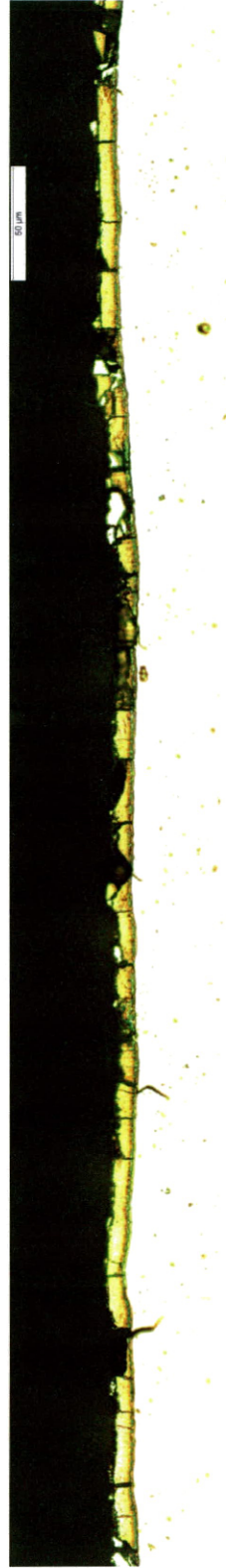
**Figure 5.12**  Bending under tension tribometer sample I-04 tested at ~14 MPa of applied normal stress.  Cross section view parallel to the test direction.

## 5.1.4 Friction testing observations summary

The friction testing behavior showed that individually each coating follows a common trend. As the COF increases with the applied normal load, the increment is larger for samples that contain $\zeta$-phase on the surface when compared to samples with little or no $\zeta$-phase. When comparing the coatings with each other, the COF increases as the amount of $\zeta$-phase at the surface of the coating increases, and the COF also increases with decreasing Fe wt% in the coating. This increase of COF with $\zeta$-phase is accentuated when the coating had been temper rolled.

When comparing the results of test with each other, the FDT, BUTT with 50.8 mm roller die diameter, and BUTT with 12.7 mm roller die diameter (as if combining Figure 5.3 and Figure 5.7 where the COF are plotted as a function of applied normal stress) no common trend was evident. On the other hand, after observing the development of the real contact area with normal stress, the different tests follow a common trend. Figure 5.13 shows the real contact area of samples I-00, I-99, and U-99T plotted as a function of normal stress for three different tests, the FDT and the BUTT with the two roller die diameters. The behavior of the contact area with normal stress has been indicated previously for a single type of test [59,64,65,66], while in this study the same behavior is observed across three different tests.
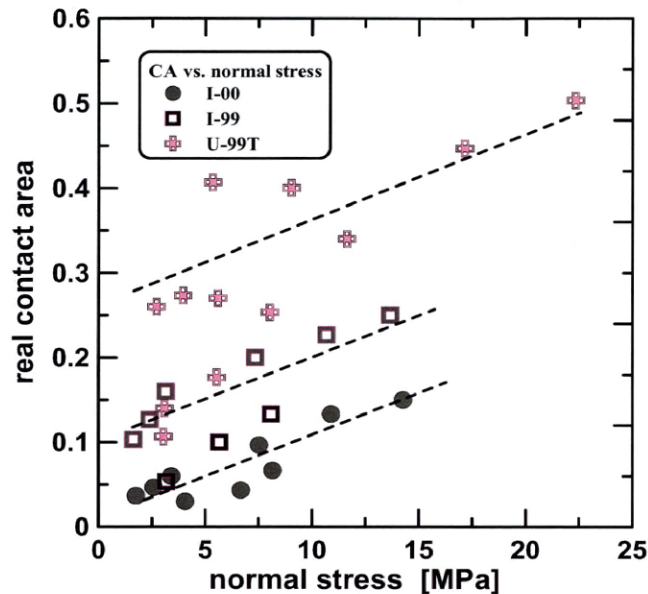
**Figure 5.13**   Real contact area plotted as a function of normal stress of samples I-00, I-99, and U-99T from three different friction tests:  flat die tribometer, bending under tension tribometer with 50.8 mm roller die diameter, and with 12.7 mm roller die diameter.

## 5.2  Formability Test, the Limiting Drawing Ratio

The limiting drawing ratio (LDR), determined from the Swift test described in Chapter 3, gives a measure of the formability of the steel sheet.  The LDR is directly related to normal anisotropy, the $\bar{r}$ value, where a high value of $\bar{r}$ value represents good drawability of the sheet.  In the drawing process, friction plays an important roll as an increase of COF increases the punch drawing force, reducing the LDR.  For the ISG sheets, coming from the same coil, the $\bar{r}$ values are very similar; therefore, the LDR values are expected to be the same.  Friction plays an important role in the Swift test, as an increase of the COF would represent in an increase of the punch drawing force and a lower LDR value.

Figure 5.14 presents the LDR values plotted as a function of the Fe content in the coating, and it can be observed that the LDR decreases with decreasing Fe content in the coating.  It has been shown that the COF increases with decreasing Fe content in the coating.  Figure 5.15 presents the same LDR data plotted as a function of the ζ-phase percent at the

surface of the coating.  By comparing samples among the same sheets, the coatings with lower amounts of ζ-phase, such as I-00, I-04, showed a higher LDR than samples I-92 and I-99.  Similarly, sample U-02T and A-15T showed higher LDR than U-99T and A-85T.  With the exception of a single point, there is a clear separation in the LDR response of the samples that were not temper rolled (ISG), and the samples that were temper rolled (USS and AK).  This behavior seems to correspond with the friction response of the sheets, where the samples with ζ-phase on the coating have higher COFs, and samples that were temper rolled also have higher COFs compared to the samples that were not temper rolled.  The variances of the LDR values is a direct response of the effect of the friction response of the sheets; for that reason, the LDR testing is referred to as an indirect friction test in which the effects of the different friction response is identified.
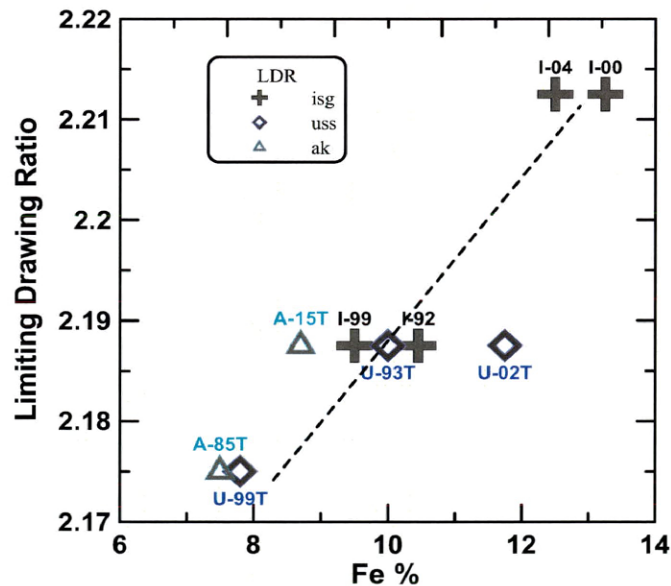


**Figure 5.14**     **Limiting drawing ratio values plotted as a function of the Fe content in the coating.**
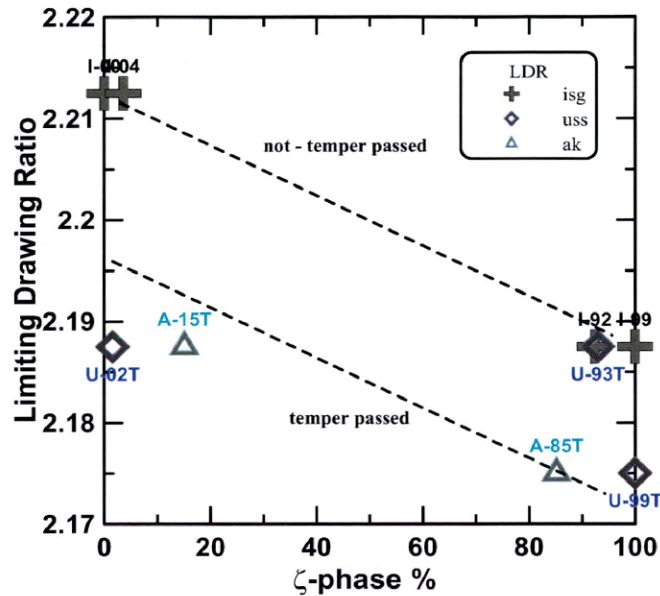
**Figure 5.15** Limiting drawing ratio values plotted as a function of the amount of $\zeta$-phase percent at surface of the coating.

It can be argued that the differences in LDR values are the result of different $\bar{r}$ values of the sheets; in other words, the different LDR values are a natural response of the anisotropy of each individual sample. In order for this to be correct, the LDR values would follow a reported trend where the LDR values increases with increasing $\bar{r}$ value [67]. Figure 5.16 shows the LDR values plotted with the $\bar{r}$ values for the ISG sheets, the only samples that came from the same coil, and therefore expected to have the same $\bar{r}$ value. What was found was that the LDR values decreases as the $\bar{r}$ increases, the opposite of what is expected if the LDR value was controlled by the anisotropy of the sheets. This finding confirms that the resulting LDR variations are a result of the friction response of the samples.

124
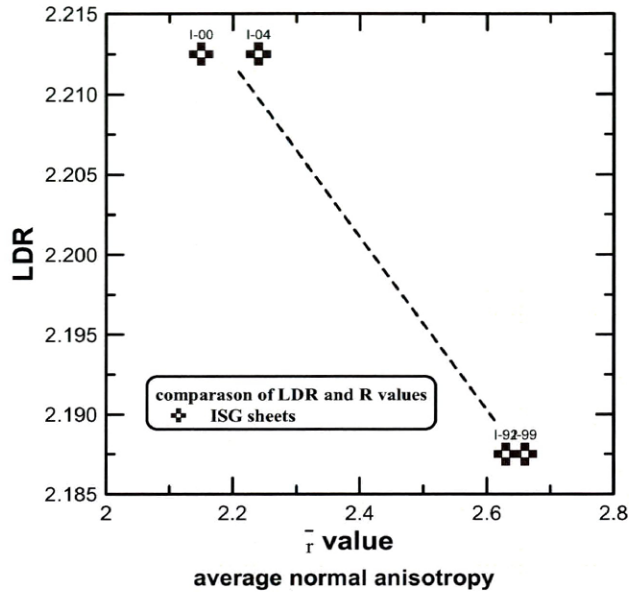
**Figure 5.16** Limiting drawing ratio values plotted with as a function of average normal anisotropy, $\bar{r}$, for the ISG samples.

## 5.3  Powdering Test

The adherence of the coating was tested with the double-Olsen powdering test, which is described in Chapter 3.  Figure 5.17 shows the metal loss from the double-Olsen powdering test as a function of the Fe content in the coating.  The metal loss decreases with increasing Fe content.  This observation that has been reported in literature [30,31,32,33,34,35,36,37,38].  The comparison between the different samples is valid because the coating masses (grams of coating per square meter) are similar.  However, plotting the metal loss of samples versus $\zeta$-phase percent on the surface of the coating as in Figure 5.18, does not show any clear trend, it appears that amount of $\zeta$-phase on the surface has no direct effect on the powdering response of the coatings.

It might be concluded from the previous observations that powdering is affected only by the Fe content in the coating and not by the amount of $\zeta$-phase in the coating.  In reality, there are several factors affecting the powder resistance of the coatings such as the thickness of the $\Gamma$-phase, the ratio of $\Gamma_2/\Gamma_1$ phases, grain size, and thickness of $\delta$-phase.  The

deformation imparted by the double-Olsen test to assess the adhesion of the coating, the bending and unbending, is not a common forming process path. A cautious approach should be taken when interpreting powdering test results as these might not be a true representation of a real situation; nevertheless they are a good guide to qualitatively compare different coatings and a test criterion for a material acceptance.
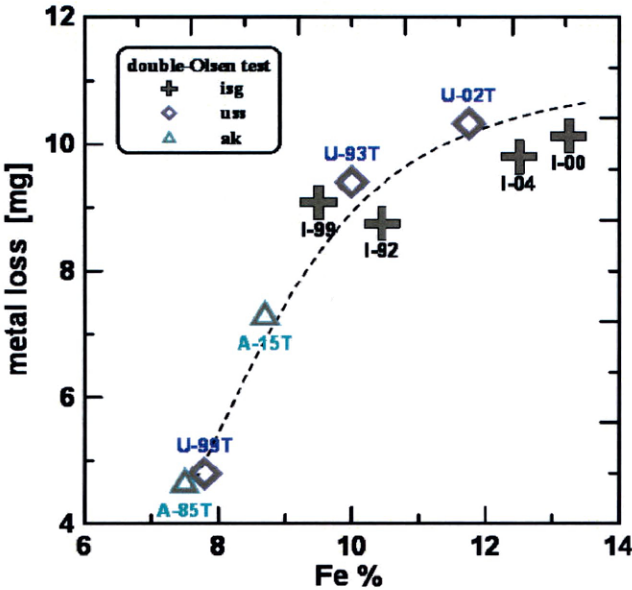


**Figure 5.17**    **Double-Olsen powdering test results plotted as a function of Fe content in the coating.**
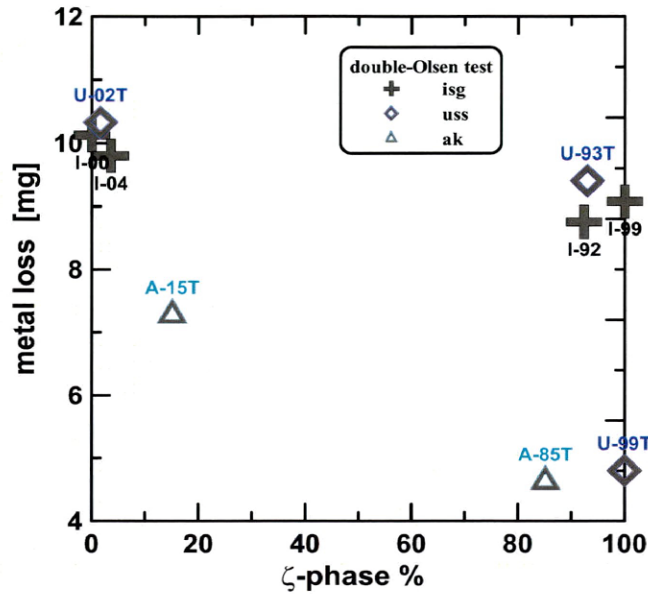
**Figure 5.18** Double-Olsen powdering test results plotted as a function of $\zeta$-phase percent at the surface of the coating.

The $\zeta$-phase plays an important roll controlling powdering in a forming process where there is contact with a die. It has been demonstrated in section 5.1.4 that the $\zeta$-phase at the surface of the coating increases the real contact area on a forming process (Figure 5.13). Assuming that the contact areas between the sheet and the forming die carry the bearing load, the smaller the real contact area the higher the normal stress would be. The real normal stress $\sigma_{N,real}$ can be calculated as follows:

$$\sigma_N = \frac{F}{A}$$

$$A_{real} = b * A$$

[ Eq. ] 5-1 $$\sigma_{N,real} = \frac{F}{A_{real}}, \text{ or } \sigma_{N,real} = \frac{F}{b * A}$$

where $F$ is the applied normal force, $A$ is the macroscopic contact area between the sheet and the forming die, $b$ is the fraction of the area that is in real contact with the die, and $A_{real}$ is the real contact area.

All the measured COF values ranged from 0.14-0.19, while the real contact area fractions range from 0.03-0.50. These variations in real contact area fraction represent significant differences in the calculated real normal stress. The shear stress $\tau$ is directly related to the normal stress in a friction situation, and the real shear stress $\tau_{real}$ could be estimated from the measured friction coefficient and the real contact area as follows:

Remembering that: $\mu = \dfrac{\tau}{\sigma_N}$

[ Eq. ] 5-2 $\qquad \mu = \dfrac{\tau_{real}}{\sigma_{N,real}}, \qquad \qquad \tau_{real} = \mu\sigma_{N,real}$

In the metallographic observations of cross section of the tested samples, some showed heavy damage in the form of powdering while others did not. Sample I-00 tested with the FDT with a medium-level clamping force is shown in Figure 5.19, where both sides of the sample are shown. The heavily damaged coating can be observed in the figure, some parts of it had been pulled out and there seems to be horizontal cracks running across the entire photographed area. The real contact area in this sample was 6.6 %. Considering that the FDT does not impart any bending, the damage to the coating is produced purely by the clamping forces and the frictional shear stress from the die. In previous studies in which the adhesion of GA coatings had been investigated, Hertveldt *et al.* reported a shear adhesive strength for the coating in the range of 10-20 MPa [68], while Nakamori *et al.* reported shear adhesive strength range of 6-10 MPa [69] for coatings similar to the ones used in this study. These values of shear strengths were obtained by performing a modified lap shear test. In Figure 5.19, the real normal stress calculated with [ Eq. ] 5-1, is 101 MPa, and the resulting real shear stress calculated with [ Eq. ] 5-2 is 13.8 MPa. The value of real shear stress is in the range of the adhesive strength presented in the literature.

In Figure 5.20, for sample I-00 tested with the BUTT -12.7 mm roller die diameter, the coating shows some damage. The BUTT produces bending and unbending, and with the 12.7 mm roller die diameter, the bending is quite pronounced. The damage of the coating is not as severe as in Figure 5.19. The value of calculated real shear stress for this sample is 9.9

128

MPa, close to the reported shear strength. In Figure 5.21, sample I-00 tested on the BUTT - 50.8mm roller die diameter is shown. This sample, although having the highest Fe content of all the coatings and having no $\zeta$-phase at the surface, did not exhibit significant powdering damage. The calculated real shear stress is quite low with a value of 2.8 MPa. The absence of powdering damage in this coating is a result of the real contact area that produces low real shear stress. The last example, Figure 5.22, sample I-99 tested with the FDT at a medium-level normal stress, shows no powdering damage at the coating contact point. Even though sample I-99 had a relatively high value of metal loss in the double-Olsen powdering test, the increase in contact area produced by the $\zeta$-phase of the coating results in a low value of the real shear stress, below the shear strength reported in literature.

Several researchers have stated that when the $\zeta$-phase is present in the coating, it improves the powdering resistance [38,70,71]. The mechanism of powdering improvement of the $\zeta$-phase proposed in this dissertation is that the $\zeta$-phase increases the real contact area accommodating more of the normal load which decreases the real normal stress. This increase in real contact area also results in a diminution of the real shear stress, which protects the coating from damage. While the presence of the $\zeta$-phase increases the shear stress by increasing the COF, the increase of real contact area dominates, reducing the real stresses and minimizing powdering.

real contact area = 6.6 %

applied normal stress = 6.6 MPa

real normal stress = 101.0 MPa

real shear stress = 13.8 MPa
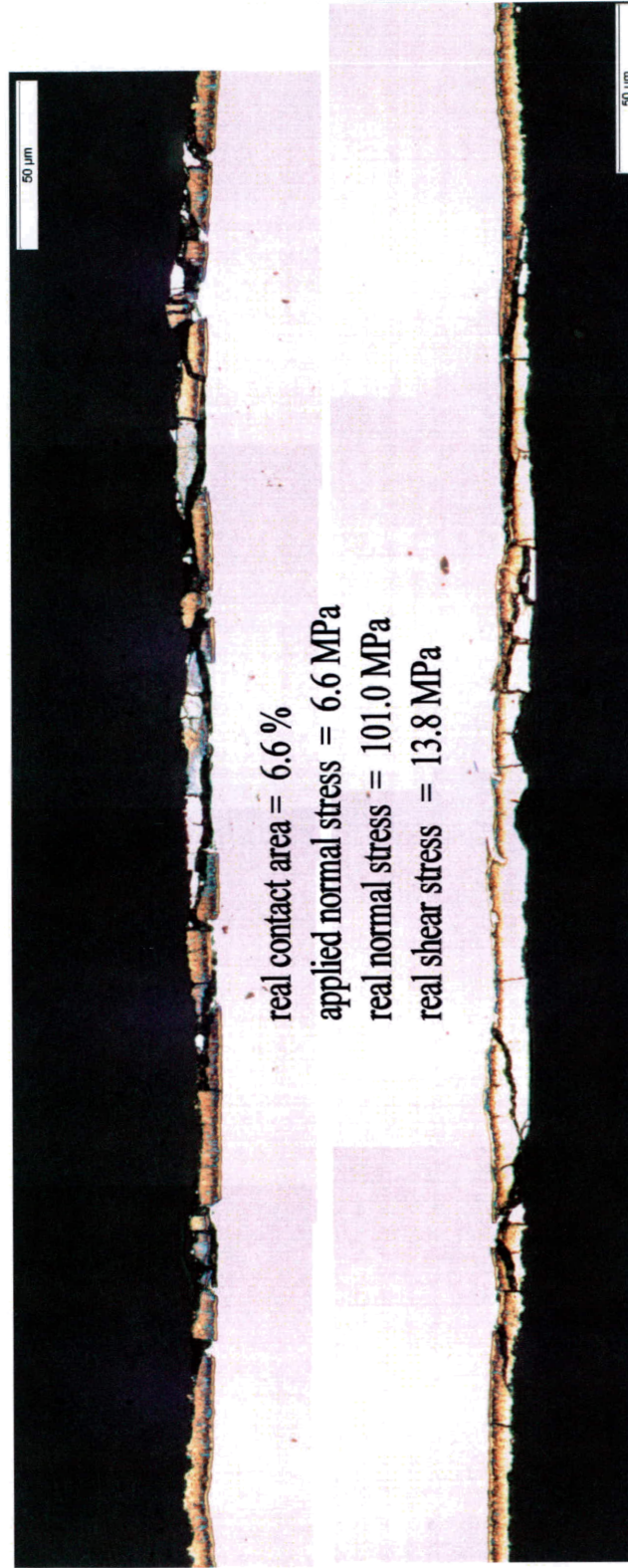
**Figure 5.19**     Light optical micrograph of flat die tribometer tested sample I-00, showing the coating damage of both surface sides.  NOTE: the center part of the substrate is not in scale.  Etched with Kilpatrick solution.

130

real contact area = 20 %

applied normal stress = 11.4 MPa

real normal stress = 60.5 MPa

real shear stress = 9.9 MPa
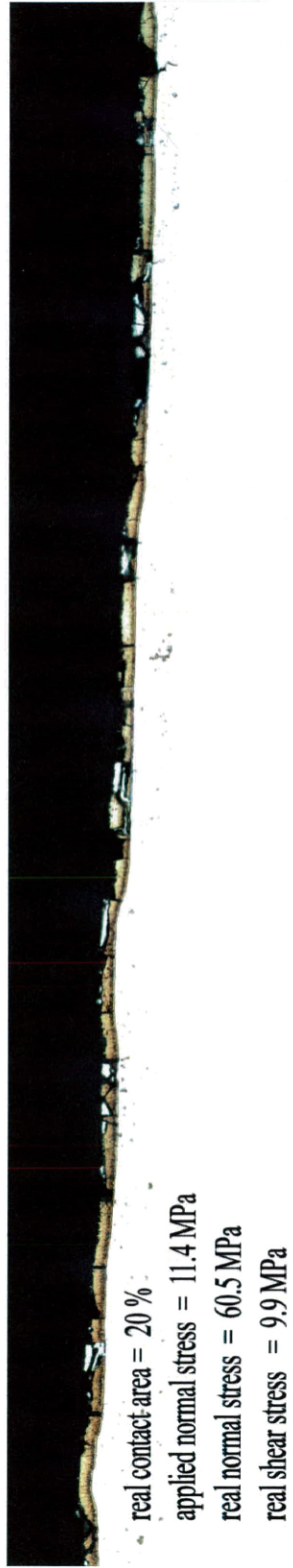
Figure 5.20    Light optical micrograph of bending under tension tribometer -12.7 mm roller die diameter tested sample I-00, showing the coating damage of the surface side in contact.  Etched with Kilpatrick etching solution.

real contact area = 8.3 %

applied normal stress = 1.4 MPa

real normal stress = 17.6 MPa

real shear stress = 2.8 MPa
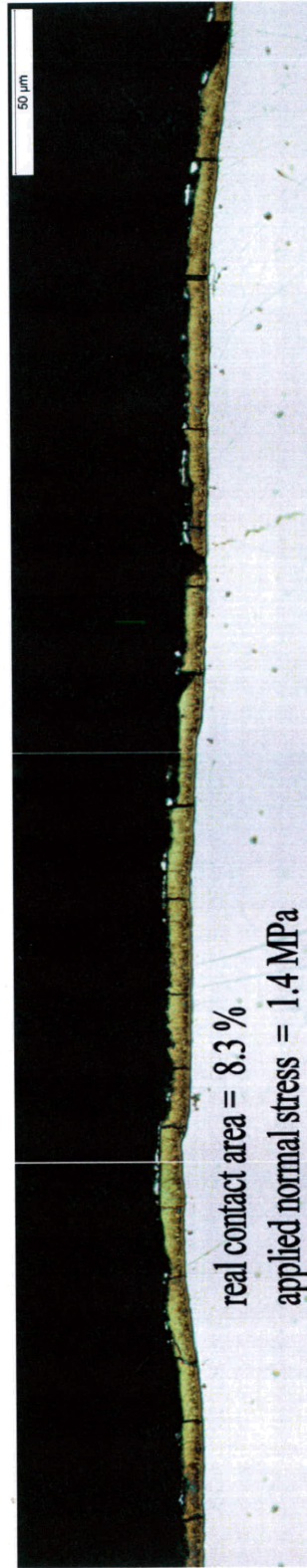
**Figure 5.21** Light optical micrograph of bending under tension tribometer -50.8 mm roller die diameter tested sample I-00, showing the coating damage of the surface side in contact. Etched with Kilpatrick etching solution.

real contact area = 14.2 %

applied normal stress = 5.6 MPa

real normal stress = 39.8 MPa

real shear stress = 6.1 MPa
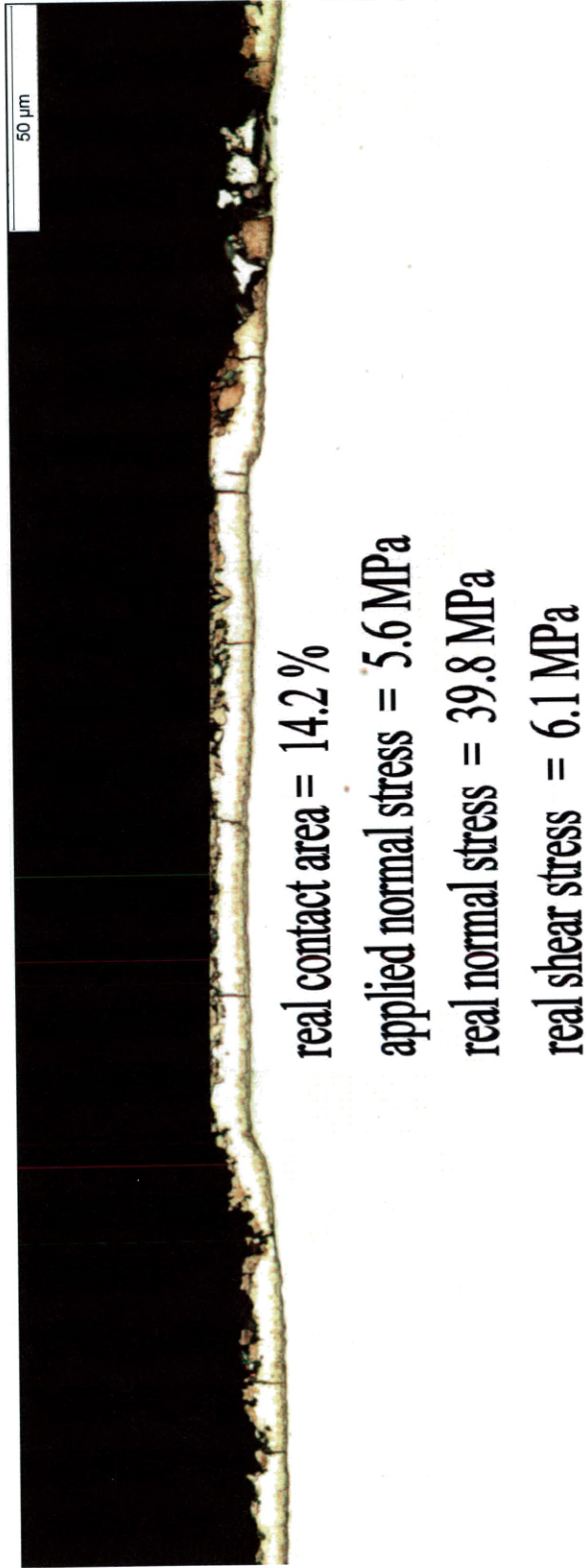
**Figure 5.22**   Light optical micrograph of flat die tribometer tested sample I-99, showing the coating damage of both surface sides.  Etched with Kilpatrick etching solution

# CHAPTER 6

# MIXED FILM LUBRICATION FRICTION MODEL

The tribological behavior of the galvannealed (GA) coatings can be described with a mixed film lubrication (MFL) friction model. This chapter gives an introduction to the lubrications regimes, describes the MFL friction model, and demonstrates how the experimental data match the model. The MFL friction model accommodates results from previous studies, as well as justifies the findings of other researchers. At the end the limitations of the model are discussed.

## 6.1 Fluid Film Lubrication

There are different ways two sliding solid surfaces in contact with each other can be characterized. If the surfaces are clean it results in high coefficients of friction (COF), wear, and partial fusion between the two. Lubricants are intentionally added to protect the surfaces, prevent wear, and lower the COF. Lubrication can be applied in two ways, either by solid lubrication and by fluid (liquid or gaseous) film lubrication. A thin film, on the order of the surface roughness of the surfaces in contact, results in low COF and wear, as compared to solid-solid contact. A thick fluid film prevents solid-solid contact and lowers the COF and the amount of wear is negligible. There are different lubrication regimes between the solid-solid contact and the thick film in between surfaces.

The lubricant film parameter is defined as:

**[ Eq. ] 6-1**    $$\Lambda = \frac{h}{\sigma^*}$$

where $h$ is the lubricant film thickness, and $\sigma^*$ is the composite standard deviation of the surfaces roughness, which is calculated in the following way:

[ Eq. ] 6-2 $\qquad \sigma^* = \sqrt{\sigma_1^2 + \sigma_2^2}$ or $\sigma^* = \sqrt{R_{q,1}^2 + R_{q,2}^2}$

where $\sigma_1$ and $\sigma_2$ are the standard deviations of the profiles of the two surfaces, and $R_{q,1}$ is the root means square roughness value of the work piece and $R_{q,2}$ is the root means swquare roughness value of the tooling. As described earlier, the standard deviation of the profile of the surface is comparable to the $R_q$ roughness value.

The Stribeck curve, shown in Figure 6.1, is a hypothetical representation of a fluid lubricated bearing system in which the response of the COF is plotted as a function of a dimensionless parameter, called the Stribeck's number:

[ Eq. ] 6-3 $\qquad$ Stribeck's number $= \eta \dfrac{N}{P}$

where η is the absolute viscosity, N is the speed of the bearing in revolutions per second, and P is the load divided by the projected bearing area or the pressure. The different lubrication regimes can be observed in the Stribeck curve. The hydrodynamic lubrication (HDL), also called fluid-film or thick-film lubrication, occurs when the lubricant film parameter $\Lambda > 6$. Hydrodynamic lubrication is often referred to as ideal lubricated contact condition, where there is absolutely no contact between the surfaces, there is no adhesive wear occurring, and the COF are as low as 0.001. Hydrodynamic lubrication is one of the most studied regimes, and fluids mechanics is used to described the behavior of the films. Elastohydrodynamic lubrication (EHL) regime is a subsection of HDL in which the elastic deformation of the surfaces in contact is considered. The bearing load is still carried by the fluid film. For the EHL regime the lubricant film parameters $\Lambda$ is between 3 and 10. An even more specific subsection of HDL is plastohydrodynamic (PHD) where extreme high pressures plastically deform one of the surfaces without actual contact of the surfaces, *i.e.* in metal rolling [72,73,48,74].

Boundary lubrication is a term used when the surfaces are close together, and the lubricant film parameter is $\Lambda$ is less than 1. In this lubrication regime, the surface interaction between monomolecular or multimolecular films of the lubricant and the solid asperities dominate the contact. Fein defines boundary lubrication as "a condition of lubrication in

136

which friction and wear between two surfaces in relative motion are determined by the properties of the surfaces and by the properties of the lubricant other than bulk viscosity" [74]. The COF has values above 0.10 or much higher. Physisorbed or chemisorbed or chemically reacted films can prevent adhesion. The failure in boundary lubrication occurs by adhesive and chemical bonding, wear, although some welding between the surfaces is known to occur, especially in metalworking processes [72,73,74].

The transition between the hydrodynamic lubrication and the boundary lubrication regime is called mixed lubrication or mixed film lubrication (MFL). In this regime two lubrication mechanisms may be functioning, there is frequent solid contact between the surfaces, but there is still a portion of the bearing load supported by the hydrodynamic film. The solid contact between the asperities can produce adhesion, metal transfer, wear, plastic deformation, and particle formation. As in boundary lubrication, adhesion is prevented by physisorbed, chemisorbed or chemically reacted films.

137
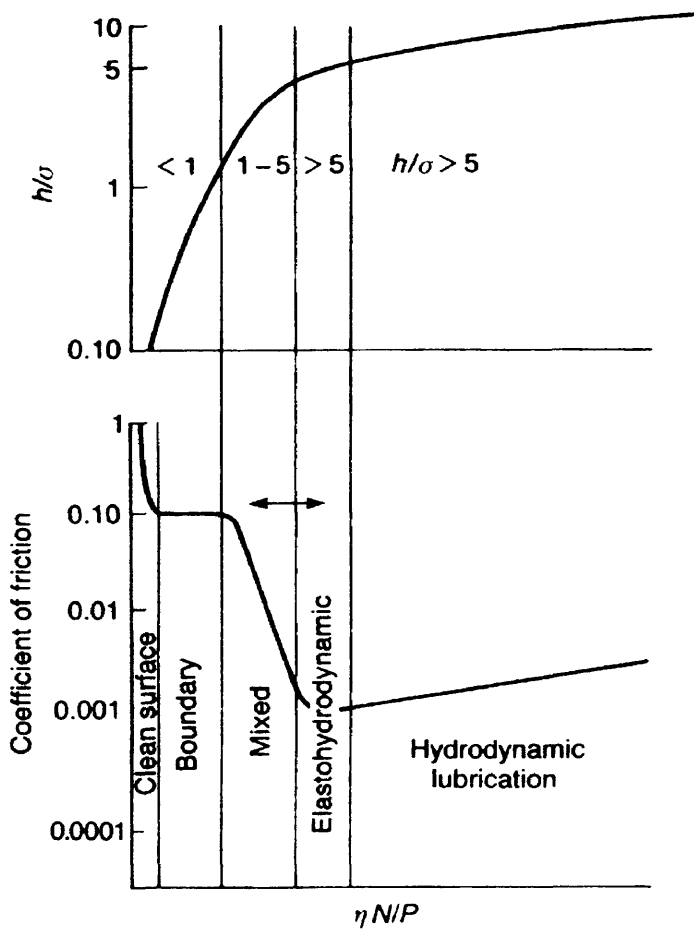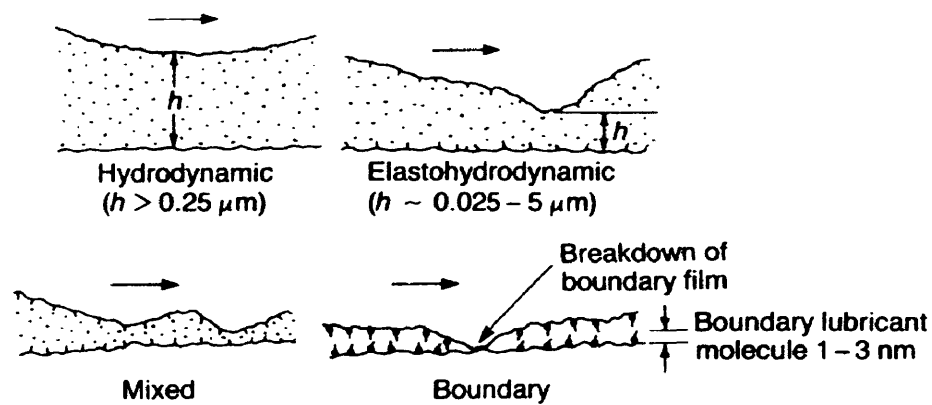
**Figure 6.1**   **Lubricant film parameter (h/σ) and coefficient of friction as a function of ηN/P (Stribeck curve) showing different lubrication regimes observed in fluid lubrication.72**

## 6.2 Mixed Films Lubrication Friction Model

Mixed films lubrication is the transitional regime between boundary and hydrodynamic/elastohydodynamic lubrication. Following a similar analysis to the one presented by Schey [48], a friction model can be developed for the GA coated steels under investigation. Figure 6.2 presents a cross-section diagram of the two surfaces in contact, the surface fraction areas lubricated with the fluid film are identified by $h$, the fraction areas that are subjected to a boundary lubrication regime are identified by $b$, and the fraction areas marked as $c$ are in dry contact. The contact between the die and the different other interfaces (fluid film, boundary, and dry interface) produce different shear force reactions when experiment a sliding motion. From a force balance at the interface and knowing the area fractions of the different interfaces, the average shear strength of the interface of the mixed film can be expresses as the sum of the shear strengths of those areas:

[ Eq. ] 6-4 $\qquad \tau_{mix} = h\tau_h + b\tau_b + c\tau_c$

where $\tau_h$ is the shear strength of the hydrodynamic film, $\tau_b$ is the shear strength of the boundary film, and $\tau_c$ is the shear strength of the areas in dry contact. In real life, the COF is measured instead of shear stresses. The friction in hydrodynamic pockets can be expressed as $\mu_h$, the friction produced by the boundary areas can be expressed as $\mu_b$, and the friction caused by the dry pockets can be expressed as $\mu_c$. Then the behavior of the interface can be described as:

[ Eq. ] 6-5 $\qquad \mu_{mix} = h\mu_h + b\mu_b + c\mu_c$

If, over some fraction of the surface $a$, contact results in actual metal pick-up, $\tau_a = k$, where $k$ is the shear strength of the softer surface in contact. The COF of the interface can be expresses as:

[ Eq. ] 6-6 $\qquad \mu_{mix} = h\mu_h + b\mu_b + c\mu_c + a\left( k \Big/ p \right)$
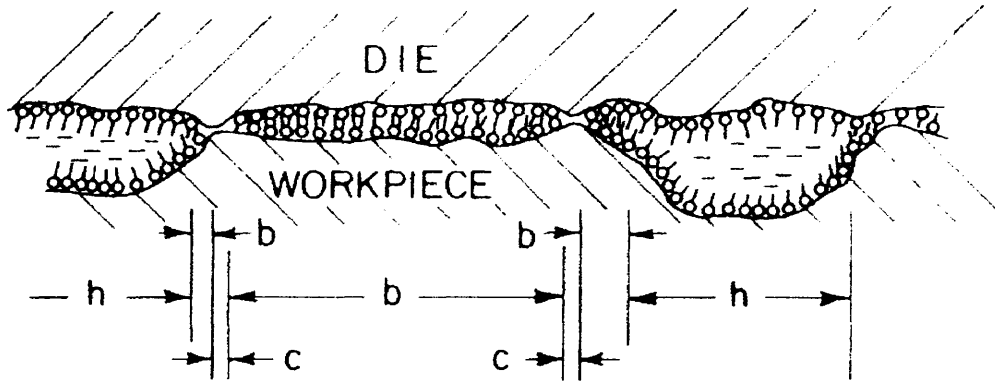
**Figure 6.2**  **Mixed film lubrication diagram. Interface between contacting surfaces.48**

In normal circumstances, $\mu_h$ could be calculated with hydrodynamic theory. In the present study the roughness of the coatings does not allow for a simple calculation. The fraction $a$ in reality is very small; however, it is always present because there is evidence in the forming dies of pick-up. To simplify the problem, the contribution to friction of the dry lubrication, boundary, and pick-up can be combined in one term, $\mu_b$, and $(\,b\,+\,c\,)$ can be expressed only as $b$, the real contact area. The mechanisms are interconnected to form a surface that is subject to a boundary lubrication regime. The asperities are flattened, which occurs in a dry lubrication regime, producing pick-up of the die. The simplified expression becomes:

| Eq. | 6-7        $$\mu_{mix} = b\mu_b + (1 - b)\mu_h$$

## 6.3 Application of the Mixed Films Lubrication Model to the Experimental Data.

It has been demonstrated that the friction experimental data follow a common behavior, and the real contact area increases with applied normal stress, independent of testing method. The coatings with $\zeta$-phase at the surface showed higher real contact areas than samples with little or no $\zeta$-phase. These coatings with $\zeta$-phase have higher values of COF. When the COF is plotted as a function of the real contact area for the ISG samples, the

140

COF consistently increases as the real contact area increases, Figure 6.3. In this figure the single test data have been selected together with the single real contact area measurements, resulting in the scatter of the data points. The COFs for every point were calculated from the ratio of the shear stress and the normal stress for each individual test, using the Coubrough method for the BUTT data, described in Chapter 3. A linear regression calculated from the data points shows a fair fit.
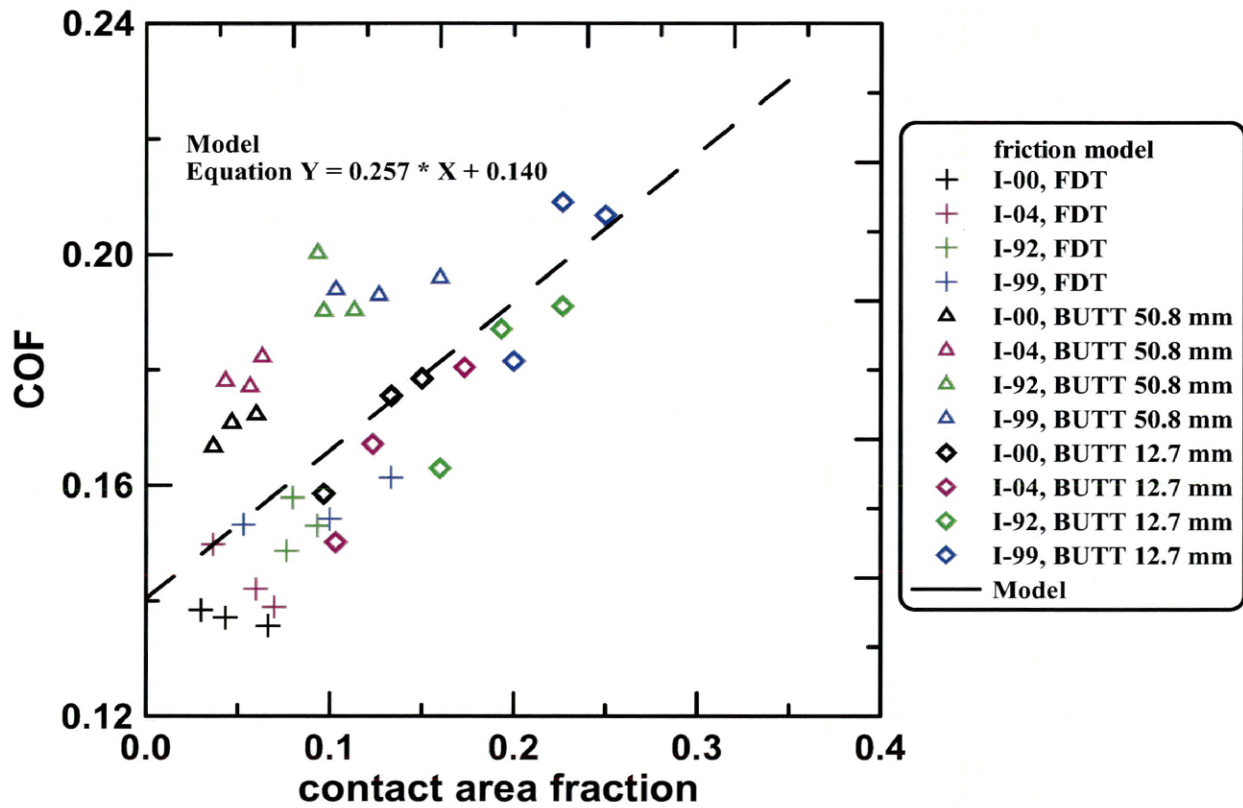


**Figure 6.3**  **Coefficients of friction plotted as a function of the real contact area for the ISG samples.**

With simple arithmetic manipulation it can be shown that [ Eq. ] 6-7 takes the form of:

$$[ \textbf{ Eq. } ] \textbf{ 6-8 } \qquad \mu_{mix} = (\mu_b - \mu_h)b + \mu_h$$

From the results from out linear regression, *Y=0.257\*X + 0.140*, the intercept represents $\mu_h$, which has a value of $\mu_h$=*0.140*. The slope of the linear regression represents ($\mu_b$-$\mu_h$), from which the value of the boundary coefficient of friction can be extracted, $\mu_b$=*0.397*.

Applying the same treatment to the USS sheets shown in Figure 6.4, a fair fit can be observed as well. The values resulting from the linear regression are some what different. The resulting value of the hydrodynamic COF $\mu_h$=*0.135*, somewhat similar to what found with the ISG sheets, but the resulting boundary COF $\mu_b$=*0.236* is significantly lower.
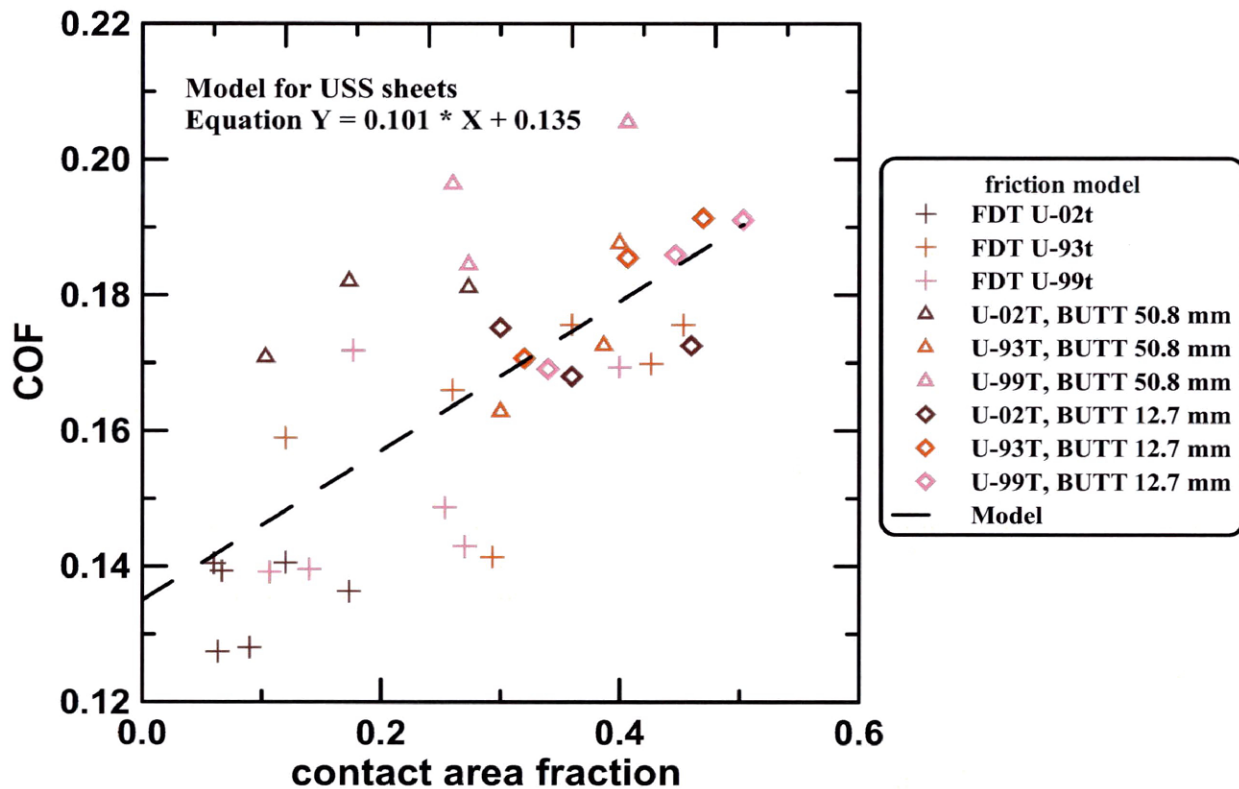


**Figure 6.4**     **coefficients of friction plotted as a function of the real contact area for the USS samples.**

One of the first obstacles of the model is the discrepancy between the results from the two families of data. The COFs calculated for both families of samples, are considered an accurate measure. However, the contact area measurements because of the pre-testing condition of the USS sheets are not as accurate. Because of the temper roll, these coatings already had a surface condition where some asperities had been flattened prior testing. The 3D profiles for the contact areas for the samples that were tested at low normal stress levels, showed two distributions prior testing and distributions after testing. Figure 6.5 shows an example of a profile with three distributions. The inverse slope of the probability plot represents the standard deviation of the distribution which can be related to the $R_q$ value, and in the figure at about 70 % the slope of the distribution changes. This change indicates the start of the distribution caused by the temper roll, and the number agrees with the observations performed with scanning electron microscope secondary electron (SEM-SE) images. The third distribution with an even steeper slope (or a smaller $R_q$ value) represents the fraction of area affected by the friction testing, meaning that only a fraction of the already flattened surface was making contact with the die during the friction testing. The COF and real contact areas agree with what was found in the ISG samples. On the other hand, for USS and AK samples that were tested at higher normal stresses which would result in more deformation, the contact area measurements performed by analysis of the probability plots of the 3D profiles resulted in fractions higher than the original temper rolled flattened areas. Observations of the SEM-SE images confirmed these values as well. It is clear that the deformation of the asperities that occurred during the friction testing resulted in an increase of the flattened area fraction, but it is possible that not all this measured area fraction was in contact with the die, acting as in the boundary lubrication regime. It is possible that some of the fraction of real contact area measured is acting and contributing to the friction coefficient in a boundary lubrication regime, while another fraction of the measure real contact area is acting in a elastohydrodynamic regime. Attempting to differentiate between the two cases by analyzing the distributions, even by observations of the SE-images, is a very difficult task. If that was the case, measured real contact areas higher than the preexisting flat fraction caused by the temper roll represent only a fraction of the true real contact area acting in a boundary

lubrication regime, the data points in Figure 6.4 that have a real contact area higher than the original temper rolled value of 0.25, would had been displaced to the right by certain amount. Repositioning of these points would adjust the slope of the regression to a higher value bringing it to agreement with what found for ISG sheets. Figure 6.6 attempts to illustrate the adjustment. For these reasons, the values obtained from the linear regression of the ISG samples will be the ones considered for the concluding statements of this study.
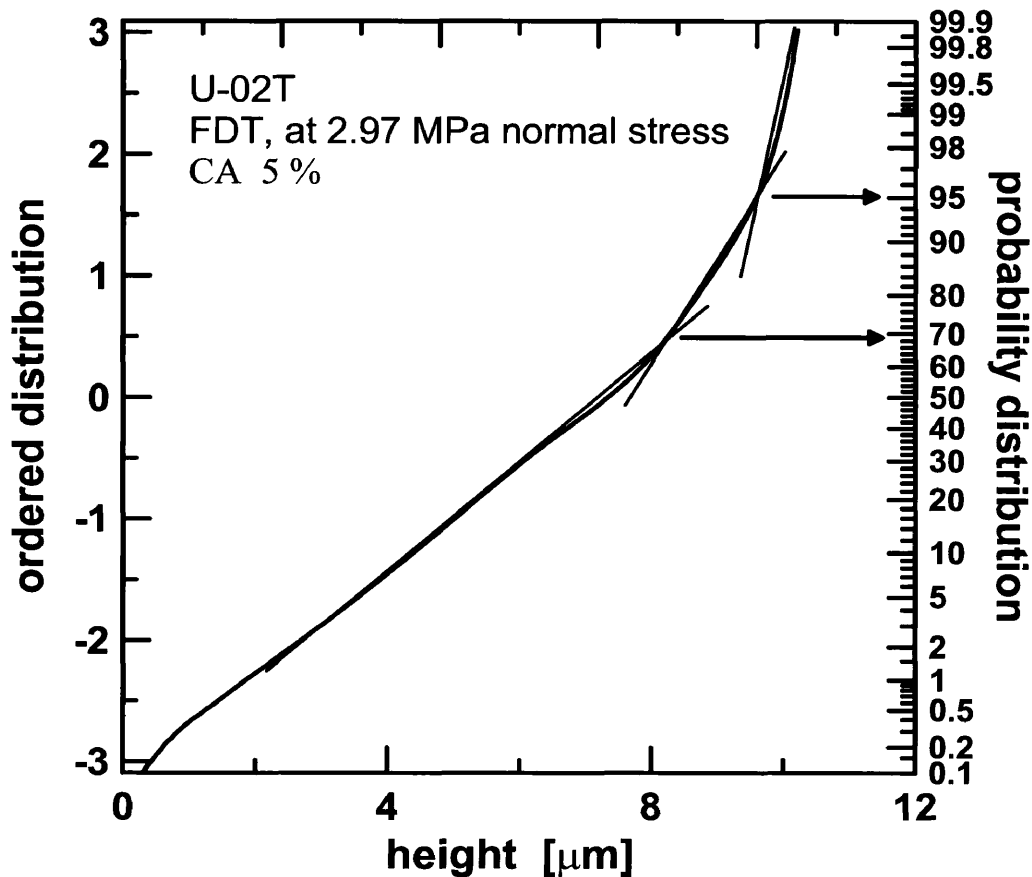


**Figure 6.5**     **Probability plot for flat die tribometer sample U-02T, tested at 2.97 MPa. This figure shows two contact area distributions, one corresponds to the temper rolled, the other is the effect of the friction testing.**

144
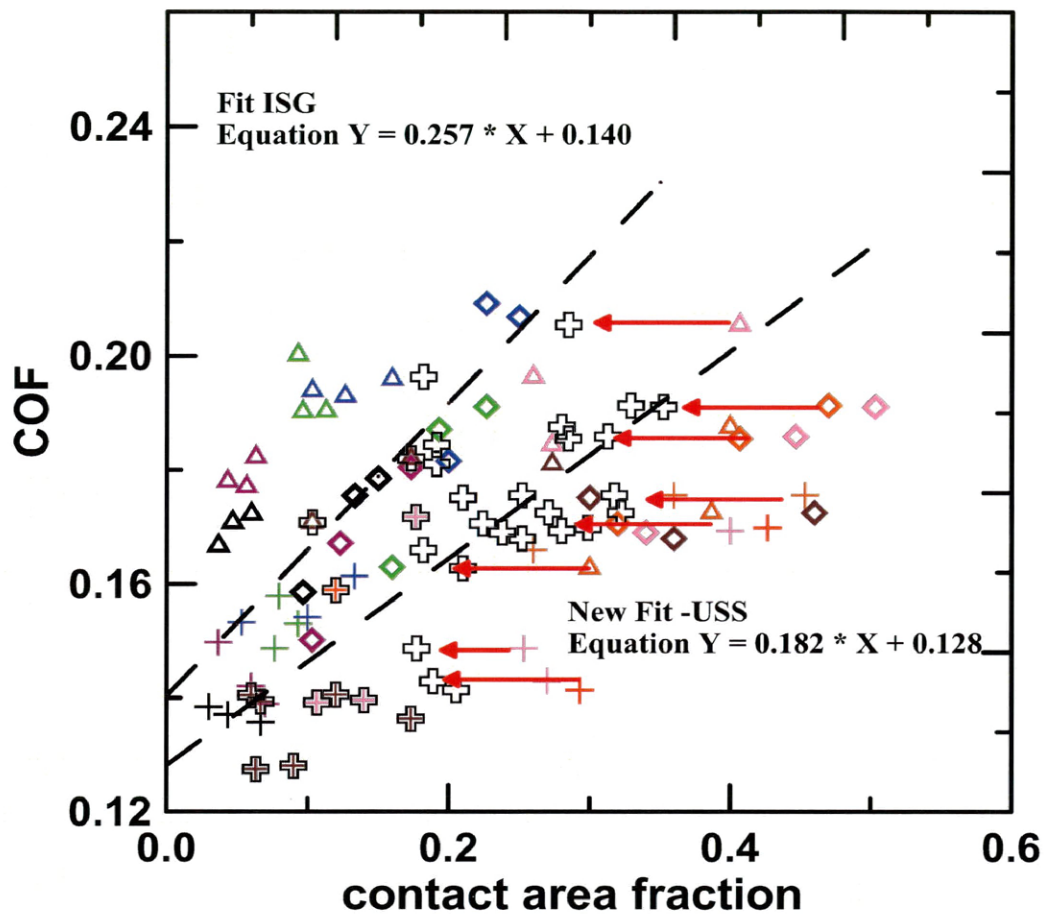
**Figure 6.6**  Coefficients of friction plotted as a function of the real contact area for the ISG and USS samples. The data points of the USS samples that showed a contact area higher than 0.25, the temper rolled contact area fraction, are projected to the right, and the resultant linear fit.

The complicated nature of the scratch test does not allow the resulted data to be included it in the model; however, we can compare the values and see how they fit with the model. In Figure 6.7, the values of COF for the scratch test are plotted with the rest of the data. The values for the contact are fraction of the scratch test samples were estimated from observations of images of the tested samples surfaces. Extrapolating the model predictions, the scratch test data points fall in the range projected by the two families of data.
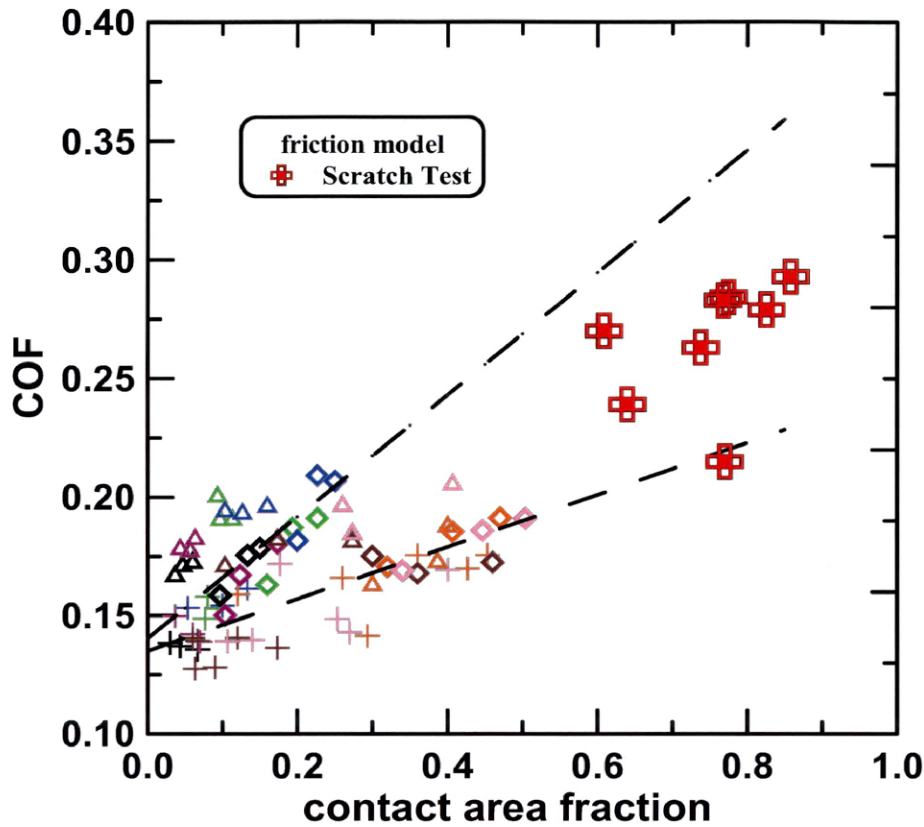
**Figure 6.7**    COF plotted vs. real contact area fraction with scratch test results.

In the past, there had been various other studies on friction of GA coatings using the same lubricant as in this study. Vallance studied the friction behavior of the coated steel sheets using the BUTT [75], and Gallo studied the friction and formability of GA IF-steel sheets [76]. The results of those studies are plotted in Figure 6.8, where the COF for the BUTT had been plotted now using the Vallance and Matlock procedure, since in the previous studies that was the procedure followed to measure the COF. One can observe a fair match between the previous data and the results from this study.
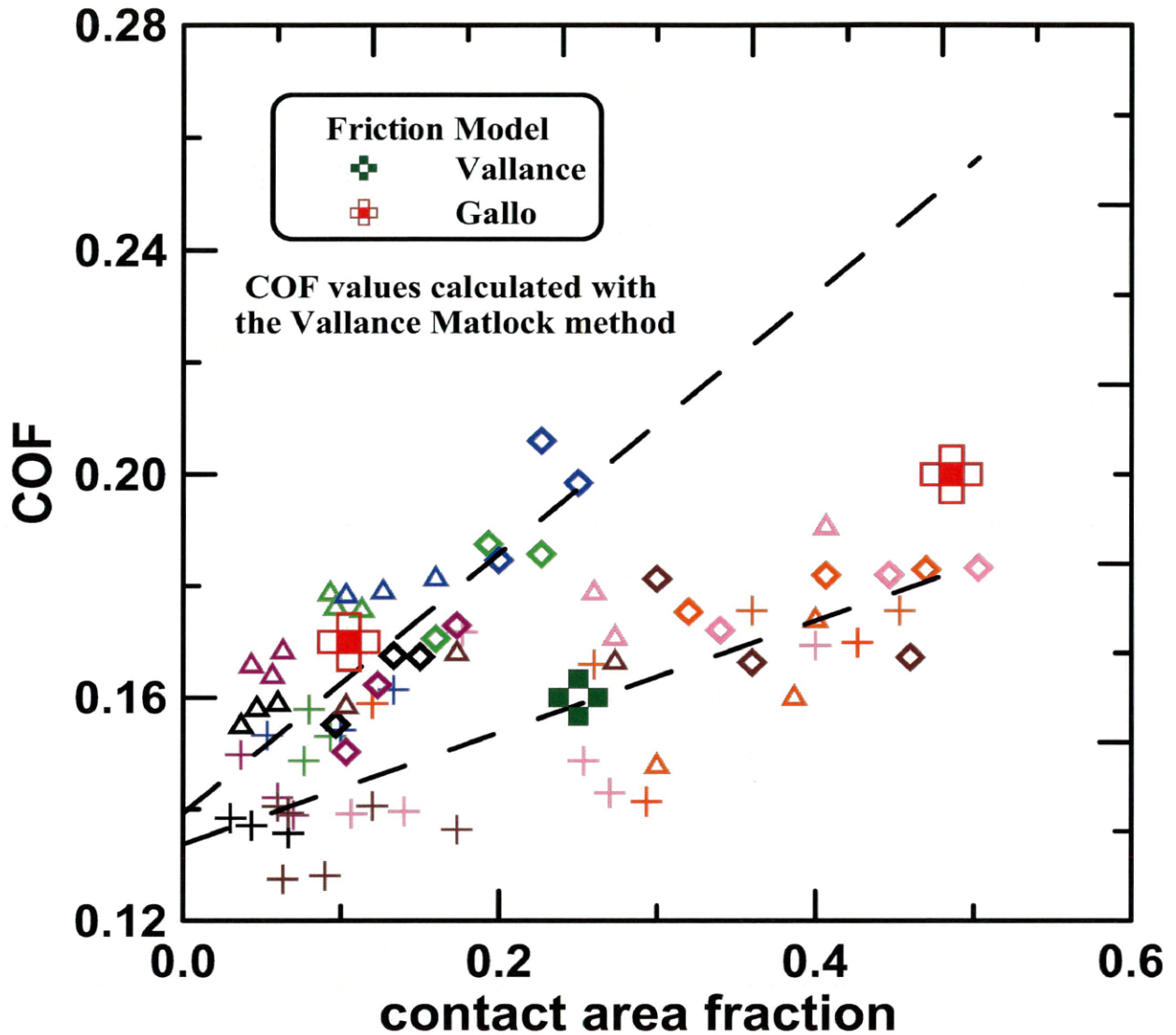
**Figure 6.8**      **Mixed films lubrication model compare with previous studies.**

## 6.4 Mixed Films Lubrication Model Implications

It was proven that the experimental data could be explained with the use of a MFL model. There are two clear characteristics that the MFL model is valid, the lubricant film parameter and the surface of the tested samples appearance. In the worst cases, the height of the fluid films can be estimated as half of the $R_z$ roughness value (the average of the 10

highest points minus the average of the 10 lowest points of the 3D profile), that for the as received sample I-99 (the sample with the highest roughness values) is $R_z/2=10$ μm. The $R_q$ value for that same sample is 3.51 μm, and the roughness of the BUTT roller die is 0.25 μm. From [ Eq. ] 6-1 and [ Eq. ] 6-2 the value of the lubricant film parameter is:

$$\Lambda = \frac{h}{\sigma^*}, \qquad \Lambda = \frac{10}{\left(3.51^2 + 0.25^2\right)^{\frac{1}{2}}} = 2.84$$

The value of the calculated lubricant film parameter is exactly in the range of values expected for a mixed films lubrication regime. Figure 6.9 presents one example of a tested coating, where it can be observed that the real contact area consists of a fraction of the whole surface and the rest consist of load bearing fluid pockets.

In the development of the model, it was assumed that uniform contact existed between the die and the coating, without considering that the surface of the coating consists of two different phases with different mechanical properties and crystal structures. GD-QDP profiles showed evidence of the presence of oxygen at the surface of the coating. Taira *et al.* had confirmed and measured the thickness of the oxide layer (~10 nm) using Auger electron spectroscopy analysis [59]. The common behavior of increasing COF with increasing contact area, independently of the intermetallic phases present at the surface (δ or ζ-phase), confirms that the sliding system consist of a die in contact with an oxide layer. The ζ-phase plays the role of deforming underneath the oxide layer, accommodating the normal stress, increasing the contact area, resulting in an increase of the COF.
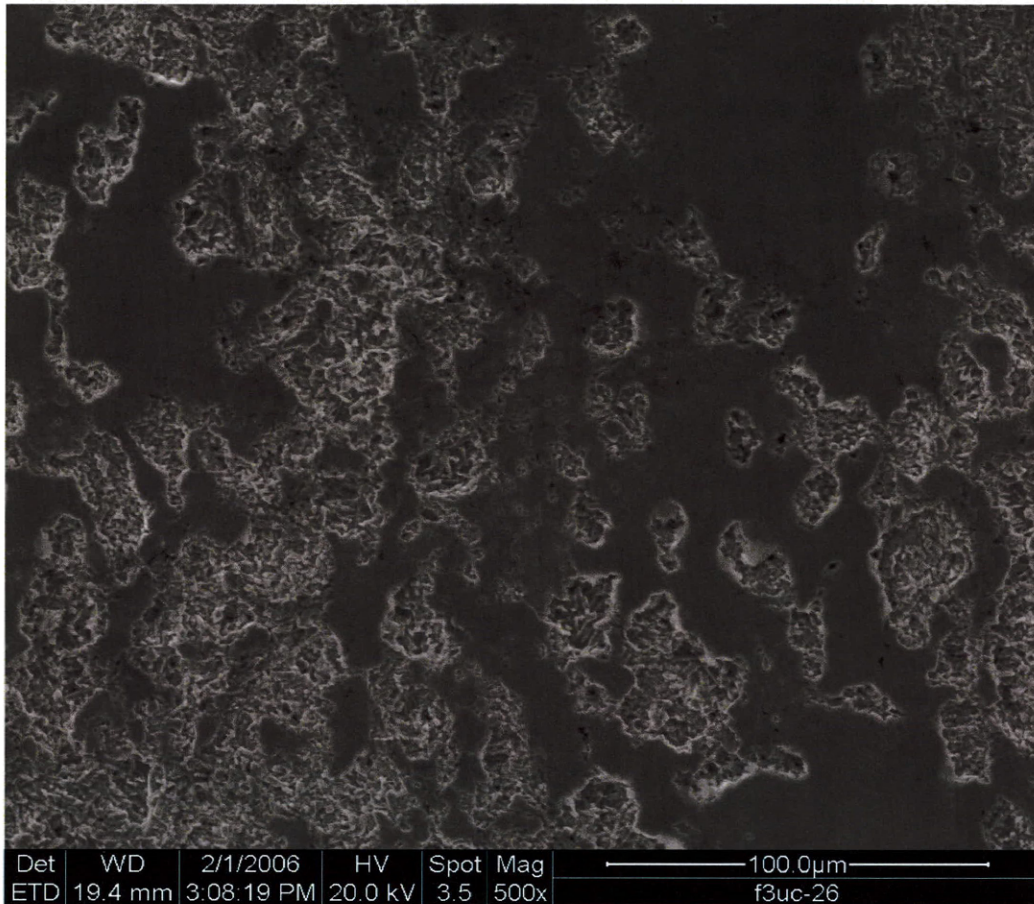
**Figure 6.9**  **Scanning electron microscope SE-image of flat die tribometer sample U-99T. The figure shows the surface of the tested sample, with the flattened contact areas and the fluid film pockets.**

Another implicit assumption of the model is that the real contact area is constant throughout the entire contact. Observations of the surfaces at the entry and exit of the contact areas of the sample with the die showed that the fractions of real contact area are similar. When the sample first comes in contact with the die, the high asperities deform accordingly to the normal stress applied and remain that way throughout the contact duration. The BUTT has been described as having a pressure profile with pressure peaks at the entrance and exit of the sample. The first pressure peak stress would create the initial asperity deformation and remain constant during the contact with the roller.

The effects of the difference in mechanical properties and crystal structures between the phases at the surface, is still an issue. When $\zeta$-phase deforms in contact, there is some energy consumed by the deformation, and the adhesion and pick-up of the die is higher than if the die were in contact with the $\delta$-phase. However, these factors seem to be small enough that the model still remains valid, showing no difference in the COF for a given real contact area, regardless of which phases are present on the surface.

The value of boundary lubrication COF, $\mu_b=0.397$, is a value somewhat higher than that reported in by others [48] but the calculations in those studies are considering contact between two hard surfaces. The value of $\mu_b=0.397$ is considered to be a good prediction. For the hydrodynamic COF, $\mu_h=0.140$, a smaller number at least one order of magnitude was expected from what was observed. Every sample in the experimentation showed some fraction of real contact area, which means that we do not have a direct measure for the hydrodynamic COF.

From the contact area measurements, the real contact area fractions ($b$) are accurate measures. However, the MFL model assumes that the rest of the fraction ($1-b$) is subjected to a HDL regime. Some portion of the HDL region ($1-b$) consists of interconnected areas that act as channels liberating hydraulic pressure and do not bear any load, not contributing to the hydrodynamic COF. Some portion ($1-b$) is composed of pockets that contain the lubricant, contribute to the bearing load, and have an effect in the frictional response. With the real measure of lubricant containing pockets, the real ratio of real contact areas to lubricant pockets could be known, resulting in a more accurate model. However, the measurement of the lubricant containing pockets is not a simple task.

The MFL friction model is still considered valid, even with the limitations described above. The value of the hydrodynamic COF, $\mu_h=0.140$, cannot be taken as an accurate measurement, but instead is considered as empirical result of our modeling without the normal physical meaning. If the model is limited to a minimum real contact area, the model is still successful in predicting the COF with real contact area. The boundary lubrication COF, $\mu_b=0.397$, is considered a good estimate.

150

## 6.5 Summary

In this chapter, a model that describes the frictional response of a GA coated steel sheet was developed. The model is based on mixed films lubrication regime and makes the COF a function of the real contact area. The experimental system agrees with the requirements of a mixed films lubrication friction model. The experimental data show agreement with the model, especially the ISG sheets where the measurements of real contact area are accurate. Some limitations of the model were discussed, where the measured numbers do not show a real physical significance. However, the model is considered valid as it successfully predicts the COF for a given contact area.

# CHAPTER 7
# CONCLUSIONS

The coefficient of friction (COF) is a critical parameter in metal forming. The friction response of seven galvannealed (GA) steel sheets with different intermetallic phase distributions was investigated. The friction testing and analysis of the tested samples produced different results. Some of these results agreed with those reported in literature, and some results produced new interpretations of the friction and powdering behaviors of the GA coatings. This chapter presents the summary of the conclusions drawn from this study.

Two different friction tests, the flat die tribometer (FDT) and the bending under tension tribometer (BUTT) were performed on the GA coatings. Two roller die diameters were used with the BUTT, 50.8 mm and 12.7 mm. The results of the friction testing can be summarized as follows:

- The COF increased as the Fe content in the coating decreased.
- The COF increased with the amount of $\zeta$-phase present on the coating.
- Coatings that were temper rolled and had a preexisting contact area surface texture resulted in higher COF, especially for the coatings containing $\zeta$-phase on the surface.

The surface of the tested samples was characterized. The real contact area of the tested samples was quantified. These observations are summarized in the following statements:

- The real contact area increased as the applied normal stress increased for each individual coating, independently of the type of friction test performed
- The increased of real contact area was larger for $\zeta$-phase containing coatings.
- The COF increased as the real contact are of the tested samples increased, independent of the coating (phase distributions) and type of friction test performed.

The mixed film lubrication (MFL) friction model describes the behavior of COF and real contact area. The experimental data were compared to the MFL model. A reasonable value for the boundary lubrication COF was found, $\mu_b=0.397$. The MFL model did not predict a value of elastohydrodynamic/plastohydodynamic COF within the expected range. The value of hydrodynamic COF found is, $\mu_h=0.140$. The MFL model results were comparable with the scratch test. The COF measured by the scratch test line up in the extrapolation of the model. The MFL model showed agreement with friction tests results from previous studies.

Powdering is also a critical parameter in metal forming. Although some coating loss of a GA steel sheet in a formed panel does not compromise its corrosion resistance or its final appearance, it can produce problems for the forming dies. Powdering of the GA coatings was characterized with the double-Olsen test by measuring metal loss. The observations obtained from this characterization are the following:

- The powdering, measured as metal loss per test, decreases as the Fe content in the coating increases.

- There was no direct correlation with the amount of $\zeta$-phase present on the coating surface and the amount of powdering.

During the friction testing, the $\zeta$-phase on the surface increased the real contact area. This increase of contact area produces a reduction of the real shear stress experienced by the coating. The presence of the $\zeta$-phase protects the coating against shear failure caused by friction, even when it increases the COF.

The most significant factor affecting the friction response was the $\zeta$-phase. The $\zeta$-phase deforms in contact, increasing the real contact area and increasing the COF. A coating that is expected to have good powdering resistance must keep the Fe content of the coating below a certain threshold. There is no GA coating that would result in a low COF and good powdering resistance; however, there are processing parameters that would produce a GA coating with optimized characteristics.

154

# REFERENCES CITED

1 D. A. Jones, *Principles and Prevention of Corrosion,* 2$^{nd}$ edition, Prentice-Hall, Upper
      Saddle River, NJ, USA, , 1996.

2 R. F. Tylecote, *A History of Metallurgy,* 2$^{nd}$ edition, The Institute of Materials, London,
      UK, 1996.

3 G. Agricola / H.C. & L.H. Hoover, *De Re Metallica,* Dover Publications, New York, NY,
      USA, 1556 / 1950.

4 F. Habashi, "Discovering the 8th Metal, A history of Zinc",
      http://www.iza.com/zwo_org/Publications/Discovering/0202.htm, International Zinc
      Organization, accessed March 12, 2006.

5 A. R. Marder, "Microstructural Characterization of Zinc Coatings", *Zinc-Based Steel*
      *Coating Systems: Metallurgy and Performance,* edited by G. Krauss and D. K.
      Matlock, TMS, Warrendale, PA, USA, 1990, pp 55-82.

6 *ASM Handbook, Vol. 5, Surface Engineering,* ASM International, Materials Park, OH,
      USA, 2002.

7 T. Sekita, S. Iida, T. Kiyasu, H. Shigemoto, S. Uchiyama, and N. Suganuma.
      "Development of New CGL at Kawasaki Steel for Automotive Use", *2$^{nd}$*
      *International Conference on Zinc and Zinc Alloy Coated Steel Sheet, GALVATECH*
      *'92,* Stahleisen, Amsterdam, Netherlands, 1992, pp 41-47.

8 S. T. Bluni and A. R. Marder, "Galfan Microstructure and Surface Characteristics", *The*
      *Physical Metallurgy of Zinc Coated Steel,* edited by A. R. Marder, TMS, Warrendale,
      PA, USA, 1994, pp 99-109.

9 M. Lamberigts and F. E. Goodwin, "Process-Structure-Property Relationships in Commercial Galfan® Sheet Steels", *The Physical Metallurgy of Zinc Coated Steel*, edited by A. R. Marder, TMS, Warrendale, PA, USA, 1993, pp 79-87.

10 K. L. Lin, J. K. Ho, C. S. Jong, and J. T. Lee, "The Formation of Intermetallics and Its Effect on the Microstructure of the Hot Dip 5% Al-Zn Coating on Steel", *The Physical Metallurgy of Zinc Coated Steel*, edited by A. R. Marder, TMS, Warrendale, PA, USA, 1993, pp 89-97.

11 T. Hada, "Production Technologies of Ho-Dip Zinc-Aluminum Alloy Coated Steel Sheet", *4$^{th}$ International Conference on Zinc and Zinc Alloy Coated Steel Sheet, GALVATECH '98*, ISIJ, Chiba, Japan, 1998, pp 108-114.

12 R. D. Jones, R. Trinick, J. Wolsenholme, S. T. Bluni, and A. R. Marder, "The Surface Topography of Hot-Dip Galvafan Coatings", *4$^{th}$ International Conference on Zinc and Zinc Alloy Coated Steel Sheet, GALVATECH '98*, ISIJ, Chiba, Japan, 1998, pp 115-126.

13 Y. Tokunga, "Application of Interstitial-Free (IF) Steel Sheets to Automobile Parts", *Metallurgy of Vacuum-Degassed Steel Products*, edited by R. Pradhan, TMS, Warrendale, PA, USA, 1990, pp 91-108.

14 E. Agurre, B. Fernandez, and J. M. Puente. "Post-Annealed 55 % Al-Zn Alloy Coated Steel Sheets: Microstructural Characterization and Ductility Properties", *The Physical Metallurgy of Zinc Coated Steel*, edited by A. R. Marder, TMS, Warrendale, PA, USA, 1993, pp 137-152.

15 A. Miyasaka, "Recent Progress and Perspective of the Zn and Zn-alloy Coatings in Japan", *6$^{th}$ International Conference on Zinc and Zinc Alloy Coated Sheet Steels, GALVATECH '04*, AIST, Chicago, IL, USA, 2004, pp 3-8.

16 S. Sugimoto, "Expectation for Automotive Coated Steel Sheet in View of Const and Global Supplyability Needs", *4$^{th}$ International Conference on Zinc and Zinc Alloy Coated Steel Sheet, GALVATECH '98*, ISIJ, Chiba, Japan, 1998, pp. 64-69.

17 K. Ostyn and K. Rubben, "Evaluation of Coating Parameters Affecting the Resistance Welding of Zinc-Coated Steels", *2nd International Conference on Zinc and Zinc Alloy Coated Steel Sheet, GALVATECH '92*, Stahleisen, Amsterdam, Netherlands, 1992, pp 100-104.

18 T. Irei, "Development of Zinc-Based Coatings for Automotive Sheet Steel in Japan", *Zinc-Based Steel Coating Systems: Metallurgy and Performance*, edited by G. Krauss and D. K. Matlock, TMS, Warrendale, PA, USA, 1990, pp 143-155.

19 W. Bleck, R. Bode, and F.J. Hahn, "Interstitial-Free Steels Processing, Properties and Applications", *Metallurgy of Vacuum-Degassed Steel Products*, edited by R. Pradhan, TMS, Warrendale, PA, USA,1990, pp 73-90.

20 Y. Tokunga, "Application of Interstitial-Free (IF) Steel Sheets to Automobile Parts", *Metallurgy of Vacuum-Degassed Steel Products*, edited by R. Pradhan, TMS, Warrendale, PA, USA,1990, pp 91-108.

21 D.J. Bologna, "Corrosion Resistant Materials and Body Paint Systems for Automotive Applications", SAE Paper 862015, *Proceedings of the Automotive Corrosion and Prevention Conference, P-188*, Society of Automotive Engineers, Warrendale, PA, USA,1986, pp 69-80.

22 J. Mackowiak and N. R. Short, "Metallurgy of Galvanized Coatings", International Metals Reviews, Vol. 24, 1979, pp 1-19.

23 *ASM Handbook, Vol. 3, Alloy Phase Diagrams*, ASM International, Materials Parks, OH, USA, 2002.

24 N.-Y. Tang, X.B. Yu, and F.N. Coady, "Phase Transition in Galvanneal Coatings", Metallurgical and Materials Transactions A, Vol. 34A, March 2003, pp 879-881.

25 C. E. Jordan and A. R. Marder, "A Model for Galvanneal Morphology Development", *The Physical Metallurgy of Zinc Coated Steel*, edited by A. R. Marder, TMS, Warrendale PA, USA, 1993, pp 197-219.

157

26 E. T. NcDevitt and M. Meshii, "Microstructural Evolution during Galvannealing. Part II: Formation and Growth of the Fe-Zn Intermetallic Compounds", *4th International Conference on Zinc and Zinc Alloy Coated Steel Sheet, GALVATECH '98*, ISIJ, Chiba, Japan, 1998, pp 161-167.

27 C. S Lin, M. Meshii, and C. C. Cheng, "Phase Evolution during Galvanneal Process", *The Use and Manufacture of Zinc and Zinc Alloy Coated Sheet Steel Products into the 21st Century, GALVATECH '95*. IIS, Chicago, IL USA, 1995, pp 485-495.

28 A. Miyasaka and K. Matsumura. "Influence of Alloying Elements in Steel on Galvannealing Behavior of Interstitial-Free (IF) Steels", *4th International Conference on Zinc and Zinc Alloy Coated Steel Sheet, GALVATECH '98*, ISIJ, Chiba, Japan, 1998, pp 185-189.

29 S. H. Deits and D. K. Matlock, "Formability of Coated Sheet Steels: An Analysis of Surface Damage Mechanisms", *Zinc-Based Steel Coating Systems: Metallurgy and Performance*, edited by G. Krauss and D. K. Matlock, TMS, Warrendale, PA, USA, 1990, pp 297-317.

30 V. Rangarajan, "Influence of Strain State on Powdering of Galvannealed Sheet Steel", *New Steel Products and Processing for Automotive Applications, SP-1172, SAE Technical Paper Series 960026*, SAE International, Warrendale, PA, USA, 1996.

31 V. Rangarajan, "Galvanneal Powdering in Drawbeads", *Steel in Automotive Applications SP-1259, SEA Technical Paper Series 970150*, SAE International, Warrendale PA, USA, 1997.

32 J. Foct, A. Iost, and G. Reimont, "Mechanical Behavior of Zinc Coating", *The Physical Metallurgy of Zinc Coated Steel*, edited by A. R. Marder, TMS, Warrendale, PA, USA, 1993, pp 21-30.

33 W. Zhong, H.F. Ng, and M. Ichikawa, "Effect of Coating Characteristics on Powdering Performance of Galvanneal Coatings", *4th International Conference on Zinc and Zinc Alloy Coated Steel Sheet, GALVATECH '98*, ISIJ, Chiba, Japan, 1998, pp 603-607.

34 C. Cheng and V. Rangarajan, L. Franks, "The Effect of Steel Substrate on the Microstructure and Powdering of Galvanneal Coatings", *2nd International Conference on Zinc and Zinc Alloy Coated Steel Sheet, GALVATECH '92,* Stahleisen, Amsterdam, Netherlands, 1992, pp 122-126.

35 M.F. Shi, G.M. Smith, M. Moore, D. J. Meuleman, "Galvannealed Coating Optimized for Coating Adhesion Through Dies", *Zinc-Based Steel Coating Systems: Metallurgy and Performance,* edited by G. Krauss and D. K. Matlock, TMS, Warrendale, PA, USA, 1990, pp 387-398.

36 S.P. O'Dell and J. Charles, "The Formations of Craters Within the Galvanneal Coating and Their Effects on Processing Properties", *44th Mechanical Working and Steel Processing Conference Proceedings,* Vol. 40, ISS, Warrendale, PA, USA, 2002, pp 1299-1307.

37 D. Bhattacharya and C. Cheng, "Mechanism of the Effect of Nb on the Galvannealing Behavior of IF Steels", *6th International Conference on Zinc and Zinc Alloy Coated Sheet Steels, GALVATHEC '04,* Chicago, IL, USA, 2004, pp 509-516.

38 M. Urai, M. Arimura, H. Sakai, and S. Nomura, "Effects of Galvanizing and Galvannealing Conditions on Powdering Characteristics of Galvannealed Steel Sheet", *Kobelco Technology Review,* No. 19, April 1996, pp 27-30.

39 D. Dowson, *History of Tribology,* Longman, London, UK, 1979.

40 ASTM E8-01, *2001 Annual Book of ASTM Standards,* 2001 Vol. 3.01, American Society for Testing and Materials, West Conshohocken, PA, USA, p. 58.

41 J.R. Kilpatrick, "A New Etching Technique for Galvannealed and Hot-Dipped Galvanized Coatings", Praktiche Metallographie (Germany), Vol. 28, 1991, pp 649-658.

42 C.E Jordan, K.M. Goggins, A.O. Benscoter, and A.R. Marder, "Metallographic Preparation Technique for Hot-Dip Galvanized and Galvannealed Coatings on Steel", Materials Characterization (UK), Vol. 31, 1993, pp. 107-114.

43  C. Xoffer, H. Dillen, and B.C. De Cooman, "Quantitative Phase Analysis of
     Galvannealed Coatings by Coulometric Stripping", Journal of Applied
     Electrochemistry, Vol. 29, 1999, pp 209-219.

44 http://rsb.info.nih.gov/ij/ accessed February 18th, 2006.

45 E.J. Abbott and F.A. Firestone, "Specific Surface Quality", Mechanical Engineering, Vol.
     55, 1933, pp 569-572.

46 W.J. Wojtowicz, "Sliding Friction Test for Metalworking Lubricants", Lubrication
     Engineering, Vol. 11, 1955, pp. 174-177.

47 H.W. Swift, "Plastic Bending Under Tension", Engineering, Vol. 166, 1948, pp 333-335,
     357-359.

48 J.A. Shey, Tribology in Metalworking, 2nd edition, AMS, Metals Park, OH, USA, 1984.

49 E. Doege and K.P. Witthüser, HFF-Bericht 9 UKH, Gesellshaft fur Produktionsechnik,
     Hannover, 1977, pp 129-137.

50 M. Littlewood and J.F. Wallace, "The Effect of Surface Finish and Lubrication on
     Frictional Variations Involved in the Sheet Metal Forming Processes", Sheet Metal
     Industry, Vol. 41, 1964, pp. 925-930.

51  D.W. Vallance and D.K. Matlock, "Application of the Bending –Under-Tension Friction
     Test to Coated Sheet Steels", Journal of Material Engineering and Performance, ASM
     International, Vol. 1, 1992, pp 685-693.

52  G. Coubrough, Friction During Stretch-Bend Deformation, PhD Dissertation T-5196,
     Colorado School of Mines, Golden, CO, USA, 1998.

53 G.J. Wenszloff, T.A. Hylton, and D.K. Matlock, "Technical Note: A New Test Procedure
     for the Bending under Tension Friction Test", Journal of Material Engineering and
     Performance, ASM International, Vol. 1, 1992, pp 609-613.

54 R.T Fox, A.M. Maniatty, and D. Lee, "Determination of Friction Coefficient for Sheet
     Materials under Stretch-Forming Conditions", Metallurgical Transactions A, Vol. 2,
     1989, pp 2179-2182.

55 M. Sulonen, P. Eskola, J. Kumpulainen, and A. Ranta-Eskola, "A Reliable Method for Measuring the Friction Coefficient in Sheet Metal Forming", *IDDRG Working Group Meetings, Paper WG III/4*, Tokyo, Japan, 1981

56 K.M. Pickett, G.J. Fata, and D.J. Meuleman, "The Double Reverse Olsen and Stretch-Draw Tests for Evaluating Adhesion of Metallic Coatings on Sheet Steel", Journal of Materials Shaping Technology, Vol. 8, 1990, pp149-158.

57 DaimlerChrysler Corporation LProcedures MS-6000 and MS-8056.

58 G. Deiter, *Workability Testing Techniques*, ASM, Metals Park, OH, USA, 1984.

59 S Taira, M Sakurai, Y. Yamasaki, Y. Sugimoto, J. Inagaki, and M. Yamashita, "Factors Affecting Surface Friction of Galvannealed Steel Sheet", *44th Mechanical Working and Steel Processing Conference Proceedings*, Vol. 40, ISS, Warrendale, PA, USA, 2002, pp 1263-1270.

60 D Haynes and P. Hodgson, "Influence of Galvannealed Coating Structure on Press Formability", *44th Mechanical Working and Steel Processing Conference Proceedings*, Vol. 40, ISS, Warrendale, PA, USA, 2002, pp 1271-1279.

61 M. Sakurai, T. Imokawa, Y. Yamasaki, S. Hashimoto, J. Inagaki, and M Yamashita, "Effect of Surface Modification on Coefficient of Friction of Galvannealed Steel Sheet", *5th International Conference on Zinc and Zinc Alloy Coated Steel Sheet, GALVATECH '200*, Verlag-Stahleisen, Brussels, Belgium, 2001 pp 65-71.

62 J. Mataigne, P. Drillet, J. Prat, D. Mareuse, P. Terreaux, and M. Guttmann, "Optimized Galvannealed Coating Microstructure for Automotive Applications", *The Use and Manufacture of Zinc and Zinc Alloy Coated Sheet Steel Products into the 21st Century, GALVATECH '95*, ISS, Chicago, IL, USA, 1995, pp 589-597.

63 M. H. Hong and H. Saka, "Mechanical Properties of the $\zeta$ Intermetallic Compound in the Fe-Zn System", *4th International Conference on Zinc and Zinc Alloy Coated Steel Sheet, GALVATECH '98*, ISIJ, Chiba, Japan, 1998, pp 248-253.

64 N. Bay and T. Wanheim, "Real Area of Contact and Friction Stress at High Pressure Sliding Contact", Wear, Vol. 38, 1976, pp 201-209.

65 N. Demkin and V. Izmailov, "Plastic Contact Under High Normal Pressure", Wear, Vol. 31, 1975, pp 391-402.

66 T. A. Hylton, C.J. Van Tyne, and D.K. Matlock, "Frictional Behavior of Electrogalvanized Sheet Steels, *SAE Technical Papers 930809*, Warrendale, PA, USA< 1993, pp 241-253.

67 R.W. Logan, D.J. Meuleman, and W.F. Hosford, "The Effects of Anisotropy on the Limiting Drawing Ratio", in *Formability and Metallurgical Structure*, TMS, Warrendale, PA, USA, 1987, pp. 159-173.

68 I. Hertveldt, B.C. De Cooman, K. Meeure, and C. Xhoffer, "The Shear Strength of Galvannealed Coatings on IF Steels", ISIJ International, Vol. 39, 1999, pp 1280-1288.

69 T. Nakamori, Y. Adachi, M. Arai, and A. Shibuya, "Coating Adhesion and Interface Structure of Galvannealed Steel", ISIJ International, Vol. 35, 1995, pp 1494-1501

70 I. Hertvedt, B.C. De Cooman, and J. Dilewijns, "Properties of Galvannealed Coatings on TiNb- and Ti-Stabilized Interstitial Free High Strength Steels", *39th Metal Working and Steel Processing Conference Proceedings*, ISS, Warrendale, PA, USA, Vol. 35, 1998, pp 105-113.

71 A.T. Alpas and J. Inagaki, "Effect of Microstructure on Fracture Mechanics in Galvannealed Coatings", ISIJ International, Vol. 40, No. 2, 2000, pp 172-181.

72 B. Bhushan, *Principles and Applications of Tribology*, John Wiley & Sons, New York, NY, USA, 1999.

73 G. Stachowiak, A. Batchelor, *Engineering Tribology*, Butterworth Heinemann, Boston MA, USA, 2001.

74 P. J. Blau, *Friction Science and Technology*, Marcel Dekker, New York, NY, USA, 1995, pp. 211.

75 D. W. Vallance, Analysis of Friction Behavior of Coated Sheet Steel Using the Bending Under Tension Test, , T-3796, Colorado School of Mines, Golden CO, USA, 1990.

76 E. E. Gallo, *Friction and Formability of Hot-Dip Galvanneal Interstitial-Free Sheet Steel*, MS-Thesis T-4851, Colorado School of Mines, Golden, CO, USA, 1995.